University of Potsdam
Faculty of Science

Transient Absorption Spectroscopy: A Versatile Tool for Investigating Excited States in Organic and Inorganic Molecules

Toni Haubitz

Cumulative dissertation

in fulfillment of the requirements
for the degree of
"doctor rerum naturalium"
(Dr. rer. nat.)
in the subject of "Physical Chemistry"

presented to
The Faculty of Science
Institute of Chemistry
at the
University of Potsdam
Potsdam, Brandenburg
10th of January 2022

Supervisor: apl. Prof. Dr. Michael U. Kumke
Co-Supervisor: Prof. Dr. Pablo Wessig
External Examiners: Prof. Dr. Tobias Reich, Prof. Dr. Freek Ariese

Published online on the
Publication Server of the University of Potsdam:
https://doi.org/10.25932/publishup-52681
https://nbn-resolving.org/urn:nbn:de:kobv:517-opus4-526814

Thesis advisor: apl. Prof. Dr. Michael U. Kumke Toni Haubitz

Transient Absorption Spectroscopy: A Versatile Tool for Investigating Excited States in Organic and Inorganic Molecules

Abstract

The optical properties of chromophores, especially organic dyes and optically active inorganic molecules, are determined by their chemical structures, surrounding media, and excited state behaviors. The classical optical go-to techniques for spectroscopic investigations are absorption and luminescence spectroscopy. While both techniques are powerful and easy to apply spectroscopic methods, the limited time resolution of luminescence spectroscopy and its reliance on luminescent properties can make its application, in certain cases, complex, or even impossible. This can be the case when the investigated molecules do not luminesce anymore due to quenching effects, or when they were never luminescent in the first place.

In those cases, transient absorption spectroscopy is an excellent and much more sophisticated technique to investigate such systems. This pump-probe laser-spectroscopic method is excellent for mechanistic investigations of luminescence quenching phenomena and photoreactions. This is due to its extremely high time resolution in the femto- and picosecond ranges, where many intermediate or transient species of a reaction can be identified and their kinetic evolution can be observed. Furthermore, it does not rely on the samples being luminescent, due to the active sample probing after excitation.

In this work it is shown, that with transient absorption spectroscopy it was possible to identify the luminescence quenching mechanisms and thus luminescence quantum yield losses of the organic dye classes O^4-DBD, S^4-DBD, and pyridylanthracenes. Hence, the population of their triplet states could be identified as the competitive mechanism to their luminescence. While the good luminophores O^4-DBD showed minor losses, the S^4-DBD dye luminescence was almost entirely quenched by this process. However, for pyridylanthracenes, this phenomenon is present in both the protonated and unprotonated forms and moderately effects the luminescence quantum yield. Also, the majority of the quenching losses in the protonated forms are caused by additional non-radiative processes introduced by the protonation of the pyridyl rings.

Furthermore, transient absorption spectroscopy can be applied to investigate the quenching mechanisms of uranyl(VI) luminescence by chloride and bromide. The reduction of the halides by excited uranyl(VI) leads to the formation of dihalide radicals $X_2^{\cdot -}$. This excited state redox process is thus identified as the quenching mechanism for both halides, and this process, being diffusion-limited, can be suppressed by cryogenically freezing the samples or by observing these interactions in media with a lower dielectric constant, such as ACN and acetone.

Betreuer der Dissertation: apl. Prof. Dr. Michael U. Kumke Toni Haubitz

Transient Absorption Spectroscopy: A Versatile Tool for Investigating Excited States in Organic and Inorganic Molecules

Zusammenfassung

Die optischen Eigenschaften von organischen Farbstoffen und optisch aktiven anorganischen Molekülen werden durch ihre chemische Struktur, ihrer chemischer Umgebung, und durch das Verhalten ihrer angeregten Zustände bestimmt. Die klassischen Methoden zur Untersuchung dieser Eigenschaften sind die Absorptions- und Lumineszenzspektroskopie. Obwohl beide Methoden leistungsfähig und einfach anzuwenden sind, stellen die fehlende Zeitauflösung respektive das benötigte Vorhandensein von Lumineszenz in gewissen Anwendungen ein Problem dar. Dies ist der Fall, wenn die zu untersuchenden Moleküle durch Löscheffekte keine Lumineszenz mehr aufweisen oder von vornherein nicht lumineszent sind.

Unter diesen Umständen ist die Transientenabsorptionsspektroskopie eine exzellente Alternative. Dieses laserspektroskopische Anregungs-Abfrage-Verfahren ist für mechanistische Untersuchungen von Lumineszenz-Löschphänomenen und Photoreaktionen sehr gut geeignet. Aufgrund seiner extrem hohen Zeitauflösung im Femto- und Picosekundenbereich können Intermediate und transiente Spezies identifiziert und deren kinetische Entwicklung beobachtet werden. Da es sich außerdem um eine aktive Abfrage des Probenzustands handelt, entfällt die Notwendigkeit von lumineszenten Probeneigenschaften.

In dieser Arbeit konnten mittels Transientenabsorptionsspektroskopie die Lumineszenz-Löschmechanismen der organischen Farbstoffklassen O^4-DBD, S^4-DBD, und der Pyridylanthracene aufgeklärt werden. Bei all diesen Farbstoffen konnte die Bildung von Triplettzuständen als kompetitiver Mechanismus zur Lumineszenz identifiziert werden. Während bei den O^4-DBD-Farbstoffen diese Verluste eher gering ausfallen, wird die Lumineszenz der S^4-DBD-Farbstoffe fast vollständig gelöscht. Eine Triplettbildung konnte ebenfalls bei den Pyridylanthracenen beobachtet werden, sie hat jedoch einen eher moderaten Anteil am Löschverhalten der Lumineszenz. Der Hauptteil der Lumineszenz-Löschung der protonierten Pyridylanthracene wird eher durch zusätzliche nicht-strahlende Desaktivierungsprozesse über die Pyridylringe verursacht.

Es konnte gezeigt werden, dass die Transientenabsorptionsspektroskopie für die Untersuchung des Löschverhaltens von Uranyl(VI)-Lumineszenz durch Chlorid und Bromid geeignet ist. Es wurde geschlussfolgert, dass die Reduktion der Halogenide durch angeregtes Uranyl(VI) zur Bildung von Dihalogenidradikalen $X_2^{\bullet -}$ führt. Diese Redoxreaktion im angeregten Zustand wurde daher als Lumineszenz-Löschmechanismus für beide Halogenide identifiziert. Dieser diffusionslimitierte Mechanismus wird unter cryogenen Bedingungen oder in schwächeren dielektriktrischen Lösemitteln wie ACN oder Aceton unterdrückt.

I, Toni Haubitz, declare that this thesis, titled "Transient Absorption Spectroscopy: A Versatile Tool for Investigating Excited States in Organic and Inorganic Molecules", and the work presented in it are my own. I have not used any sources other than those listed in the bibliography and identified as references. I furthermore assure that this work has not been submitted in any other way yet. This is my first attempt.

Signature:

Date:

Acknowledgments

First, I would like to thank my supervisor apl. Prof. Dr. Michael Kumke for the excellent mentoring during my time as a Ph.D. student and all the very professional and constructive discussions on the topics of spectroscopy and chemistry. I would also like to thank Prof. Dr. Pablo Wessig and Leonard John for their great collaboration between our departments.

My special thanks go to Dr. Sascha Eidner, Dr. Robin Steudtner, Dr. Björn Drobot, and Dr. Jerome Kretzschmar for all their invaluable advice on chemistry, spectroscopy, and data analysis and for all the great time we spent together over the years, both inside and outside of work. Their great mentoring mainly influenced my scientific career and my approach to scientific problem solving.

My thanks also go to all the colleagues of the physical chemistry group at the University of Potsdam and the colleagues of the Helmholtz-Zentrum Dresden-Rossendorf, for always being helpful on all matters and questions and for the great collaboration over the years.

Finally, I would like to thank all my family and friends for all their support over all the years that made this thesis possible, and I can call myself lucky to have them.

Contents

List of Figures

List of Tables

List of Abbreviations

ACN	Acetonitrile
AO	Atomic Orbital
CCD	Charge Coupled Device
DBD	[1,3]dioxolo[4,5-*f*][1,3]benzodioxole
ΔOD	Change in Optical Density
ES	Excited State
exc.	Excitation
f	Fluorescence
FC	Franck–Condon
FRET	Förster Resonance Energy Transfer
GS	Ground State
GSB	Ground State Bleach
HOMO	Highest Occupied Molecular Orbital
HZDR	Helmholtz-Zentrum Dresden-Rossendorf
IC	Internal Conversion
IR	Infrared
ISC	Intersystem Crossing
LUMO	Lowest Unoccupied Molecular Orbital
ODE	Ordinary Differential Equation
OPA	Optical Parametric Amplification
p	Phosphorescence
PARAFAC	Parallel Factor Analysis
S	Singlet
SE	Stimulated Emission
SR	Solvent-Relaxed
T	Triplet
TA	Transient Absorption
TAS	Transient Absorption Spectroscopy
TCSPC	Time-Correlated Single Photon Counting
TD-DFT	Time-Dependent Density Functional Theory
TRLFS	Time-Resolved Laser-Induced Fluorescence Spectroscopy
UV/Vis	Ultraviolet/Visible
VR	Vibrational Relaxation
WLC	White-Light Continuum

List of Publications

First Author:

1. Haubitz, T., Tsushima, S., Steudtner, R., Drobot, B., Gerhard Geipel, Stumpf, T., & Kumke, M. U., Ultrafast Transient Absorption Spectroscopy of UO_2^{2+} and $[UO_2Cl]^+$. *Journal of Physical Chemistry A*,2018, *122*(35), 6970–6977

2. Haubitz, T., John, L., Wessig, P., & Kumke, M. U., Photophysics of Acyl- and Ester-DBD Dyes: Quadrupole-Induced Solvent Relaxation Investigated by Transient Absorption Spectroscopy. *Journal of Physical Chemistry A*,2019, *123*(22), 4717–4726.

3. Haubitz, T., John, L., Freyse, D., Wessig, P., & Kumke, M. U., Investigating the Sulfur "Twist" on the Photophysics of DBD Dyes. *Journal of Physical Chemistry A*, 2020, *124*(22), 4345–4353.

4. Haubitz, T., Fudickar, W., Linker, T., & Kumke, M. U., pH-Sensitive Fluorescence Switching of Pyridylanthracenes: The Effect of the Isomeric Pattern. *Journal of Physical Chemistry A*, 2020, *124*(52), 11017–11024.

5. Haubitz, T., Drobot, B., Tsushima, S., Steudtner, R., Stumpf, T., & Kumke, M. U., Quenching Mechanism of Uranyl(VI) by Chloride and Bromide in Aqueous and Non-Aqueous Solution. *Journal of Physical Chemistry A*,2021,*125*(20), 4380–4389.

Co-Author:

1. Kretzschmar, J., Haubitz, T., Hübner, R., Weiss, S., Husar, R., Brendler, V., & Stumpf, T., Network-like arrangement of mixed-valence uranium oxide nanoparticles after glutathione-induced reduction of uranium(VI). *Chemical Communications*, 2018, *54*, 8697–8700.

2. Hoang, H. T., Haubitz, T., & Kumke, M. U., Photophysics of "Floppy" Dyads as Potential Biomembrane Probes. *Journal of Fluorescence*, 2018, *28*, 1225–1237.

3. Burek, K., Krause, F., Schwotzer, M., Nefedov, A., Süssmuth, J., Haubitz, T., Kumke, M. U., & Thissen, P., Hydrophobic Properties of Calcium-Silicate Hydrates Doped with Rare-Earth Elements. *ACS Sustainable Chemistry & Engineering*, 2018, *6*(11), 14669–14678.

4. Kretzschmar, J., Strobel, A., Haubitz, T., Drobot, B., Steudtner, R., Barkleit, A., Brendler, V., & Stumpf, T., Uranium(VI) Complexes of Glutathione Disulfide Forming in Aqueous Solution. *Inorganic Chemistry*, 2020, *59*(7), 4244–4254.

5. Chemura, S., Haubitz, T., Primus, P. A., Underberg, M., Hülser, T., & Kumke, M. U., Europium-Doped Ceria–Gadolinium Mixed Oxides: PARAFAC Analysis and High-Resolution Emission Spectroscopy under Cryogenic Conditions for Structural Analysis. *Journal of Physical Chemistry A*, 2020, *124*(24), 4972–4983.

6. López de Guereñu, A., Klier, D. T., Haubitz, T., & Kumke, M. U., Influence of Gd^{3+} doping concentration on the properties of $Na(Y,Gd)F_4:Yb^{3+}$, Tm^{3+} upconverting nanoparticles and their long-term aging behaviour. 2021, in preparation

1

Introduction

For centuries, the interaction of light and matter fascinates people around the world, it induces the creation of paints, glasses, lamps, and more, even without a detailed understanding of this interaction. However, only with the rise in physics and chemistry as scientific disciplines does the understanding of this interaction become clearer and induce new technological developments, such as synthetic fluorescent dyes [1], nanomaterials [2], and sophisticated light sources like the laser [3]. This development has made optical spectroscopy one of the biggest branches of analytical tools, for example, in concen-

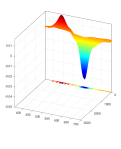

tration measurements of toxins such as uranium by fluorescence [4], detection of pollutants by light detection and ranging [5], composition analysis of minerals and materials by laser-induced breakdown spectroscopy [6], and many more.

Furthermore, only the development of ultrashort pulse lasers [7] and their application in chemistry have revealed the possibility of observing chemical processes on the nanoscale and understanding chemical reaction mechanisms in the picosecond time range. Understanding the chemical reactions and photophysical processes of chromophores is imperative for their analytical applications because, with vigorous and fundamental knowledge about these processes, the reaction or luminescence quantum yield losses can be reduced, and photochemical efficiencies can be maximized to be useful in practical applications. This understanding of chemical and photophysical processes is especially important in the design of organic dyes because their photophysical properties define their applications and practical values. Widely used dyes, such as rhodamine derivatives, are used for many applications, especially in microscopy for staining cells [8], for nanometer distance measurements [9], or in newer applications, such as stimulated emission depletion [10], for microscopic analysis beyond the diffraction limit. In the latter application, the absorption properties are highly important alongside the dyes' luminescent properties, such as quantum yield, lifetime, and Stokes shift. Hence, the scientific community is always in search of new, highly flexible, and adjustable dyes to further broaden their practical applications.

One of those newly developed fluorescent dye class is the so called DBD ([1,3]dioxolo[4,5-*f*][1,3] benzodioxole) scaffold [11]. Their high flexibility in absorption and luminescence properties due to different substitution patterns on the dye's core [12] make them extremely promising for microscopy applications and use as "nanometer rulers" in Förster resonance energy transfer (FRET) applications [13]. This flexibility extends to solubility adjustments, where they can be used in non-aqueous matrices, such as lipid membranes [14]. However, the DBD luminescence quantum yield of 30% to 50% in non-aqueous solvents [12] drops drastically when dissolved in highly polar solvents like water, which lowers their analytical value due to shorter luminescence lifetimes and lower signal-to-noise ratios.

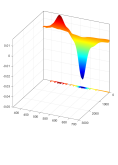

This problem of strong quenching is even worse in a derivate of oxygen-based DBD dyes, where sulfur replaces the oxygen in the chromophore. However, due to their even stronger redshift of luminescence, these "S⁴-DBD" dyes [15] will be good candidates to even further extend this class of chromophore if the luminescence quenching could be minimized.

Another dye class that faces a similar problem are pyridylanthracenes [16], which could be used in the future as sensors, for example for temperature, oxygen, and pH. Especially for pH/proton activity sensors, the quenching phenomenon in acidic aqueous solutions can be used as a pH indicator. However, it would be more elegant to know the source of this quenching effect under acidic conditions and to adapt the dye so that the luminescent properties simply change upon protonation but do not fully disappear.

Another major branch of the application of spectroscopy is the detection and quantification of dangerous and toxic chemicals in water and soil, which can be harmful to humans and the biosphere. One of those potential health risks is uranium, a heavy metal that is dangerous not only due to its chemotoxicity [17], but also its radiotoxicity [18] because of its long radioactive half-life. Its' presence in naturally occurring mineral waters and drinking water is usually quite low [19], but it can significantly increase if the geochemical barriers of a long-term nuclear waste repository fail. A go-to technique for uranyl(VI) detection in solution in the down-to-nanomolar range is luminescence spectroscopy [20]. However, this is only applicable if the uranyl(VI) luminescence is not quenched by other ions in the sample matrix. Typical ions for uranyl(VI) quenching, such as hydroxides [21], metal ions [22], carbonates [23], and halides [24], are abundant in possible real-world samples of contaminated ground or geological pore waters. With large amounts of these quenchers, luminescence spectroscopy is practically "blind" for these uranium complexes and is not useful for risk assessment or long-term repository research.

To understand all these luminescence quenching effects in organic and inorganic chromophores, we must understand the photochemical processes in the excited states and their effects on the luminescence of the emitting electronic state. The most promising technique for gaining such a fundamen-

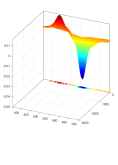

tal photophysical understanding is transient absorption spectroscopy (TAS) [25]. This laser-based pump-probe technology makes it possible to observe the evolution of a photoactive molecule on extremely small time scales, down to the femtosecond range. Due to its active probing laser beam, the investigated molecule does not need to be luminescent; thus, strongly quenched systems or systems that are not luminescent in the first place can be analyzed. That makes it applicable whenever luminescence spectroscopy is "blind" for any inorganic complexes or organic dyes. Also, due to the extremely high time resolution, we can determine the chemical reactions and photophysical mechanisms that induce luminescence quenching. Based on the information gained and the further improved fundamental understanding of the chromophore by TAS, we can undertake new synthesis approaches or use different complexating agents to counter these quenching phenomena, thereby revealing the possibility of a better practical application of luminescence and absorption techniques for these photoactive systems.

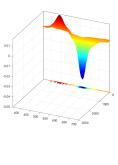

The Laser: A solution in search of a problem.

T. H. Maiman

2 Theoretical Background

In one of Einstein's famous articles in 1905, he proposed a theory of how light is quantized, to describe the photoelectrical effect [26]. It is based on the fact, that incoming light needs a minimal energy E, or frequency ν to eject an electron out of a material. The interpretation of the quantization of light came from the discovery of Max Planck, who found that energy and frequency of light are connected via a constant h, today known as Planck's constant [27].

$$E = h \cdot \nu \tag{2.1}$$

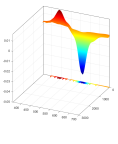

While Max Planck described light as an electrically charged oscillator (dipole) to describe its wave character, the Einstein interpretation of light being a quantized particle leads to today's still valid wave-particle duality. In this duality, light can be, depending on the case, described as a wave or a particle to explain certain phenomena, such as the infamous double slit experiment. Based on Einstein's results, the typical phenomenon of the interaction of light fields (electromagnetic radiation) with matter can only happen in energetically discrete packages or quanta, today known as photons. These interactions are excitation, emission, and scattering.

In the following chapter, light is shed on the most important interactions between electromagnetic radiation and matter, which form the fundamental basis for the here presented thesis and published manuscripts.

2.1 On the Electronic States of Molecules

For a long time, atoms were considered the smallest indivisible units of the universe until the discovery of the electron [28] and the nucleus [29]. The discovery of those induces the current model of the atom, where the nucleus comprises of neutrons and protons and is surrounded by a diffuse electron shell. The electrons are randomly distributed around the nucleus but are localized in specially formed regions of space with a high probability of occupation, called atomic orbitals (AO). An orbital is a mathematical wave function ψ that describes the wave-like behavior of a particle in space and time [30]. Electrons within these orbitals have discrete, and not a continuous, energy. Erwin Schrödinger found in 1926 a mathematical description of these orbitals for the non-relativistic case, the so-called Schrödinger equation, where the derivative of the wavefunction is proportional to the Hamilton operator $\hat{H}$ applied to the wave function [31].

$$i\hbar\frac{\partial}{\partial t}\psi(\mathrm{r},t) = \hat{H}\psi(\mathrm{r},t) \tag{2.2}$$

The solution to this equation gives the discrete energies of the orbitals and wave functions. Thus,

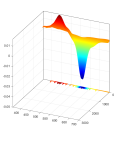

electrons can be considered dipole oscillators in this atomic model. Furthermore, the square of this wave function ψ^2 can be interpreted as the probability of finding an electron in a certain region around the nucleus. With this description of the electron, the view of the atom went away from a classical to a quantum mechanical one [30] with no deterministic behavior, which is described only in terms of probabilities.

The different orbital energies of an atom define its structure and its atomic and ionic radii. The electrons within these orbitals usually occupy the orbitals with the lowest energy first (Hund's rules) and fill up the orbitals from the lowest to the highest energy orbital. Every orbital can be occupied by a maximum of two electrons with opposite spins (Pauli exclusion principle) [32].

Depending on the energy of the orbitals and the nucleus charge, the total number of electrons in an atom can vary. Usually, a close to neutral configuration is found in nature, where the electron charges more or less balance the nucleus charges. When the charges are balanced exactly to zero, it is the elemental form of an atom. However, it is more common to find atoms not in their elemental form but in an ionic form with a positive or negative net charge, where the number of protons and electrons are unbalanced. When all electrons are distributed in the lowest energy orbitals and occupy the lowest energetic distribution, it is called the atoms or ions ground state. On the other hand, if an ion or atom is not in its ground state or lowest energy electron configuration, it is in an excited state electron configuration. Two or more atoms can form molecules by forming chemical bonds between them. These bonds are basically described as molecular orbitals (MOs), which can be mathematically described as the linear combination of the participating atomic orbitals. These MOs follow the same rules for occupation as atomic orbitals. The electron configuration, i.e., state, of an atom, ion, or molecule can be reduced to specific term symbols. For example, in the case of Russell–Saunders coupling, the Russell–Saunders term symbols for atoms and ions [33] take the form of:

$$^{\mathcal{M}}L_J = ^{(2S+1)}\,L_{(L+S)}, \tag{2.3}$$

where the spin multiplicity $\mathcal{M}$ of a state of an atom, ion, or molecule is defined via the total spin

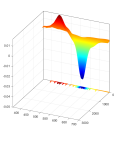

quantum number S, while L is the total orbital angular momentum. The sum of both quantum numbers J is considered as the total angular momentum. The molecule equivalent of the atomic Russell–Saunders coupling uses Greek letters for the total orbital angular momentum Λ.

$$^{M}\Lambda_{J} = ^{(2S+1)}\ \Lambda_{(\Lambda+S)} \tag{2.4}$$

When each electron has an opposite spin partner anywhere in the MO, the spin multiplicity is one, as the total spin angular momentum is zero. This configuration is considered as a singlet state. Unbalanced electron spins lead to higher spin multiplicities, such as doublet for $S = 1/2$ (usually radicals), triplet for $S = 1$, and so on. In general, when changing from a low multiplicity to a high multiplicity electron configuration, the high multiplicity state is lower in energy, due to a reduction in exchange interaction [34] and exchange energy.

Just as electrons are quantized, the vibrations of a molecule are also quantized. That means that molecules cannot vibrate freely at any energy but only at discrete energy levels. These levels are called vibronic states, which result from a coupling of the electronic and the vibrational wavefunction. As the lowest vibronic level is never at zero energy for any molecule or lattice, there is always energy left in a system, and it never reaches zero at the lowest possible temperature (zero-point energy). Furthermore, molecules do not behave as a harmonic oscillator (symmetric around its equilibrium point) but rather as an anharmonic oscillator (asymmetrically elongated away from the nucleus) with a specific dissociation energy beyond which the two atoms dissociate. Compared to the harmonic oscillator, the vibronic levels of an anharmonic quantum mechanical oscillator are not equally distanced, but the energy difference between two consecutive levels decreases toward higher vibrational energies. To illustrate such vibronic, anharmonic hyperpotential surfaces, a Morse potential is often used (Figure 2.1.1).

To change the electronic state of a molecule, an electron needs to transition from one orbital to another. If the molecule is in its ground state and all electrons reside in the lowest energy orbitals, the only way to transition an electron to another orbital is by the absorption of some form of energy

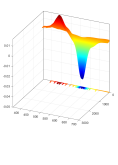

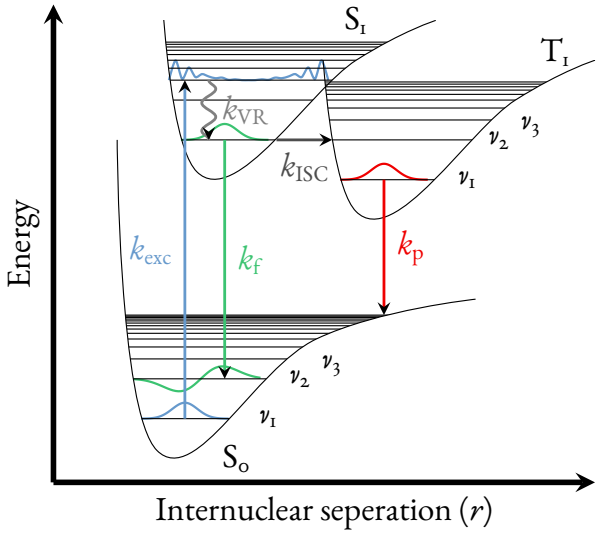

Figure 2.1.1: Jabłoński diagram combined with Morse potential curves of a hypothetical binuclear system with radiative (colored) and non-radiative transitions between three electronic states and several vibronic states. k_i – rate constant, exc – excitation, VR – vibronic relexation, ISC – intersystem crossing, f – fluorescence, p – phosphorescence, ν_i – vibronic sub-level.

(excitation). One way molecules can absorb energy and conduct an electron transition is in the form of light (Figure 2.1.1, blue). However, as the molecule's states are quantized, only photons with the energy (Eq. 2.1) equivalent to the energy difference ΔE between the ground state (GS) E_{GS} and the excited state (ES) E_{ES} can be absorbed (resonance condition, Eq. 2.5).

$$\Delta E = E_{ES} - E_{GS} = h \cdot \nu \tag{2.5}$$

However, even if the energy or frequency of the incoming radiation matches the energy difference between the two states, it does not guarantee an absorption with a consecutive electron transition. The actual probability of the transition is dominated by the overlap of the vibronic wave functions of the initial state ψ_i and the final state ψ_f. This is known as the Franck–Condon principle [35, 36]. It states that a transition is most favorable (higher transition probability) when the initial and final state are most similar, i.e., have the highest magnitude of overlap of their vibronic wave functions. The intensity of an absorption can be described as the transition dipole moment $\langle \mu \rangle$ via the transition

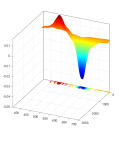

dipole moment operator $\hat{\mu}$:

$$\langle \mu \rangle = \langle \psi_f | \hat{\mu} | \psi_i \rangle \tag{2.6}$$

When considering only the nuclear (N) and electronic (e) wave functions of those states, we obtain the transition dipole moment as follows:

$$\psi_f = \psi_{f,N} \psi_{f,e} \tag{2.7}$$

$$\psi_i = \psi_{i,N} \psi_{i,e} \tag{2.8}$$

$$\langle \mu \rangle = \underbrace{\langle \psi_{f,N} | \psi_{i,N} \rangle}_{f} \langle \psi_{f,e} | \hat{\mu}_e | \psi_{i,e} \rangle \tag{2.9}$$

So, the intensity of the transition is dominated by the first vibrational term (nuclear wave functions), which is also known as the Franck–Condon factor or oscillator strength f (eq. 2.9).

This principle further states that radiative transitions between hyperpotential surfaces are vertical, as an electron can change orbitals and thus its energy much faster than the involved nuclei change position (Born–Oppenheimer approximation [37]). It holds true for absorptions alongside emissions, where a photon is released upon a transition from a higher energy state to a lower energy state. The energy of this photon is equivalent to the energy gap between these states (Figure 2.1.1, green).

However, non-radiative transitions between electronic states are horizontal, as they introduce vibrations along the coordinates in the molecule without a change in energy (conservation of energy). A non-radiative transition needs some form of perturbation that gives the initial state some probability to transform into the final state, which is calculated via the perturbation operator $\hat{P}$. This perturbation can be described as a series of matrix elements, or, alternatively, the perturbation matrix element V_{fi}.

$$V_{fi} = \langle \psi_f | \hat{P} | \psi_i \rangle \tag{2.10}$$

Furthermore, the transition probability per unit time (or rate constant) from the initial state to

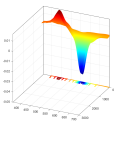

the final state $k_{i\to f}$ also depends on the final density of states $\varrho(E_f)$. Hence, the more possible states are available to transit into, the higher the transition rate constant. The connections between the transition rate constant, the perturbation matrix element, and the final state density are known as Fermi's golden rule [38]:

$$k_{i\to f} = \frac{2\pi}{\hbar} V_{fi}^2 \varrho(E_f) \tag{2.11}$$

From this equation, it is obvious that the stronger factor in this description is the quadratic perturbation element, which is dominated by the Franck–Condon factor f or vibrational wave function overlap integral between the two states. This is why one might assume that, when both potential surfaces are becoming increasingly separated in energy, the increased density of vibronic states of the final state (energetic difference decreases the further up the energy "ladder") might increase the transition rate. However, the transition rate constant usually drops overall as the perturbation matrix element decreases due to the worse vibrational wave function overlap with increasing vibrational energy between the initial and final states. This decrease in non-radiative transition rates with a larger energy gap ΔE between the states is known as the "energy gap law" [39].

Non-radiative transitions between two states of same spin multiplicity (for example, between two singlet states) are referred to as internal conversions (IC), while transitions between states of different spin multiplicity are known as intersystem crossing (ISC). An important result of the energy gap law is that an emission usually occurs from the excited state with the lowest energy (Kasha's rule [40]). This is due to the fact that the energy difference between the singlet ground state S_0 and the first excited singlet state S_1 usually significantly exceeds the energy difference between the S_1 and the higher excited singlet states S_n. That induces a fast relaxation from the S_n into the S_1 state (low energy gap) via non-radiative transitions (IC and vibronic relaxations (VR) through the solvent or phonons) and a very low non-radiative transition rate (very high energy gap) from S_1 to S_0.

This means that the transition from S_1 to S_0 can be dominated by the spontaneous emission rate constant of the fluorescence k_f rather than by non-radiative processes and their corresponding rate constants k_{nr}. A photon emission process is called luminescence. This can be further differentiated

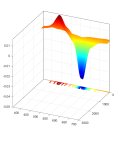

Table 2.1.1: Overview of possible depopulation pathways of excited chromophores.[32]

Process	Transition	Rate constant	Timescale $[s^{-1}]$
Internal conversion (IC)	$S_n \rightarrow S_1$, $T_n \rightarrow T_1$	k_{IC}	$10^{10} - 10^{14}$
Internal conversion (IC)	$S_1 \rightarrow S_0$	k_{IC}	$10^{6} - 10^{7}$
Vibrational relaxation (VR)	$S_{1,\nu=n} \rightarrow S_{1,\nu=0}$	k_{VR}	$10^{10} - 10^{12}$
Singlet-singlet absorption (exc)	$S_0 \rightarrow S_1$, $S_1 \rightarrow S_n$	k_{exc}	10^{15}
Fluorescence (f)	$S_1 \rightarrow S_0$	k_f	$10^{7} - 10^{9}$
Intersystem crossing (ISC)	$S_n \rightarrow T_n$, $T_n \rightarrow S_n$	k_{ISC}	$10^{5} - 10^{8}$
Phosphorescence (p)	$T_1 \rightarrow S_0$	k_p	$10^{-2} - 10^{3}$
Triplet-triplet absorption (exc)	$T_1 \rightarrow T_n$	k_{exc}	10^{15}

into fluorescence, when the transition is occurring between two states with the same multiplicity (for example, two singlet states), and phosphorescence, where the radiative transition is occurring between two states of different multiplicity (for example, a triplet and a singlet state or vice versa). As the transition between electronic states of different multiplicity requires a spin inversion of the transitioning electron, these transitions have a low probability and thus a low rate constant. That is why fluorescence (k_f) is usually much faster than phosphorescence (k_p). When a transition has a low probability or rate constant it is referred to as a "forbidden" transition, i.e., the overlap integral is small or even zero. Other selection rules are that the vibrational wave functions have to overlap (Franck–Condon principle) and that an orbital overlap exists. That is why $\pi \rightarrow \pi^*$ orbital transitions are considered "allowed", while $n \rightarrow \pi^*$ and $f \rightarrow f$ orbital transitions are considered "forbidden". The restrictions by these selection rules can be weakened by certain effects, for example, spin-orbit coupling. This relativistic effect occurs in molecules with atoms of a high atomic number. The result of this "heavy-atom effect" can be a splitting in spectral lines (fine structure) or an increase in the ISC transition rate constants, which for example, induces an increase in triplet formation. When the heavy atom is chemically bound to the molecule, it is called an internal heavy-atom effect, while when the heavy atom is located in the solvent or in the crystal lattice, it is called an external heavy-atom effect. Depending on the "allowedness" of a transition, one can assign time scales in which all these processes can occur (Table 2.1.1).

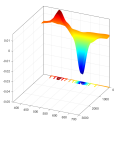

The depopulation of an excited state can thus involve several different pathways with their own unique rate constants k_i. The inverse of the sum of all these deactivation processes n of an electronic state is known as the natural lifetime τ of that state. As it is the sum of probabilities per unit of time (or rate constants), it represents the average time one can expect a molecule to reside in this state.

$$\tau = \frac{1}{\sum_{1}^{n} k_i} \tag{2.12}$$

The natural lifetime of a two-state system is directly connected to the spectral peak width of the radiative transition associated with that state, both for absorption and emission. This connection is known as Heisenberg's uncertainty principle, which connects spatial uncertainty Δx with momentum uncertainty Δp as well as time uncertainty Δt with energy uncertainty ΔE.

$$\Delta x \cdot \Delta p \geq \frac{\hbar}{2} \leq \Delta E \cdot \Delta t \tag{2.13}$$

$$\Delta \nu \sim \frac{\Delta E}{\hbar} \sim \frac{1}{\Delta t} \tag{2.14}$$

Similarly, as absorptions can happen from the ground to the first excited state; absorptions from the first excited state to higher excited states will also be possible, if the Franck–Condon (FC) factors are high enough and the transition is "allowed". This possibility of a radiative transition between excited states technically also holds true for emissions. However, these are usually superseded by faster non-radiative transitions (energy gap law, Kasha's rule).

Besides spontaneous emission, another important transition mechanism stimulated emission. In stimulated emission, if the energy of an incoming photon matches the energy gap of a transition, the emission of a second photon with the same energy can be induced due to a radiative deactivation of the excited molecule. This additional photon is then coherent, i.e., in phase over a long distance, and collinear with the initial photon. While spontaneous emission is a randomly occurring process, stimulated emissions can be actively "forced" to occur and can be faster than the natural lifetime of

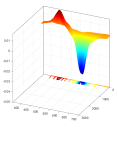

the excited state.

This effect, first described by Einstein in 1917 [41], can be used to create a LASER (light amplification by stimulated emission of radiation), a device first demonstrated in the visible spectrum as a pulsed ruby laser by Maiman [3] in 1960. It is based on the idea that if a group of excited molecules in a medium, the so-called gain medium, is hit by an initial photon, then by consecutive stimulated emissions, an avalanche of photons can be created, and thus the initial photon is amplified. To achieve this avalanche, more molecules have to be in the excited state than in the ground state, also known as a population inversion. When considering a two-state system, with a ground state *1* and an excited state *2* ($E_1 < E_2$), the difference in the number of molecules between the states $\Delta N = N_1 - N_2$ after photoexcitation can never be negative (population inversion), and no laser can be operated on such a system. This is because the probabilities of absorption and stimulated emission (Einstein coefficient B times the applied intensity I) are, even at the highest possible radiation intensity, at maximum only equal, but the spontaneous emission additionally depopulates the excited state regardless, thus, the total depopulation rate of the excited state dN_2/dt always exceeds its excitation rate.

$$\frac{\mathrm{d}N_2}{\mathrm{d}t} = -\frac{\mathrm{d}N_1}{\mathrm{d}t} = B\,I\,N_1 - B\,I\,N_2 - A\,N_2 \tag{2.15}$$

when $I \to \infty$:

$$B\,I\,N_1 = B\,I\,N_2 \tag{2.16}$$

$$\frac{\mathrm{d}N_2}{\mathrm{d}t} = -\frac{\mathrm{d}N_1}{\mathrm{d}t} = -A\,N_2 \tag{2.17}$$

However, in a three-level system with an additional third state *3*, which lies energetically between the previously discussed states, a population inversion is possible. If the rates for excitation (pump) and transition from states *2* and *3* are fast, and the emission between states *2* and *1* is slow in comparison, a population inversion can be achieved via fast pumping and slow deactivation between those levels. The same is true for a four-level system.

Sources to pump a gain medium can be high-intensity flash lamps, laser diodes, or another laser.

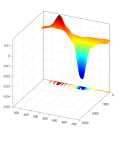

Gain media can be in the solid state (laser crystals such as Nd:YAG or Ti:sapphire, diode lasers, fiber laser), liquid media (dye lasers), or gaseous state (He-Ne-laser). A constructive condition for a laser is the use of highly reflective mirrors. As not all excited molecules can be "collected" in a single pass through the gain medium, the light packages need to travel several times through the gain medium to achieve maximum intensity. This is achieved by placing the gain medium between a set of mirrors (cavity) to send the light packages back and forth through it. Even if the light is trapped between two highly reflective mirrors, with every round trip, the light loses intensity through mirror imperfections, gain medium scattering and absorption. That is why the losses of every round trip need to be much lower than the gains through amplification to create a photon avalanche. When sufficient amplification is achieved, the laser beam needs to be coupled out of the cavity. This can be done passively by a partly transmissive mirror, or actively via polarization switching by Pockels cells. With active switching, also known as Q-switching, the light can be electronically coupled out at the highest intensity, inducing very short laser pulses in the nanoseconds range with very narrow line width. To achieve even faster laser pulses, another technique called "mode-locking" is used. Instead of letting every longitudinal mode in the cavity run freely and out of phase, it is possible to bring all these modes in a fixed phase relation to one another. This can be done by opto-electronic active mode-locking or passive mode-locking via a saturable absorber, thereby inducing constructive interference and extremely short pulses. The more modes or frequencies $\Delta\nu$ that are mode-locked, the shorter the pulse will be (energy-time relationship, see equation 2.14). For a Ti:sapphire laser [7] with a high bandwidth of several hundred nanometers containing several modes, this equates to femtosecond laser pulses, which are spectrally very broad.

The advantages of laser light compared to other light sources, besides the previously discussed extremely short pulses, are their high coherence, collimation, and in part monochromacity. With all these advantages, it is possible to achieve extremely high light intensities, especially when the light is focused on a small area with very short pulse times.

However, despite these advantages, the output wavelength of a laser is fixed by the used gain medium,

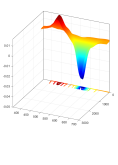

and other techniques must be used to generate laser light of different frequencies than the fundamental laser wavelength. This is achieved via non-linear optical effects. When considering only the linear effects of the time-dependent electric field $E(t)$ on the dielectric polarizability density $P(t)$ of a medium, there is no way that allows the generation of different frequencies through only the linear susceptibility coefficient $\chi^{(1)}$. However, this dependence of the polarizability is only fully described using a Taylor expansion, with quadratic, and higher non-linear terms $\chi^{(2)}, \chi^{(3)}, \ldots$.

$$P(t) \sim \chi^{(1)}E(t) + \chi^{(2)}E(t)^2 + \chi^{(3)}E(t)^3 + \ldots \tag{2.18}$$

Thus, when irradiating a material, with a non-zero non-linear coefficient, by two electric fields (two laser beams) $E_1(t)$ and E_2(t), the non-linear terms for the polarizability density result in new electric fields (laser beams) with frequencies that are different from their fundamental frequencies (inserting equation 2.19 into equation 2.18 gives equation 2.20, with $\omega = 2\pi\nu$):

$$E(t) = E_1\cos(\omega_1 t) + E_2\cos(\omega_2 t) = \frac{1}{2}E_1\exp(-i\omega_1 t) + \frac{1}{2}E_2\exp(-i\omega_2 t) \tag{2.19}$$

$$\begin{aligned} P^{(2)}(t) \sim \chi^{(2)}[&E_1^2\exp(-i2\omega_1 t) + E_2^2\exp(-i2\omega_2 t) \\ &+ 2E_1E_2\exp(-i\underbrace{(\omega_1+\omega_2)}_{\omega_{\text{sum}}}t) + 2E_1E_2\exp(-i\underbrace{(\omega_1-\omega_2)}_{\omega_{\text{diff}}}t)] \end{aligned} \tag{2.20}$$

Among the newly generated frequencies are the doubled frequencies of the two fundamental wavelengths $2\omega_1$ and $2\omega_2$. That means, under the right conditions and with the right material, one can transform a beam of 800 nm light partly into 400 nm light (frequency doubling). The other two new frequencies originating from non-linear optical effects are the sum frequency ω_{sum} and difference frequency ω_{diff}. That means a light beam can be generated, whose frequency is either the sum or the difference of the frequencies of the two original beams, respectively. For a crystalline material to have non-zero non-linear coefficients, it usually requires to lack an inversion symmetry. An example of such a crystal is β-barium borate, a crystal often used for frequency doubling. Although the coefficient is

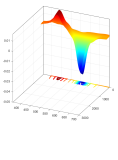

non-zero in this material, it is usually very small and a very strong electric field (high light intensity, i.e., high photon flux) is needed to see any of these non-linear effects emerging. These strong fields can often only be achieved by lasers and not by conventional light sources. Another condition that needs to be satisfied is the so-called phase matching for a non-linear process to occur. Due to this condition, a process can only occur if all the phases of the two or three involved electromagnetic waves match, and thus constructively interfere. That means that the periodic crystal structure of the non-linear material needs to be oriented in the correct angle toward the collinear wavefronts for optimal phase matching. Through this condition, a certain non-linear effect can be favored or chosen by simply adjusting the angle of the crystal.

While these mixing and frequency doubling techniques extend the obtainable wavelength window of a laser source, the laser wavelength remains not freely adjustable. One method of creating a universal laser source is to combine supercontinuum (or white-light) generation (WLG) and optical parametric amplification (OPA), both being another kind of non-linear optical effects. WLG utilizes the phenomenon that, when sending ultrashort pulses through a non-linear medium, a spectrally broad continuum can be generated that can reach a spectral width of several hundred nanometers across the UV, visible, and/or IR range. Common combinations are femtosecond pulses of a Ti:sapphire laser with a CaF_2 crystal (UV/Vis continuum) or a sapphire crystal (Vis-IR continuum). After the WLG is conducted with an energetically minor part of the fundamental laser source, the remaining majority of energy of the beam can be used to amplify a single selected wavelength of the white-light continuum (WLC) via OPA. With OPA, a low-intensity, low-energy/high-wavelength seed beam can be greatly amplified by a high intensity, higher energy/lower wavelength pump beam. This is done by converting some of the pump beam photons into photons that are identical to the entering seed beam, to create an intensified exiting signal beam. The remaining energy of this down-conversion is then transformed into the same number of higher wavelength photons as a so-called idler beam. Thus, the idler wavelength is inversely proportional to the energy difference between the pump beam wavelength and the signal beam wavelength. So, through OPA, a specific wavelength of the WLC can

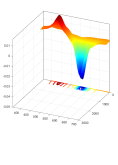

be freely selected and amplified to create a freely tunable laser. Combining all of these methods of frequency manipulation, any desired laser wavelength in the UV to IR can be generated by a series of non-linear conversion steps. However, the efficiency of these conversion processes is usually very low, and a substantial amount of laser intensity is lost on the way from the fundamental to the desired laser wavelength.

2.2 Spectroscopy of Molecules

The previously discussed ideal spectral line widths of atoms and ions are defined by the natural lifetime of the states they are originating from and are the narrowest (lowest ΔE) physically possible. These natural absorption and emission lines exhibit the shape of a Lorentzian profile. However, at room temperature and in solution the atomic, ionic, or molecular spectra are not narrow line spectra, as in the gas phase or at low temperature. Under these conditions, the natural spectral lines are broadened by different effects. One of those effects is Doppler or thermal broadening, by which the atomic or molecular movement relative to the incoming light shifts the needed energy of an absorbed or emitted photon according to the Doppler effect. As the transition wavelength depends on the particle speed and direction, and both of these are randomly distributed in a disordered gas or liquid, this broadening is homogeneous toward both ends of the spectrum and follows a Gaussian distribution. As this broadening is at room temperature and in solution far larger than the natural line width, all spectral peaks follow a Gaussian distribution and can be fitted by a Gaussian function. As this broadening depends on particle velocity, it can be suppressed or at least decreased by cooling the sample.

On top of this broadening, every electronic state is coupled more or less strongly to every vibration of the molecule to form vibronic states. Thus, in the absorption and emission spectra, we can observe not only pure electronic transitions but also vibronic features with consecutive peaks, which are separated by a defined energy which is equal to the energy difference of each vibronic state. As there can be many different vibrations with smaller and larger energy differences in a larger molecule, all these vibronic features may overlap, and the vibronic structure in the spectrum is no longer resolvable, as

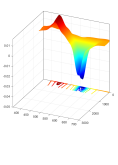

all the peaks are fading into one large spectral peak. Thus, to find the actual energy of the lowest vibronic level of the excited state, we cannot simply use the absorption and fluorescence maxima (as these might be higher harmonics of the vibronic states), but we must use the crossing point between both absorption and fluorescence spectra, which is known as the 0-0 transition. However, if only a few strongly coupling vibrations are present in the molecule, these will dominate the spectrum and give it a defined vibrational structure. This leads to the phenomenon that the fluorescence spectrum should be the mirror images of the corresponding absorption spectrum in a molecule where the ground and excited state exhibit a similar energetic and geometric vibronic structure. This is especially true for rigid molecules, such as anthracene.

However, this mirror image rule is often violated because during the time between absorption and emission, the excited state of a molecule can undergo several processes that transform the excitation energy into thermal or chemical energy, which can change the geometry or chemical composition of the molecule. Due to this energy loss, the emission spectra are generally red-shifted compared to the absorption, which is known as Stokes shift. One of these excited state processes, which is induced by the electron transition and thus charge transfer, is molecule reorganization. As the transferred charge induces or reduces coulomb and exchange interactions, the molecule's structure has to adapt to this new charge distribution by changing its bond lengths and bond angles, to minimize its energy. This can lead to planarization, rotation, or twisting of the molecule. To this class of reorganization also counts a possible internal proton transfer, where a proton is detached from one part of the molecule and attached to another part within the same molecule.

Besides these internal effects, the excited molecule can further interact with its surroundings. As the ground state molecule is in equilibrium with its surrounding molecules, such as solvent molecules, the quick change in charge distribution, alongside change in dipole moment ΔD due to excitation, can severely perturb this equilibrium. In its solvent relaxed (SR) ground state (Figure 2.2.1), the molecules' dipole is aligned with the dipoles of the surrounding solvent molecules. Due to the change in its dipole moment when an electron is transitioning, the molecular dipole might change direction and/or

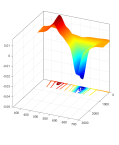

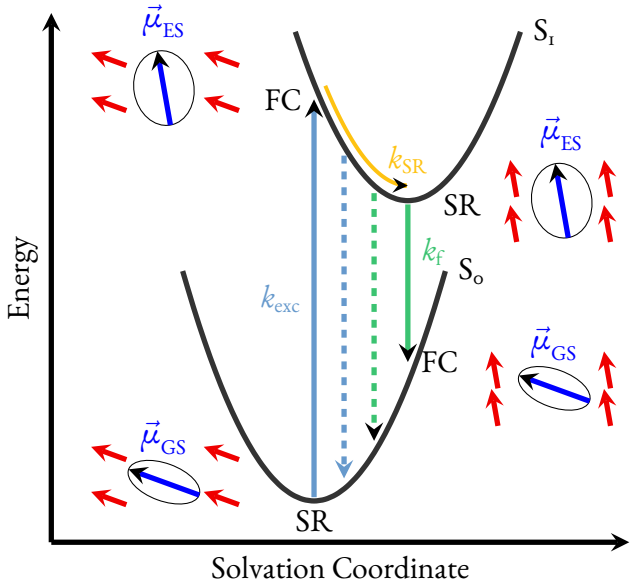

Figure 2.2.1: Illustration of solvent relaxation after excitation of a hypothetical two state chromophore [32]. It shows the change in the chromophore dipole moment orientation and strength $\vec{\mu}$ (dark blue) upon excitation from the ground state (GS) to the excited state (ES) within the solvent cage and solvent molecule dipoles (red) along the solvation coordinate.

strength and is thus no longer in equilibrium with the solvent anymore. This initially formed excited state, without any molecular or geometric adjustments, is called the Frank–Condon (FC) state: An excited state with ground state geometry. Hence, the solvent molecules (and partly the molecule itself) start to rearrange themselves according to the new dipole moments until they reach a new meta stable equilibrium. This rate constant of solvent relaxation k_{SR} depends on the viscosity and thus on the temperature of the sample. In water and at room temperature, this process is usually completed within 200 ps. As this process lowers the energy of the excited state, the energy gap between the excited and ground state decreases and thus the energy of the possibly emitted photon does too. The result is a continuous shift in emission wavelength to higher values (red shift) over the time of the relaxation process. This time-dependent shift in wavenumber $\tilde{\nu}(t)$ from the wavenumber of the FC state $\tilde{\nu}_0$ over time t to the wavenumber of the SR state $\tilde{\nu}_\infty$ can be described via a multiexponential decay law, where each solvent relaxation rate constant $k_{SR,i}$ and pre-exponential factor γ_i are associated with a specific

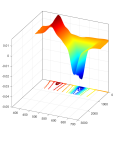

rotation axis of the molecules [32]:

$$\tilde{\nu}(t) = \tilde{\nu}_\infty + \underbrace{(\tilde{\nu}_0 - \tilde{\nu}_\infty)}_{\Delta\tilde{\nu}} \sum_i \gamma_i \exp(-k_{SR,i} t) \tag{2.21}$$

As different solvent molecules have different shapes, these different rotational lifetimes are due to rotations around a certain axis, where some rotations might have a higher friction than others and thus take a longer time to complete (elongated molecule vs. spherical molecule). While the rate constant of the solvent relaxation depends on the solvent's mobility and geometry, the amount of energy decrease $\Delta\tilde{\nu}$ is dominated by the strength of the charge dislocation and redistribution, alongside the solvent polarity. To model the new charge distribution and electromagnetic potential V of a molecule, we can describe it as a series of multipoles and thus as a series of multipole moments.

When the molecule carries a charge, it can be described as its monopole moment and is the strongest in this multipole expansion, as it falls off inversely proportional with distance ($1/r$). If there is no change in net charge present, the next strongest multipole moment is the dipole moment ($1/r^3$), which is usually used for electronic transitions, as no new net charges are formed, but a charge is changing position. The spectral shift in the dependence of solvent polarity is described by the Lippert–Mataga model [42, 43]. It connects the spectral shift with the change in the dipole moment of the molecule and the solvent parameters refractive index n and its dielectric constant ε. However, if the change in dipole moment upon excitation is also zero, for example, due to symmetry, then the shift in the emission has to be explained by the next stronger multipole moment, which is the quadrupole moment ($1/r^5$, Section 3.1.5).

Another major category of excited state processes is excited state reversible or irreversible chemical reactions. Due to the change in charge distribution and orbital occupation, the chemical behavior of a molecule M can severely differ between its excited state and its ground state. These reactions are, like ground state reactions, diffusion-limited and concentration-dependent, as they are all collision-based processes. However, as the excited state lifetime is usually on the time scale of nanoseconds,

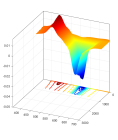

only molecules and reactants in close proximity can diffuse enough in that time frame for a collision and reaction to occur, which is why these processes usually happen only in concentrated solutions with short mean-free-path lengths.

One example of an excited state reaction is the formation (or dissociation) of complexes ML or M^*L, which is for example, not possible or very weak in the ground state. Thus, the magnitude of the complex formation constant K of a molecule in the ground state M and a ligand L can change substantially upon excitation. That means that a system in a ground state complex equilibrium has to adapt and equilibrate toward the new complex formation constant K^* between the excited molecule M^* and a ligand. The activity of a complexed molecule a_{ML} then depends on the activities of the participating molecules:

$$K = \frac{a_{\mathrm{ML}}}{a_{\mathrm{M}} \cdot a_{\mathrm{L}}} \tag{2.22}$$

$$K^* = \frac{a_{\mathrm{M^*L}}}{a_{\mathrm{M^*}} \cdot a_{\mathrm{L}}} \tag{2.23}$$

For a multistage complexation, we can give, instead of the complex formation constant of each complexation step K_{i}, the total complexation constant β_{n} for that stage:

$$\beta_{\mathrm{n}} = \prod_{1}^{n} K_{\mathrm{i}} \tag{2.24}$$

When a usually luminescent molecule forms a new complex with an added ligand or quencher Q in the excited state, this new excited complex might not be luminescent anymore and deactivate via other pathways than luminescence. This is called a static quenching effect, as the luminescence intensity is lowered due to the lower number of free luminescent molecules, but its lifetime remains identical. To quantify this effect, the Stern–Volmer equation [32] for static quenching was developed, where the luminescence intensity without a quencher F_{o} and with quencher F is related to the quencher concentration [Q] to calculate the complex formation constant K_{S} of the excited state molecule and the quencher.

$$\frac{F_{\mathrm{o}}}{F} = 1 + K_{\mathrm{S}}[\mathrm{Q}] \tag{2.25}$$

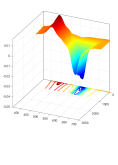

Besides reversible complex formation and dissociation reactions, irreversible reactions are very common as well, especially at high radiation intensities, where the rates of photo-induced reactions are significantly high. Typical reactions can be reactions with dissolved oxygen, which oxidizes and destroys the molecule over time, or bond breakage within the molecule due to the high light intensities.

Another kind of excited state processes are energy transfers. As the excited state carries energy, this energy of the donor (D) molecule can be transferred to another acceptor (A) molecules. The most important mechanisms are the Förster resonance energy transfer (FRET) [44] and the Dexter mechanism [45].

The FRET mechanism is a non-radiative dipole-dipole coupled energy transfer. As no electrons are transferred between the participating molecules and only energy is transferred, the total spin of the system is conserved. The better the energies of the two involved molecule states are matching (spectral overlap integral J) and the smaller the distance r between them is, the larger the rate of the energy transfer k_{FRET} will be. Instead of the rate, the FRET efficiency E_{FRET} is often used, which is defined as the share of the FRET rate constant compared to all deexcitation rates of the donor excited state:

$$E_{\mathrm{FRET}} = \frac{k_{\mathrm{FRET}}}{\sum k_{\mathrm{i}}} = \frac{1}{1 + (\frac{r}{R_0})^6} \tag{2.26}$$

The Förster radius R_0 in this model is defined as the distance at which the FRET efficiency is 50%. This equation further illustrates a power 6 dependence of the FRET efficiency on the distance, meaning that it is a relatively short-range transfer process. The FRET radius can be calculated from the luminescence quantum yield of the donor Q_{D}, Avogadro's number N_{A}, the refractive index n, and the relative orientation of the two transition dipoles to one another κ:

$$R_0^6 = \frac{2.07}{128\pi^5 N_{\mathrm{A}}} \frac{\kappa^2 Q_{\mathrm{D}}}{n^4} J \tag{2.27}$$

with the donor fluorescence intensity at a given wavelength $f_{\mathrm{D}}(\lambda)$ and acceptor extinction coefficient

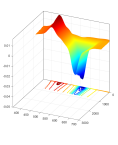

$\varepsilon_A(\lambda)$:

$$J = \frac{\int f_D(\lambda)\varepsilon_A(\lambda)\lambda^4 d\lambda}{\int f_D(\lambda)d\lambda} \tag{2.28}$$

The FRET effect can thus be used as a "nanometer ruler", as the luminescence lifetime and thus the FRET efficiency of a dye depend on the distance r to an acceptor molecule. With a known FRET radius calculated from the single spectra, we can calculate the FRET efficiency of the energy transfer to the acceptor and thus directly calculate the distance r between the two molecules directly from the donor luminescence lifetime.

Conversely in the Dexter mechanism, an electron exchange between the molecules is involved, and thus an orbital overlap between them is necessary. For an orbital overlap, the molecules need to be much closer to each other, and thus the rate of energy transfer drops off exponentially (much stronger than FRET) with distance. The Dexter process can also transfer the energy of an excited singlet state of the donor to the ground state acceptor and excite it. However, a special form of the Dexter process is triplet-triplet-annihilation (TTA) in which two triplet states exchange electrons such that both molecules have singlet multiplicity in the end, leaving one molecule in the ground state and the other in an excited singlet state.

All the collision-based excited state reactions previously discussed, which do not form a complex, are considered dynamic luminescence quenching, as all these mechanisms introduce new excited state deactivation pathways that additionally compete with the luminescence. Any additional deactivation route adds another rate constant, i.e., increases the deactivation probability and thus lowers the excited states lifetime. To quantify the total efficiency of a luminescence process, we calculate or measure the luminescence quantum yield Φ, which represents the number of photons emitted compared to the total number of absorbed photons. This can also be seen as the fraction of the emission rate constant k_f to the sum of all deactivation rate constants k_i of the excited state:

$$\Phi = \frac{k_f}{\sum_n^n k_i} \tag{2.29}$$

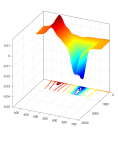

For the dynamically quenched case, the corresponding Stern–Volmer equation considers the luminescence lifetime without the quencher τ_0 and with the quencher τ to determine the quenching rate constant k_q:

$$\frac{F_0}{F} = \frac{\tau_0}{\tau} = \frac{\Phi_0}{\Phi} = 1 + \tau_0 k_q [Q] \tag{2.30}$$

As all collision-based processes are diffusion-controlled, they can be suppressed or at least significantly slowed down by reducing the temperature or raising the viscosity.

To mathematically describe all these kinetics of excited molecules, we can develop complex kinetic models based on differential equations, i.e., the concentration of states versus time, like chemical reaction kinetics. By definition, a reduction in concentration is considered as a negative change, while an increase is defined as a positive change. The rate of change or differential of concentration of a molecule or state A at a given moment in time ($\mathrm{d}[\mathrm{A}](t)/\mathrm{d}t$ or $[\mathrm{A}]'(t)$) is then the probability of a transition or reaction per unit time (k) multiplied by the concentration of molecules in that moment $[\mathrm{A}](t)$. For a simple one-to-one reaction of the form $\mathrm{A} \rightarrow \mathrm{B}$, this ordinary differential equation (ODE) will be:

$$[\mathrm{A}]'(t) = \frac{\mathrm{d}[\mathrm{A}](t)}{\mathrm{d}t} = -k[\mathrm{A}](t) \tag{2.31}$$

When analytically integrating this equation, we obtain an exponential decay law for the concentration over time with a starting concentration $[\mathrm{A}](t{=}0) = [\mathrm{A}]_0$:

$$[\mathrm{A}](t) = [\mathrm{A}]_0 \exp(-kt) \tag{2.32}$$

As for many methods, the signal intensity is directly proportional to the analytes or excited molecules' concentration ($I(t) \sim [\mathrm{A}](t)$), we can use this equation to directly fit an intensity-time graph to this equation to determine the rate constants from time-resolved luminescence spectroscopy. A fit of an equation to noisy experimental data points is most often done in software, where an algorithm compares the values of the mathematical fit function to the data points. The aim of this comparison is to minimize the difference between the mathematical fit function and the data points, very often by min-

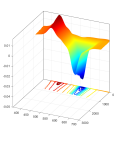

imizing the least-square difference between the two. This is done by varying the values of parameters like k and $[A]_0$ until a convergence criterion is reached.

For simple systems, as in this example, an easy-to-calculate and easy-to-use mathematical expression for the integrated form can be found analytically. However, once more complex systems with several reaction partners and deexcitation mechanisms are investigated, such as excited state equilibria, it is extremely difficult or even impossible to find an analytical solution for systems of ODE's without assumptions, approximations, and simplifications. As processing power is nowadays cheap, modern algorithms do not solve differential equations analytically, but numerically. So, instead of integrating the full ODE system one by one, the algorithm simply calculates the changes/differentials in concentration at each moment in time according to the differential equations and then moves with these new concentrations to the next time step. The smaller the chosen time-step interval, the better the numeric solution will be. A sophisticated numeric calculation is often much more precise than an approximated analytical solution, but will never reach the accuracy of a full and unconstrained analytic solution.

2.3 Spectroscopic Methods and Data Evaluation

The instrumental toolbox for investigating the ground and excited states of molecules using optical spectroscopy is large and methods have to be chosen well to fit the application and sample system. A fundamental and one of the oldest methods to analyze the electronic structure of a molecule is absorption spectroscopy in the ultraviolet (UV), visible (Vis), and infrared (IR) range. Absorption spectroscopy of molecules or ions give how strong and at which energy (wavelength) light is absorbed. To do this, an optical spectrometer usually irradiates a sample with light of a specific wavelength λ and compares the intensity before it enters the sample I_0 with the intensity after leaving the sample I, which makes it a transmission technique. The connection between the concentration of molecules c in the sample, their decadic extinction coefficient $\varepsilon(\lambda)$, the path length or sample diameter d, and the logarithmic ratio of intensities (also known as absorbance A or optical density OD) is described by

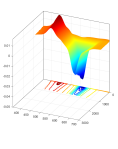

Lambert–Beer's law and holds true for low intensities, non-scattering media, and low concentrations:

$$\mathrm{OD}(\lambda) = \mathcal{A}(\lambda) = \lg \frac{I_0(\lambda)}{I(\lambda)} = \varepsilon(\lambda) c d \tag{2.33}$$

By scanning over every desired wavelength, we can generate an absorption spectrum and calculate extinction coefficients if the concentration is known. The extinction coefficient is directly connected to the Franck–Condon factor of that transition.

To select wavelengths from a spectrally broad emission source (such as a Xenon arc lamp), a dispersive element is used. These can be prisms or, mostly commonly today, diffraction gratings. The periodic structure or lines of a diffraction grating create an interference pattern by which the grating deflects the light wavelength and angle dependent, thereby separating the light by energy. Through a narrow slit and the angle of the grating, a specific wavelength can be chosen and sent through or onto the sample. To measure the amount of photons or intensities of light, nowadays electronic detectors are used. Typical detectors and enhancers in spectroscopy are photomultiplier tubes, microchannel plates, and charge-coupled devices (CCD).

On the other hand, to measure the excited state as steady state (non-time-resolved) fluorescence spectra, a similar setup is used. The big difference is that two gratings are used, one for the excitation path and the other for the emission path. Furthermore, the excitation and emission light paths are orthogonal to one another to minimize scattering effects in the emission path. To generate an excitation spectrum, the emission wavelength is set to a fixed position, and the excitation grating is driven through all the desired wavelengths, and vice versa for an emission spectrum.

The two most common methods for time-resolved luminescence measurements are time-correlated single photon counting (TCSPC) and time-resolved laser fluorescence spectroscopy (TRLFS) in box-car mode. In TCSPC, the sample is excited by, for example, a short-pulse laser diode at a fixed laser wavelength, after which the system counts the time until a photon arrives at the detector. This duration is sorted into a corresponding time channel. This is usually repeated for many thousand photons until a luminescence intensity-time-curve is generated. This curve is at short times convolved with the

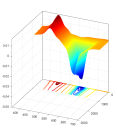

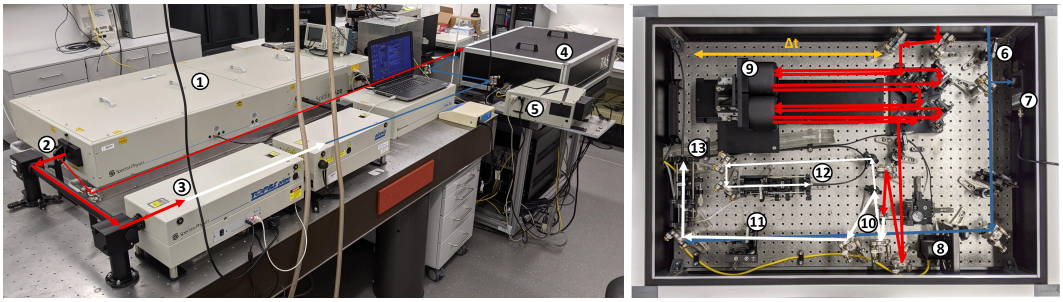

(a) Spitfire Ace and TAS laser setup.

(b) TAS internal beam path.

Figure 2.3.1: Experimental setup for TAS measurements. 1 – Spitfire Ace, 2 – Beam splitter for pump and probe, 3 – TOPAS, 4 – TAS, 5 – TAS spectrograph, 6 – Pump beam with ND-filter wheel, 7 – pump reference detector, 8 – chopper, 9 – delay stage, 10 – CaF_2 crystal, 11 – sample holder, 12 – probe reference channel, 13 – probe sample channel

laser pulse time profile and needs to be deconvolved software wise. As the emission is measured only at one wavelength, only temporal and no spectral information are collected. In TRLFS, a much more sophisticated setup is usually used, with a tunable laser source (for variable excitation wavelengths) coupled to a spectrograph with a CCD camera as a detection system. In this method, with each laser shot a full emission spectrum is detected simultaneously via a CCD detector array at an electronically fixed delay time window (box). After accumulating and averaging many spectra over several laser shots, this delay time window is shifted to the next time instance. By this method, not only the evolution of the luminescence intensity is recorded over time, but the evolution of the whole emission spectrum as well.

As these time-resolved techniques require the excited state to be luminescent, only a few optically active materials or excited states can be investigated by these approaches. Hence, pump-probe experiments are widely used in cases, where no or weak luminescence is observed. Compared to luminescence measurements, in pump-probe experiments, we do not wait passively for a response of the system by itself (emission of a photon) after pumping the sample by an initial pump pulse but actively probe the sample with a second laser beam at a specific point in time to analyze its current state. One of those techniques is the so-called transient absorption spectroscopy (TAS, Figure 2.3.1). As the name suggests, this method uses absorption or UV/Vis spectroscopy to investigate short lived, i.e., transient, electronic states or molecules. In this technique, the change of the absorption spectrum upon irradia-

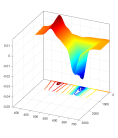

tion by the pump pulse is measured. Thus, the difference in optical density ΔOD between the optical density after (OD_P) and before (OD_{NP}) of the pump pulse's arrival is the detected signal.

$$\Delta OD(\lambda) = \Delta \mathcal{A}(\lambda) = OD_P(\lambda) - OD_{NP}(\lambda) \tag{2.34}$$

Besides spectral information, we can gain temporal information by varying the time delay between the pump pulse and the probe pulse. By sequentially collecting spectra at each of those delay times Δt we generate a typical two-dimensional TAS spectrum. The time delay between both pulses is achieved by letting one of the pulses travel a longer path than the other one. Thus, by sending one of the laser beams over a movable delay stage with retro-reflectors (9 in Figure 2.3.1), we can increase the travel distance and thus the travel time of one of the beams electronically. Hence, the time resolution of the system is defined by the spatial resolution of the delay stage via the speed of light. A time delay of 1 ns is equivalent to a path length difference of about 30 cm, and the maximum possible delay is limited by the total distance the beams can stay aligned. Thus, microsecond delays would be extremely difficult to achieve and are considered impractical, and measuring time windows of a few nanoseconds are realistic. As a light source for both pump beams a Ti:sapphire laser (1 in Figure 2.3.1) can be used, which is split into a high-energy beam and a low-energy beam. The high-energy beam is used in an OPA to generate pump light (3 in Figure 2.3.1) and is usually operated in the UV region, to avoid interference of the pump light with the detection system in the visible range. The low-energy beam is sent over the movable delay stage and afterwards focused into a CaF_2 crystal for WLG as a broadband probe beam (10 in Figure 2.3.1). Both beams are then focused and overlapped into the sample (11 in Figure 2.3.1). While the residual pump light is dumped after the sample, the probe beam is sent via fiber optics into a spectrograph with a CCD detection array (13 and 5 in Figure 2.3.1). This way, with each probe laser shot, a whole white-light intensity spectrum is measured simultaneously, instead of sequentially scanning over all wavelengths, as in a classic absorption spectrometer. As both pumped and non-pumped optical densities are connected via the Lambert–Beer's law and are then subtracted from one another, it is not necessary to measure the initial white-light intensity at each wavelength

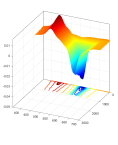

$I_0(\lambda)$, as only the ratio between the intensity before and after the pump pulse, $I_{NP}(\lambda)$ and $I_P(\lambda)$ respectively, after the sample is relevant:

$$\Delta OD(\lambda) = \lg \frac{I_0(\lambda)}{I_P(\lambda)} - \lg \frac{I_0(\lambda)}{I_{NP}(\lambda)} \tag{2.35}$$

$$\Delta OD(\lambda) = \lg \frac{I_{NP}(\lambda)}{I_P(\lambda)} \tag{2.36}$$

To measure a sample once with and without a pump pulse, the pump pulse is sent through a chopper wheel, which is synced to half of the laser repetition frequency. That means that the pump beam is blocked by a chopper blade on every other shot, while the probe light reaches the sample on every laser shot. With this setup, we can measure a whole ΔOD spectrum with each laser shot pair and integrate easily over many thousand shots.

The full 2D TA spectrum is generated by moving the delay stage to a fixed position and by measuring and integrating the TA spectrum at this time delay. Once the integration time is reached, the stage can be moved to a new time/delay position, and a new spectrum is collected. In this sequential mode, every delay time can be scanned, and a full 2D scan of the sample can be received. Measuring the sample in that manner means, that TAS is not actually measured on the femtosecond timescale for each shot but uses an ensemble of different laser shots over several minutes to recreate the ultrafast processes and information. Parallel to integrating each delay position, we can also integrate several full 2D scans into a single 2D spectrum by averaging over all scans. The combination of both integration modes vastly improves the signal-to-noise ratio as numerous shot-to-shot laser power fluctuations and other, more periodic power fluctuations, such as white-light crystal driving, are averaged out.

Due to the complex nature of this method, various signal types can be detected. For example, when exciting a significant portion of molecules in a sample, a decrease in the strength of the absorption bands of the ground state in the absorption spectrum can be observed. This is due to fewer molecules being present in the ground state. As the sample has been bleached by the pump pulse before the arrival of the probe pulse, the change in absorption is negative and thus a negative peak is present

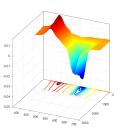

in the ΔOD spectrum. The shape of the ground state bleach (GSB) signal is then the negative mirror image of the absorption peak in a linear absorption spectrum. As previously discussed, when a molecule is excited, it can be further excited to an even higher electronic state or undergo chemical reactions. In any case, now a new molecule, a new molecule state, or a new molecule complex can be present, which has been absent before the arrival of the pump pulse. This new species can have its own very distinctive absorption spectrum and generate an additional absorption band that has not been present before the pump pulse. Thus, any new transient absorption (TA) shows up as a positive peak in the ΔOD spectrum. A third type of signal that is common in TAS is stimulated emission (SE or fluorescence f). When molecules are in an excited state, an incoming laser pulse, the probe beam, can stimulate the emission of another photon in those molecules. As these emitted photons are collinear to the stimulating beam, they follow the exact same path into the detector as the rest of the probe beam and can be detected there. The additional intensity that arrives at the detector appears as if the sample became more transparent at these wavelengths, thus as if the absorption of the sample decreased by the pump pulse, thereby inducing a negative ΔOD signal. However, spontaneous emission is not detectable in TAS, as the photons are randomly emitted in all directions around the sample and are unlikely to hit the detector. For the generation of the pump beam and white light, several stages of non-linear processes are used, and the whole laser system and spectrograph are extremely sensitive to intensity fluctuations of the fundamental laser source. These pulse-to-pulse fluctuations originate from slight air density, temperature, and humidity changes due to air conditioning or other airflow or heat sources, such as chillers and heaters. These minuscule fluctuations of the fundamental laser intensity can severely reduce the signal-to-noise ratio of the spectrometer, and it is critical to compensate those fluctuations. That is why two reference systems were installed: One for the probe beam and the other for the pump beam. For the pump beam, a small amount of intensity of the pump beam was sampled and sent onto a photodiode (7 in Figure 2.3.1) to measure the pump beam intensity fluctuations. When the intensity deviates too much from the expected intensity, the corresponding transient absorption spectrum is rejected and will be remeasured. This way, bad or deviating pump pulses are

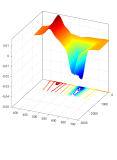

filtered. For the probe beam, the white light is sampled as well after the white-light crystal (10 in Figure 2.3.1), where the high-intensity beam is sent through the sample, and the low-intensity path is sent into a reference channel (12 in Figure 2.3.1). The same rejection function is available, where too high derivation of the expected white-light spectrum is rejected. However, compared to the pump light reference channel, the measured spectra can also be intensity corrected on top, which vastly improves the signal-to-noise ratio of the system. Both probe signals are sent via a Y-fiber to the spectrograph to do this referencing on the software side.

The large amount of two-dimensional data (matrices) generated by TAS can become extremely difficult to view, analyze, and interpret very fast, as each contained molecule can have several electronic states, each with its own TA and GSB and different extinction coefficients. Also, each of those states and species can participate in the excited state reactions to form even more molecules and electronic states. Furthermore, the kinetics of these states can be rather complicated too, as they all might be coupled to one another via equilibria. When additionally measuring TAS in dependence of a third parameter, such as pH, concentration, excitation energy, or temperature, the resulting three dimensional data cube (tensor) can contain several gigabytes of data points. Therefore, it is extremely important to deconvolve these extremely complicated spectra into different components or species, each with its own unique spectrum and time profile. Each component or species can be a certain electronic state of a molecule that is behaving temporally different from the others. For this deconvolution problem, the Parallel Factor Analysis (PARAFAC) algorithm of Bro et al. [46] can be used, which is coded in the N-way toolbox in MATLAB [47]. The PARAFAC model assumes, that the total spectrum, matrix, or tensor Y is a linear combination or superposition of several components F, each with its own unique spectrum, time profile, and third parameter profile tensor f plus an error tensor E (Figure 2.3.2 and eq. 2.37). The PARAFAC algorithm varies the single-component tensors to minimize the least square difference to the given data points and outputs the final single-component tensors after reaching convergence.

$$Y_{ijk} = \sum_{f=1}^{F} a_{if} b_{jf} c_{kf} + E_{ijk} \tag{2.37}$$

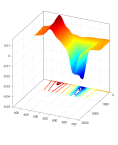

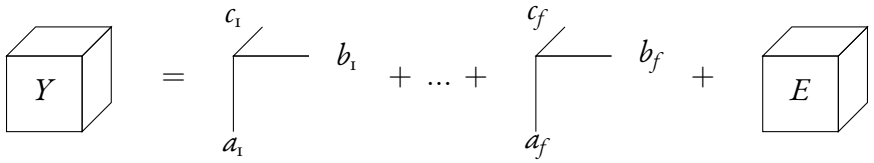

Figure 2.3.2: Visualization of the PARAFAC model. Data tensor Y is a linear combination of tensors f of different factors F and an error tensor E [46].

The major advantage of PARAFAC is the possibility of efficient multidimensional deconvolution. While more common deconvolution techniques, such as singular value decomposition or principle component analysis, are limited to two-dimensional data or matrices only, PARAFAC can deconvolve any N-dimensional tensor with many possible measuring parameters in one dataset. With this deconvolution, the amount of data is massively reduced, and the spectra are no longer superimposed; thus, all electronic states and species can be separated from one another. However, when two species are, for example, kinetically coupled, PARAFAC might interpret those coupled species as one single component and mixes the corresponding tensors. As any high parameter algorithm can converge into a local minimum without any chemical or photo physical meaning, it is necessary to control the gradient descent of the algorithm by constraining the possible solution space. For example, time and concentration profiles can only have positive values, so the PARAFAC algorithm can be constrained for these dimensions to only generate non-negative values. Once the PARAFAC algorithm converges, it gives a trust value for the probable number of components within the data — the so-called "core consistency". With this value, the correct number of components, besides only comparing the results with the raw data, can more confidently be chosen. After the deconvolution process, each spectrum can be analyzed separately, and complex kinetic models can be fitted to the separated time traces.

To support the results from TAS measurements, detailed knowledge about the electronic structure, orbitals, and electronic states of the involved molecules is necessary, to understand electron transitions and multipole moment changes upon excitation. Therefore, besides other techniques, time-dependent density functional theory (TD-DFT) can be used to calculate, via quantum mechanics, the energies and electron distributions of molecules. This way, excitation spectra and vibrational frequencies can be predicted, alongside excited and ground state geometries. One implementation of

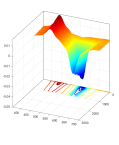

TD-DFT can be found in the ORCA package by the MPI für Kohleforschung [48, 49]. Depending on basis set, functionals, and approximations used, the quantitative error in those calculations can be relatively large, while the qualitative information is usually correct. Among these approximations is the description of the solvent cage as a conductor-like polarizable continuum model (CPCM), to avoid calculating hundreds of solvent molecules individually. Another common approximation is to use harmonic, instead of anharmonic, vibronic potentials, where the latter usually underestimates bond lengths and overestimates vibronic energies. Despite these weaknesses, without these fundamental quantum mechanical considerations, it would be complicated to interpret transient absorption spectra.

2.4 Organic Dyes and their Applications

Organic dyes comprise, compared to inorganic dyes, mostly out of carbohydrates with oxygen, nitrogen, and sometimes sulfur functionalization. The most important characteristics of a dye are its spectroscopic properties, such as absorption and luminescence. The higher the extinction coefficient of a dye, the stronger its color and thus its potential as application as a dying agent, as less dye is necessary for the same amount of coloration. That is why high-performance dyes have extinction coefficients of several thousand L $mol^{-1}cm^{-1}$ [8]. This remarkable absorption quality of organic dyes is realized by the alternation of single and double carbon bonds (sp^2 hybridized carbon atoms) to form large conjugated electron systems, for example, by connecting several aromatic rings into a larger aromatic ring system. The longer the conjugated electron system in those molecules is, the longer is the wavelength of photons that the molecule absorbs. A classic example of these molecules are polycyclic aromatic hydrocarbons (PAH), such as pyrene and anthracene [50]. In anthracene three aromatic rings are linearly fused into one aromatic system. However, as this ring system is rather small, only short wavelength, i.e., high energy, photons are absorbed, which is why it shows absorption in the UV range, while it emits in the blue part of the electromagnetic spectrum. However, to better adjust the spectral properties of organic dyes, it is common to substitute aromatic ring hydrogens by electron pushing

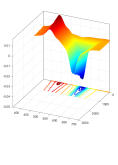

or withdrawing substituents like halides, aldehyde groups, and more. The closer this substitution is to the chromophore's transition dipole, the stronger the effect of the electron density adjustment and thus spectroscopic change. When an electron pushing group on one side of the molecule is combined with an electron withdrawing group on the other side of the molecule, a push-pull effect can be used to further modulate the spectroscopic properties [12]. Both effects influence the ground and the excited state energy alongside the energy gap between the two; thus, not only absorption but also emission properties can be managed by this. This change in spectroscopic properties is partly due to changes in the polarity of the molecule itself, as a change in the polarity of the ground and/or the excited state changes the energy of the states in its solvent environment [51]. This effect is called solvatochromism, in which negative solvatochromism is explained as a hypsochromic shift in the absorption band. This occurs when the ground state is very polar compared to the excited state and is thus stabilized in polar solvents, inducing a larger energy gap to the excited state and thus a decrease in absorption wavelength. Positive solvatochromism, however, is present when a bathochromic shift occurs, as the excited state is more polar compared to the ground state. Thus, it is stabilized/lowered in energy in polar solvents, the energy gap between the two states is decreased, and absorption occurs at a higher wavelength [32].

By substitution of hydrogen with heavy elements, such as iodine, the heavy-atom effect can be used to increase spin-orbit coupling and thus increase ISC in the dyes, to increase triplet formation. However, although more triplet state molecules are formed, organic dyes rarely emit phosphorescence at room temperature, as the large number of vibrations in those large molecules open various pathways to deactivate these triplets (high final state density, Fermi's golden rule, eq. 2.11).

Anthracene is often substituted in the 9,10-position (ring center, Figure 2.4.1, left), as this position is closest to the transition dipole. As substituents, several inorganic and organic groups can be used [52], such as phenyl rings to obtain 9,10-diphenylanthracene (DPA), or pyridyl rings to obtain 9,10-dipyridylanthracene [16]. The substituent can also be used to simultaneously tune the solubility of the dye, as polar or protonatable substituents (like a carboxylate group) on non-polar dyes increase their solubility in polar solvents. This way, an anthracene-based dye can be dissolved in sufficient quantities

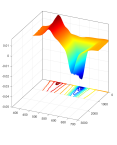

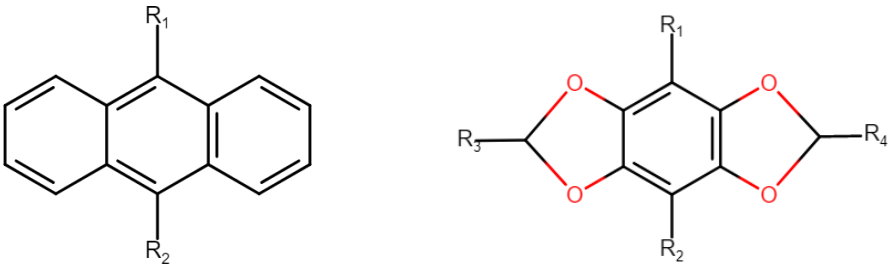

Figure 2.4.1: Left: General structure of a 9,10-substituted anthracene. Right: General structure of a DBD dye core with possible substituent positions R_1–R_4.

in water or alcohols.

Another relatively new and promising organic dye class is the so-called [1,3]dioxolo[4,5-*f*][1,3]benzodioxole (DBD) dye [11], with a benzene core that is bridged on each side by two dioxol groups, thus having a central carbon six ring and two outer five rings with oxygen hetero-atoms (Figure 2.4.1, right). This DBD core can be modified, depending on the synthesis route, or substituted after synthesis [12] at four possible locations R_1–R_4, to adjust absorption, emission, and solubility parameters. This way, the absorption can be tuned over a few hundred nanometers, while the range for emission can be even greater depending on the solvent. Typical substituents can be aldehyde or carboxylate groups, as well as longer alkyl or lipid chains, or any combination of the above to give asymmetric substituted DBD dyes. The good solubility (depending on substitution), good luminescence quantum yield, flexible emission wavelength, and luminescence lifetime make them an amazing tool for luminescence applications, as the dye can be relatively easy designed and uniquely modified to fit the application instead of adjusting the application to the available dye. Recently, the class of DBD dyes has been extended by substituting the oxygen atoms by sulfur to give S^4-DBD dyes, with even further red shifted luminescence spectra but lower luminescence quantum yield [15].

One main application of organic dyes are as gain media in dye lasers [53] and for microscopy tech-

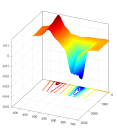

niques. DBD dyes can, for example, be synthesized in such a way that they are integrated at different positions into biomolecules like lipids, which can then be used to investigate membrane structures using fluorescence microscopy [14]. Dyes are also valuable as pH [54], temperature, or oxygen sensors [55], where lifetime or spectral changes can be used to observe changes in the sample matrix for industrial or medical parameter observations.

2.5 Uranium and the Uranyl(VI) Molecule

Uranium is a radioactive heavy metal in the group of the actinoids and thus belongs to the f-element group. With a half-life of several billion years for the most abundant isotope ^{238}U [56], it is one of the longest-lived radioactive elements known. Furthermore, it is, besides thorium, radium, and radon, one of the most abundant radioactive materials on earth and can be found in many soils and stone formations, like granite. In these natural sources of uranium, basically only two oxidation states can be found: The uranium(VI) oxidation state under aerobic and the uranium(IV) oxidation state under anaerobic conditions [57]. Besides the occurrence in rocks and soil, these oxidation states can be dissolved into water due to soil degradation and washing out by rain or ground water. Under aerobic conditions, the uranium(VI) is found in solution as the linear uranyl(VI) oxygenated molecule UO_2^{2+}, while under anaerobic conditions uranium(IV) is found as the "free", only water solvated U^{4+} ion (Figure 2.5.1). However, the solubility of U(IV) in non-acidic aqueous environments is rather low; thus, reduction can be used for immobilizing the highly solvable uranyl(VI) ion [58, 59]. Due to its heavy metal character, it is highly chemotoxic, adding to its radiotoxicity, and is dangerous for all forms of life [17]. The release of uranium into ground and surface water bodies is further accelerated by human ore mining and processing operations, either by directly mining for the uranium ore itself or by being contained in other metal ores and brought to the surface. Historically, uranium found its application as a coloring agent in glasses. However, nowadays, the technical application of uranium is mainly based on energy production as fuel in nuclear power plants [60].

Both naturally occurring oxidation states of uranium exhibit absorption and luminescence prop-

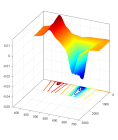

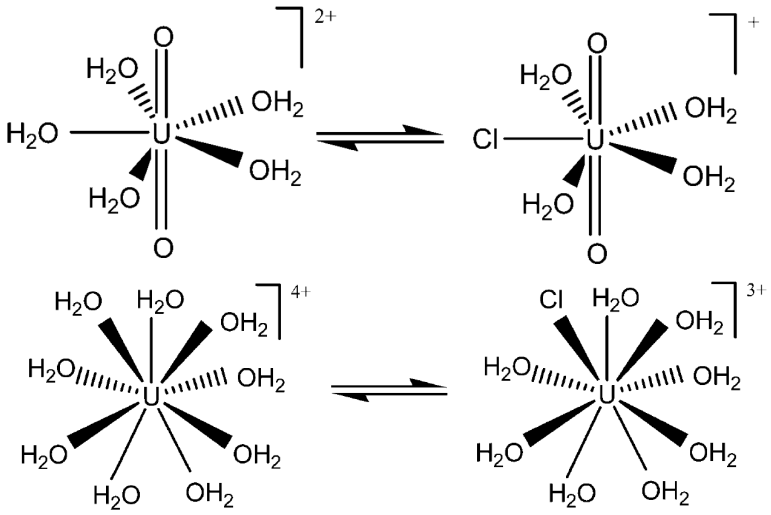

Figure 2.5.1: Complex structures of uranyl(VI) (top) and uranium(IV) (bottom) of the "free" aquo ions and the first chloride complexes [61].

erties. But due to the forbidden character of those singlet-triplet and f-f transitions, this results in low extinction coefficients but long excited state and luminescence lifetimes [62].

However, for the linear uranyl(VI) molecule, the forbidden character of those transitions is slightly lifted, the extinction coefficient in the visible range remains low with about 9 $M^{-1}cm^{-1}$ [63]. The ground state of the uranyl(VI) is a $^1\Sigma$ state that has several U-O vibration modes, for example, the symmetric and asymmetric stretching modes. These modes are also present in the lowest energy excited states $^3\Delta$ and $^3\Phi$, which can be reached by excitation in the visible range at around 410 nm. This leads to the usual yellow color of many uranyl(VI) compounds. Upon this excitation, an electron is transferred from the $3\sigma_u$ molecular orbital, comprising mainly of U(5f)-O(2p) atomic orbitals, to the atomic U(5f) orbitals $1\delta_u$ or $1\varphi_u$, respectively [64]. This transition from a more outer-lying MO to the metal center AO leads to an asymmetric U-O bond elongation on one side of the molecule, reducing its symmetry [65]. The $^3\Delta$ state has been identified as the origin of the luminescence of uranyl(VI) in water [66] — a property that is known for uranium ores and compounds for more than hundred years [67]. This emission is present at around 500 nm, depending on the observed complex or mineral, giving it a green color. The lifetime of the excited uranyl(VI) aquo-ion lies in the range

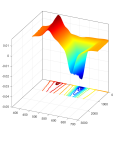

of a few microseconds [62], which might be quenched in the presence of quenching ions like halides [24] and oxidizable metal ions [22]. The absorption and the emission spectrum are dominated by U-O vibrations, inducing a peak progression where the peak distances are equal to the energy of a vibrational mode. For the absorption spectrum this peak progression resembles the vibrations of the excited states, whereas in the emission spectrum, this progression resembles the ground state vibrational energies. Furthermore, a hot-band is visible in the emission spectrum, showing emissions from the first excited vibronic state of the emitting $^3\Delta$ state due to the thermal population of this vibronic level. As expected, this hot-band disappears when cooling the sample as the population of this first vibronic state vanishes. Higher excited states are the $^1\Delta$, $^1\Phi$, $^3\Pi$, and $^3\Gamma$ that can be reached via excitations in the UV range [66]. Both absorption and emission are sensitive to the ligand or crystal field surrounding the ion. In solution, the ligands of uranyl(VI) are arranged in the equatorial plane of the linear molecule, usually forming pentagonal bipyramidal complexes with D_{5h} point group in the case of five monodentate ligands (Figure 2.5.1, top). The "free" uranyl(VI) aquo-complex $[UO_2(H_2O)_5]^{2+}$ is thus surrounded by five solvent molecules under acidic conditions. However, at higher pH values, the uranyl(VI) starts to hydrolyze, meaning abstracting hydroxide from water molecules and forming uranyl(VI) hydroxo complexes starting at pH 3 and higher [21]. In these, one or more water ligands are replaced by hydroxide ligands, which lowers the symmetry of the complex. The first hydroxo-complexes are the 1:1, 1:2, and 1:3 uranyl(VI) aquo-complexes, namely $[UO_2(H_2O)_4(OH)]^+$, $[UO_2(H_2O)_3(OH)_2]^0$, and $[UO_2(H_2O)_2(OH)_3]^-$, respectively [21]. Some of the most important ligands of uranyl(VI) are halides (like chloride and bromide), carbonate, sulfate, phosphate, and organic acids, such as amino acids and peptides [68]. While the halides are only monodentate ligands, the latter can be mono- or bidentately attached to the uranyl(VI). Depending on the size and denticity of these ligands, the coordination number might vary, for example, in the 1:1 uranyl(VI) halide complexes $[UO_2(H_2O)_4X]^+$, five ligands are present in C_{2v} symmetry, while for the 1:2 uranyl(VI) halide complex $[UO_2(H_2O)_nX_2]^0$, the number of water molecules n can be 2 or 3 [69]. At $n = 2$, a higher D_{4h} symmetry is achieved, with only four ligands in total.

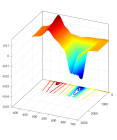

Compared to uranyl(VI), the uranium(IV) ion has no bound oxygen and thus has much more space for additional ligands (Figure 2.5.1, bottom). U(IV) also exhibits a much larger extinction coefficient of 59 $M^{-1}cm^{-1}$ in the visible spectrum at 650 nm [70] but a much shorter luminescence lifetime of less than 20 ns at room temperature [71]. The fundamentally different optical properties make it easy to differentiate between both oxidation states using optical spectroscopy.

Under rare conditions, uranyl(V) can be observed as an intermediate oxidation state. Uranyl(V) is a very unstable oxidation state of uranium, which quickly disproportionates into uranium(IV) and uranyl(VI) [72]. It is structurally similar to uranyl(VI) with two bound oxygen atoms, however, it is an angled and not linear molecule. Only under precise electrochemical conditions [73] or with very special, stabilizing ligands [74], it is possible to hold uranyl(V) in aqueous solution for long periods of time.

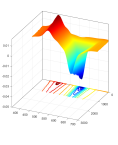

No great discovery was ever made without a bold guess.

Sir Isaac Newton

3

Manuscripts

In the following chapter, the publications of this thesis are presented and are ordered chronologically by publication date. Each manuscript is preceded by an overview of my personal contribution to the publication.

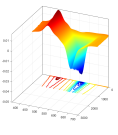

3.1 Photophysics of Acyl- and Ester-DBD Dyes: Quadrupole Induced Solvent Relaxation Investigated by Transient Absorption Spectroscopy

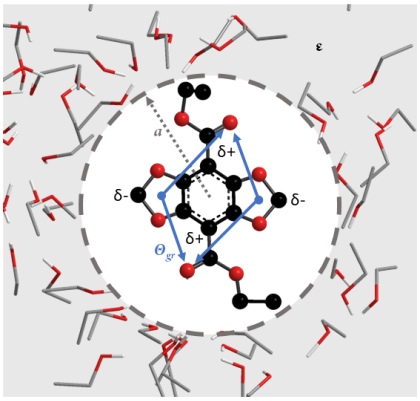

Figure 3.1.1: TOC graphic of "Quadrupole-Induced Solvent Relaxation Investigated by Transient Absorption Spectroscopy".

Haubitz, T., John, L., Wessig, P., & Kumke, M. U., Photophysics of Acyl- and Ester-DBD Dyes: Quadrupole-Induced Solvent Relaxation Investigated by Transient Absorption Spectroscopy. *Journal of Physical Chemistry A*,2019, *123*(22), 4717–4726.

Personal Contribution:

The samples in this manuscript were synthesized and provided by the "bioorganic chemistry" department of Prof. P. Wessig by L. John. All transient absorption measurements, data evaluation, Togashi-model development, tables, and graphs were done by myself. Furthermore, the large majority of the data interpretation, discussion, conclusions, and the writing of the manuscript were done by me.

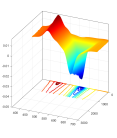

Photophysics of Acyl- and Ester-DBD Dyes: Quadrupole Induced Solvent Relaxation Investigated by Transient Absorption Spectroscopy

Toni Haubitz, Leonard John, Pablo Wessig, and Michael U. Kumke

University of Potsdam, Institute of Chemistry, Karl-Liebknecht-Str. 24-25, D-14476 Potsdam, Germany

3.1.1 Abstract

A new generation of wavelength-tunable, fluorescent dyes, so called DBD ([1,3]dioxolo[4,5-*f*][1,3] benzodioxole) dyes, was developed a few years ago and showed great potential as probes, e.g. for fluorescence microscopy. However, their photophysics is not fully explored and leaves open questions regarding their large fluorescence Stokes shifts and sensitivity to solvent conditions of differently substituted DBD dyes. To improve the understanding of the influence of the substitution pattern of the DBD dyes on their respective photophysics,Transient Absorption Spectroscopy (TAS) was used, a pump-probe experiment on the femtosecond timescale. TAS allows measurements of excited states, ground state recovery, solvent relaxation, and fluorescence properties on time scales of up to several nanoseconds. Two different DBD dye samples were investigated: an Acyl- and an Ester-substituted DBD dye. Experiments were carried out in solvents with different polarities, using different excitation energies, and at different viscosities. Based on the experimental data and theoretical calculations we were able to determine the conformational changes of the molecule due to electronic excitation and were able to investigate solvent relaxation processes for both type of DBD dyes. By generalizing the theory for quadrupole induced solvent relaxation developed by Togashi et al., we derived quadrupole moments of both molecules in the ground and the excited state. Our data showed differences in the binding of polar solvent molecules to the dyes depending on the substituent on the DBD dye. In the case of water as solvent, an additional efficient quenching process in the electronically excited state was revealed, which was indicated by the observation of solvated electrons in the TAS signals.

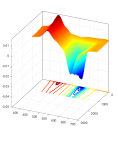

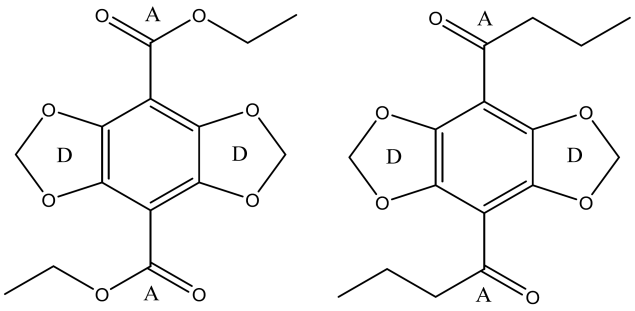

Figure 3.1.2: Chemical structures of the trans-Ester-DBD dye (left) and the trans-Acyl-DBD dye (right). Dioxol rings function as electron donor (D) groups, while carbonyl groups function as electron acceptor (A) groups.

3.1.2 Introduction

For modern microscopy and probing applications it is necessary to have access to a dye tool box, absorbing and emitting at desired wavelengths with a reasonable long luminescence lifetime, high quantum yield and photostability as well as tailored chemical properties. Especially the demand for new candidates that can be excited by using two-photon absorption is steady increasing driven by the demand of biological and clinical imaging applications which often require a decent light penetration depth into tissue samples [1, 2, 3].

A promising new dye class is based on the so called DBD ([1,3]dioxolo[4,5-*f*][1,3]benzodioxole) scaffold [4]. It has been shown that these dyes can be finely tuned in their photophysical properties by substituting the chromophore skeleton with electron accepting groups, which also allows for solubility adjustments [5]. Moreover, different functional groups for conjugation to biological-relevant molecules can be introduced making DBD dyes a powerful new class of optical probe molecules. Meanwhile a range of applications of DBD dyes was developed. Thus, they were used as probes to study conformational changes in proteins [4, 6], in fluorescence-lifetime-based assays [7, 8], in various FRET pairs [9, 10, 11, 12, 13], in potassium selective probes [14], and probes to selectively detect double-stranded DNA [15]. Recently we reported on further development in the synthesis of DBD dyes facilitating the adjustment of photophysical parameters to the requirements of an application [5].

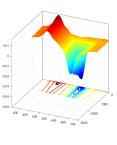

In Figure 3.1.2, the 4,8-Diester DBD dye (Ester-DBD dye, left) and the 4,8-Diacyl DBD dye (Acyl-DBD dye, right) are shown. In acetonitrile these DBD dyes absorb light at 404 nm and 429 nm and emit fluorescence at 502 nm and 558 nm, respectively, showing the distinct influence of the substituent on the photophysics [5]. An intriguing difference in the photophysics of both dyes is the sensitivity of the Acyl-DBD dye fluorescence lifetime and quantum yield towards different solvents, while the respective parameters of the Ester-DBD dye are much less affected. In the DBD dyes (see Figure 3.1.2) two electron acceptor (A) groups are attached to two electron donor groups (D) via a benzene ring (conjugated bridge). Upon photoexcitation electron density is pushed from both donor units to both acceptor parts of the molecule [5]. In order to better understand the relationship between photophysics, especially fluorescence properties, and substituents a deeper general understanding underlying the radiative as well as radiationless deactivation processes in the class of DBD dyes is needed. Here, the results of transient absorption spectroscopy are reported based on which a detailed evaluation of the electronic deactivation processes was performed.

3.1.3 Methods

Dyes were synthesized following earlier described synthesis route [5] and 0.22 mg of the solid Ester-DBD dye and 0.28 mg of the Acyl-DBD dye were dissolved in 5 mL H_2O, ACN, DCM, EtOH and Hexane to generate an optical density (OD) of about one at the pump wavelength 250 nm. For viscosity measurements, glycerol was added to the EtOH solutions. All solvents except water were purchased from Sigma–Aldrich and were of analytical grade. Water was deionized by a Milli-Q Reference Water Purification System (Merck Millipore) to 18.2 MΩ. All measurements were performed at room temperature (T = 296.5 K) if not stated otherwise. As fundamental laser source for the measurements a Ti:sapphire laser system (Spitfire Ace PA, Spectra Physics) operated at 800 nm was used. The transient absorption spectrometer (TAS, Newport) was operated with a HE-TOPAS (Light Conversion) as pump source at a pump wavelength of 250 nm (pulse energy 2.4 µJ) , unless stated otherwise, with a 1000 Hz repetition rate and 40 fs pulse width. The pump power was adjusted via a ND-filter wheel

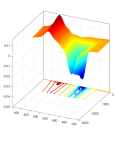

and measured by a PEPS-3-9.5 sensor (Newport). As probe beam a white light continuum (350 nm < λ_{probe} < 700 nm) generated using a CaF_2 crystal, pumped by the 800 nm fundamental (pulse energy 250 µJ) of the Ti:sapphire laser, was applied. The signal is generated as the difference in optical density (ΔOD) between the pumped and unpumped sample. The time delay was adjusted by a variable delay line between 0 to 7 ns. Instrument response function (IRF) was measured to be 90 to 150 fs depending on the probe wavelength and solvent used. Samples were measured in a quartz cuvette with 2 mm optical path length (Typ 21, Starna GmbH) and stirred by an Electronic Stirrer Model 300 (Rank Brothers Ltd.). Measurements were taken in dependence of irradiation time by measuring several 2D spectra over the course of an hour. Data deconvolution in spectral and time domain was conducted with the Parallel Factor Analysis (PARAFAC) algorithm [16] implemented in the optimization toolbox of MATLAB 2017a (MathWorks) [17] after a second-order polynomial time domain baseline-correction to compensate for dispersion. Also, to deconvolute data containing spectral shifts the PARAFAC2 algorithm [18, 19] was used. General data treatment, peak fitting and data plotting was carried out using Origin 2018 (OriginLab, Northampton, MA).

3.1.4 Results

As can be seen in Figure 3.1.3, the general shape of the time-resolved absorption spectra of both DBD dyes are similar, with the Acyl-DBD dye signals (e.g., ground state bleach (GSB) and transient absorption (TA)) being redshifted compared to the Ester-DBD dye. The GSB signal is representing the initial depletion and subsequent recovery of the ground state population. Therefore, it is found as a negative ΔOD, while the TA is representing an additional absorption by an excited state, which has not been present before the pump pulse (positive ΔOD). Initially a very broad positive signal and the superimposed (negative) GSB signal at around 420 nm (Ester-DBD dye) and 440 nm (Acyl-DBD dye) (samples 15 and 14 in Reference [5]) are dominating the spectrum. Thus, we can conclude that the broad absorption signal corresponds to the Franck–Condon-state (FC) of the excited molecule, where it is still in its ground state geometry since electronic transitions are much faster than the movement

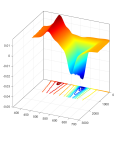

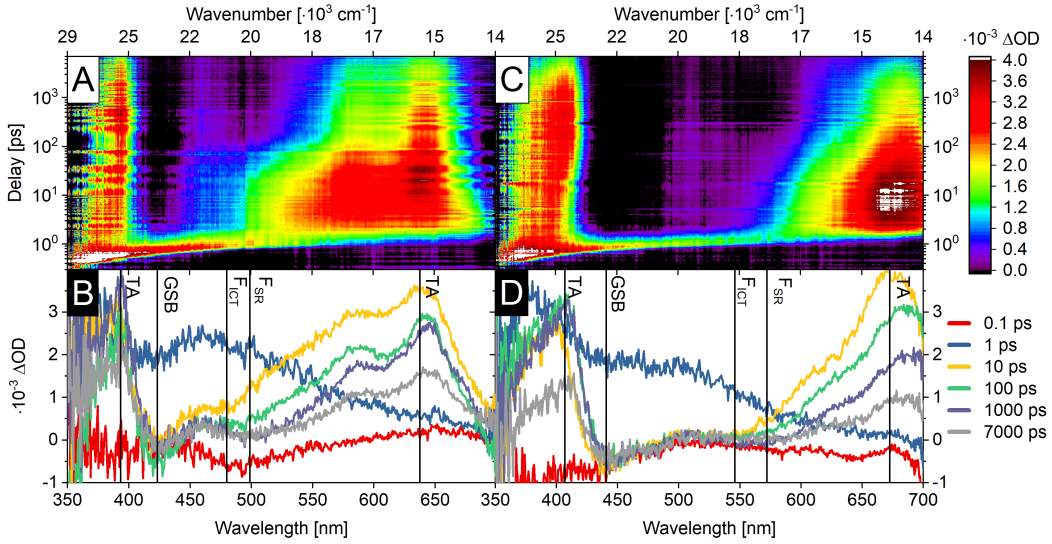

Figure 3.1.3: Transient absorption spectra of Ester-DBD (A, B) and Acyl-DBD dye (C, D) (λ_{Ex} = 250 ± 10 nm, $E_{pumppulse}$ = 2.4 µJ at 500 Hz, energy per pulse for white light generation 250 µJ, IRF = 150 fs, in EtOH). Shown are the ground state bleach (GSB) and transient absorption (TA) signals as well as fluorescence signals for the ICT-state (FICT) and solvent-relaxed state (FSR) of the DBD dyes. Solvent relaxation shift depicted as white arrow.

of nuclei. The initial broad signal is replaced within a few picoseconds by several transient absorption (TA) signals at about 390 nm, 580 nm and 640 nm for the Ester-DBD dye or at 410 nm, 630 nm and 670 nm for the Acyl-DBD dye, respectively.

As this process is very fast (faster than molecular motion), it corresponds to the rearrangement of the molecule's FC-state into the molecule's intramolecular charge transfer (ICT) state with more defined spectral properties. Former theoretical calculations have shown that the excited state of DBD dye has a quadrupole character due to a symmetrical charge separation from the dioxol-oxygens to the substituents and that its geometry is becoming planar in contrast to the bend geometry of the ground state [5].

Also visible is the fluorescence (F) of the ICT-state as a negative signal (but superimposed with the intense positive TA signal), which is shifting towards the red end of the spectrum with increasing delay time. The shift is completed within the first 300 ps after excitation (from around 480 nm to 500 nm for the Ester-DBD dye and 545 nm to 570 nm for the Acyl-DBD dye). This spectral shift in the time range of 10 ps to 300 ps can be associated to solvent relaxation processes [20]. It is due to the change

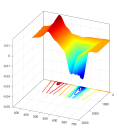

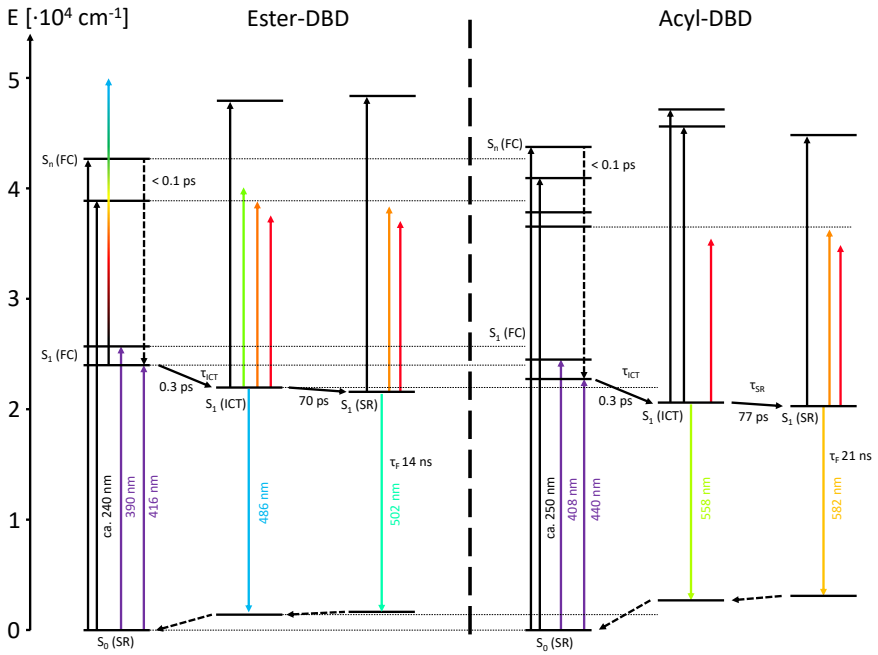

Figure 3.1.4: Proposed Jabłoński-diagrams of the Ester- (left) and the Acyl-DBD dye (right) in EtOH from TAS, UV/Vis and Fluorescence measurements; arrow colors represent color of light being emitted or absorbed.

in the DBD dye´s charge distribution upon excitation and the subsequent change of reaction field of the solvent upon the molecule. The solvent molecules in close proximity need to adjust their orientation towards the now different electric potential of the fluorophore to minimize the systems energy. Consequently, the energy gap between the excited and the ground state becomes smaller. Hence, the emission is shifted to lower energies (longer emission wavelengths) until the emission reaches the spectral position of the steady state fluorescence spectra. At this point the molecule arrived in its energy-minimized solvent relaxed (SR) state. As this spectral shift is a diffusion controlled process, its rate constant is dependent on viscosity and subsequently also on temperature. As both the ICT- and the SR-state show fluorescence, we can assume that this state is the S_1-state of the fluorophore. Comparing the GSB wavelength of the S_1 (maximum of Ester-DBD dye at 410 nm and Acyl-DBD dye at 426 nm, determined by gaussian peak fitting) with the fluorescence it can be seen that the S_1(FC)-S_1(ICT)-transition is causing already a very strong Stokes shift of 3800 ± 150 (Ester-DBD dye) and 5600 ± 800 cm^{-1} (Acyl-DBD dye) only picoseconds after excitation (see Figure 3.1.4). The transient absorption ex-

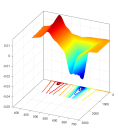

periments were additionally performed at two different pump wavelengths (λ_{pump} = 250 nm as well as 390 nm (Ester) or 420 nm (Acyl) nm, respectively) showing no distinct influence on the observed photophysics in the TA measurements. Considering that the broadband S_1(FC) signal is emerging immediately after excitation at 250 nm, we can already conclude that the higher excited electronic states S_n relax very fast into the S_1(FC)-state with transition times shorter than the IRF of the system, i.e. faster than 0.15 ps (see Figure 3.1.4). The strong polar SR-state has a long decay time and is present beyond the time scale accessible in our TAS experiments. Based on the decay of the transient fluorescence signal, a fluorescence decay time of several nanoseconds can be estimated, which is in good agreement to fluorescence decay times obtained from time-correlated single photon counting measurements. Here, fluorescence decay times of about 14 to 21 ns are found for the DBD dyes depending on the solvent (see Table 3.1.1) [5]. The limitation for the more exact determination of the fluorescence decay time from the TAS measurements is the accessible time window of maximal 8 ns, which is too short to reliably determine decay times larger than one ns.

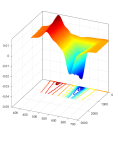

Table 3.1.1: Summary of solvent related photophysical data extracted from the analysis of the transient absorptions spectra for the Ester-DBD dye and the Acyl-DBD dye. [a]Values from SI of reference [5]. $Q(n^2)$ and $Q(\varepsilon,n^2)$ are defined in eqn. 3.9 and eqn. 3.10 (vide infra).

Solvent	$Q(n^2)$	$Q(\varepsilon,n^2)$	$\nu_{GSB,Abs}$ [cm^{-1}]	$\Delta\nu_{ICT}$ [cm^{-1}]	$\Delta\nu_{SR}$ [cm^{-1}]	τ_{ICT} [ps]	τ_{SR} [ps]	τ_F(TAS) [ns]	τ_F(TCSPC) [ns]
				Ester-DBD					
EtOH	0.339	0.595	24370 ± 90	3800 ± 150	650 ± 170	0.30 ± 0.02	87 ± 2	16 ± 9	16.4[a]
ACN	0.326	0.630	23580 ± 50	2500 ± 250	1010 ± 550	0.89 ± 0.07	30 ± 1	7.1 ± 3.8	14.4[a]
DCM	0.382	0.445	24030 ± 170	3300 ± 450	0 ± 270	0.45 ± 0.04	39 ± 3	6.2 ± 4.2	18.1[a]
Hexane	0.348	-0.003	24170 ± 160	4600 ± 2000	0	0.39 ± 0.02	–	12.2 ± 0.5	14.9
				Acyl-DBD					
EtOH	0.339	0.595	22905 ± 33	5600 ± 800	720 ± 600	0.31 ± 0.05	76 ± 3	6.6 ± 2.5	10.5[a]
ACN	0.326	0.630	23030 ± 50	4200 ± 380	595 ± 50	0.43 ± 0.04	35 ± 1	7.4 ± 1.4	21.1[a]
DCM	0.382	0.445	22260 ± 130	3420 ± 170	0 ± 110	0.39 ± 0.05	18 ± 8	20 ± 21	–
Hexane	0.348	-0.003	24190 ± 70	2410 ± 200	0	0.38 ± 0.02	–	> 7	10.9

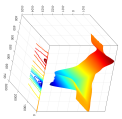

For a kinetic and spectral analysis of the different states the data sets were separated into two time regimes: i) We applied the PARAFAC deconvolution algorithm to the first 5 ps of the spectra where the S_1(FC) to S_1(ICT) transition occurs and where we have two distinct states. ii) For later times we applied the PARAFAC2 algorithm, as the PARAFAC model does not take into account the spectral shift during the solvent relaxation from S_1(ICT) to S_1(SR). As a result, both algorithms deconvoluted the experimental data into single component spectra (see Figure 3.1.5) and time traces. Those were then used for the determination of the peak positions (energy of electronic states compared to the ground state) and rate constants for relaxation or decay processes. For example, state transition times τ_{ICT}, ICT Stokes shifts $\Delta\nu_{ICT}$, SR times τ_{SR}, SR Stokes shifts $\Delta\nu_{SR}$ and fluorescence lifetimes τ_F were calculated (see Figure 3.1.4). The resulting transition times τ_{ICT} (Table 3.1.1) for both DBD dyes are similar, as both dyes have a similar chemical structure and were both measured in the same solvents, thus were exposed to identical conditions like viscosity and temperature. Fluorescence lifetime data were obtained from time-correlated single photon counting (TCSPC) experiments. The main difference between both dyes is the red shift in S_1 absorption wavelength and a larger red shift of the fluorescence for the Acyl-DBD dye. This bathochromic behavior of the absorption band is partly due to the stronger electron pull effect of the ester substituent, which is creating a more polar DBD dye molecule. This polar ground state is then better stabilized (and energetically lower) in polar solvents compared to the Acyl-DBD dye ground state. Consequently, the energy gap between the ground state and excited state becomes larger for the Ester-DBD dye. It can be seen in Figure 3.1.4 and Table 3.1.1 that the main contribution to the total Stokes shift $\Delta\nu$ can be attributed to the formation of the charge separated S_1(ICT)-state and not by the shift to the S_1(SR)-state (at least 70 % of the total $\Delta\nu$ depending on the solvent). The energy minimization of the Acyl-DBD dye is found to be stronger than for the Ester-DBD dye (higher $\Delta\nu_{ICT}$). The reduced stabilization of the Ester-DBD dye arises from the additional oxygen of the ester compared to the ketone, as this oxygen will repulsively interact with the dioxol ring oxygens and destabilize the excited state compared to the Acyl-DBD dye. The combination of the absorption redshift and the strong ICT of the Acyl-DBD dye leads to a smaller S_1(SR)-S_0

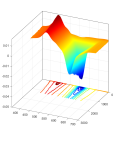

energy gap compared to the Ester-DBD dye. This smaller gap generally leads to faster non-radiative relaxation processes by internal conversion and in return to smaller fluorescence lifetimes as well as fluorescence quantum yields according to the energy gap law [21].

From the spectral separation of the excited states we can also see that the transient absorption is stronger compared to the ground state bleach signal (see Figure 3.1.5), which indicates a larger extinction coefficient of the excited state relative to the ground state. To calculate the excited state extinction coefficients ε_{TA} from the ΔOD signal of the GSB (ΔOD_{GSB}) and of the TA (ΔOD_{TA}), we can use the extinction coefficient of the ground state ε_{GS} because both signals are well separated. The linear absorption of the sample without a pump pulse (OD_{GS}) at the ground state wavelength λ_{GS} follows Lambert–Beer's-law with the light path length d and the total sample concentration c_{tot}:

$$OD_{GS}(\lambda_{GS}) = \varepsilon_{GS}(\lambda_{GS}) \cdot c_{tot} \cdot d \tag{3.1}$$

On the other hand, the optical density along the cuvette after the pump pulse ($OD_{GS/P}$) is described in the same way, but the total concentration is reduced by the amount of molecules that got excited by the pump pulse c_p:

$$OD_{GS/P}(\lambda_{GS}) = \varepsilon_{GS}(\lambda_{GS}) \cdot (c_{tot} - c_p) \cdot d \tag{3.2}$$

As ΔOD_{GSB} is defined as the difference of optical density after and before the pump pulse we get

$$\Delta OD_{GSB}(\lambda_{GS}) = OD_{GS/P}(\lambda_{GS}) - OD_{GS}(\lambda_{GS}) \tag{3.3}$$

$$\Delta OD_{GSB}(\lambda_{GS}) = -\varepsilon_{GS}(\lambda_{GS}) \cdot c_p \cdot d \tag{3.4}$$

The absorption of the molecules in the excited state c_{Ex} at the transient absorption wavelength λ_{TA} is also defined by Lambert–Beer's-law:

$$OD_{TA}(\lambda_{TA}) = \Delta OD_{TA}(\lambda_{TA}) = \varepsilon_{TA}(\lambda_{TA}) \cdot c_{Ex} \cdot d \tag{3.5}$$

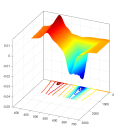

Thus the ratio between both signals gives

$$-\frac{\Delta OD_{TA}(\lambda_{TA})}{\Delta OD_{GSB}(\lambda_{GS})} = \frac{\varepsilon_{TA}(\lambda_{TA}) \cdot c_{Ex}}{\varepsilon_{GS}(\lambda_{GS}) \cdot c_{p}} \tag{3.6}$$

At long delay times (> 1 ns) we can assume that all excited molecules have either decayed back to the ground state (give no signal) or arrived in the long lived fluorescent S_1-state and that all other processes (like SR) are completed. That means that at this point in time, all molecules that are missing in the ground state are in the S_1(SR)-state, hence $c_p = c_{Ex}$ which gives the ε_{TA} of the S_1(SR)-state as

$$-\frac{\Delta OD_{TA}(\lambda_{TA})}{\Delta OD_{GSB}(\lambda_{GS})} = \frac{\varepsilon_{TA}(\lambda_{TA})}{\varepsilon_{GS}(\lambda_{GS})} \tag{3.7}$$

For the Ester-DBD dye TA at 639 nm (measured in ACN) this equals according to equation 3.7 to a 1.5 times higher extinction coefficient than at 404 nm ground state absorption (4651 M^{-1} cm^{-1}) [5] which gives an extinction coefficient ε_{TA}(639 nm) ≈ 6770 M^{-1} cm^{-1}. For the Acyl-DBD dye TA at 679 nm this equals to an ε_{TA}(679 nm) ≈ 10580 M^{-1} cm^{-1}.

3.1.5 Discussion

For the DBD dyes investigated the SR Stokes shift increases with increasing solvent polarity and approaches zero in non-polar solvents (Figure 3.1.5). As the charge distribution of the fluorophore is changing upon excitation, a more polar solvent molecule is affected stronger than a less polar solvent molecule by that change and consequently the solvent relaxation applies a stronger Onsager reaction field from this polarization [22] on the fluorophore. The connection between SR Stokes shifts $\Delta\nu_{SR}$ and solvent polarity in case of changes in the dipole moment of a molecule upon electronic excitation can be described by the Lippert–Mataga equation [23, 24]. However, the Lippert–Mataga theory is only valid for molecules that change their permanent dipole moment by excitation due to charge redistribution. But theoretical calculations (M062X/def2-TZVP) of the Aldehyde-DBD dye suggest that there are two equally likely conformers in the ground state of DBD dyes: One where the carbonyl

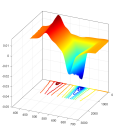

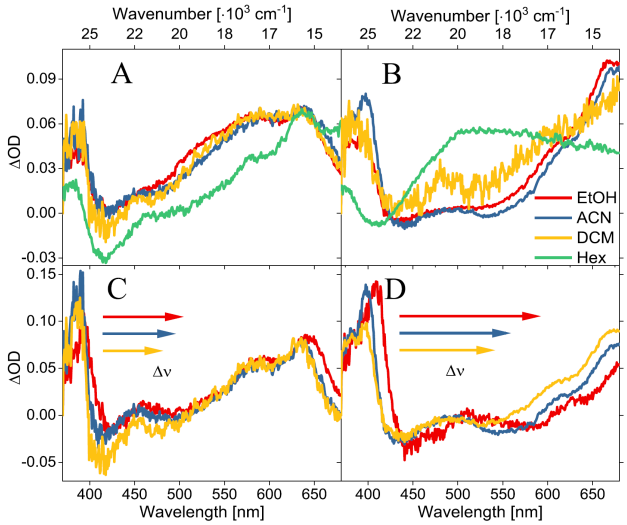

Figure 3.1.5: Spectral comparison of the PARAFAC2 deconvoluted and normalized ICT- (A, B) and SR-states (C, D) of the Ester- (A, C) and the Acyl-DBD dye (B, D) in different solvents. No SR-state observed in hexane.

oxygens of both molecule sides face in the same direction (cis-DBD dye, see Figure A.1.1 B) and thus exhibits a total dipole moment, and one where both carbonyls face in opposite directions (trans-DBD dye, see Figure 3.1.2) with no total dipole moment. The calculated energy barrier between both conformers has been determined to be 23 kJ mol^{-1} and is expected to be even higher in the excited state, as there is a partial double bond character between the aromatic system and the substituents [5]. This high-energy barrier makes it highly unlikely that an excited molecule will change its conformation within its lifetime. Hence, it will be locked in its conformation after excitation. This raises the question whether there are i) two distinctive conformation species, one with a permanent dipole moment which exhibits solvent relaxation (cis-conformer) and one without (trans-conformer) which exhibits no solvent relaxation, or ii) if both molecule conformers are exhibiting solvent relaxation through changes in their higher electric multipole moments, for example their quadrupole moments (two opposite dipoles separated by a certain distance). If the first hypothesis is true, then we would assume that two different fluorescence signals, one that is red-shifting due to solvent relaxation (cis-DBD dye, total dipole moment) and one that remains at its initial position (trans-DBD dye, no total dipole moment) would be visible. To investigate both hypothesis the Ester-DBD has been hydrolyzed under

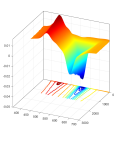

alkaline conditions to form the Carboxylate-DBD dye. To get a fully symmetric molecule without conformers, the acid was converted with TBAH into the carboxylate ion (for full synthesis route see SI A.1.2). As this Carboxylate-DBD dye (see SI A.1.2 c) is fully symmetric and should have no distinct conformers, it therefore should never have a total dipole moment in the excited state and thus should experience no solvent relaxation due to changes in dipole moment. Transient absorption measurements of the Carboxylate-DBD dye gave similar spectra and time traces compared to the Ester- and Acyl-DBD dye. Major differences are longer ICT and SR times namely 0.41 ± 0.03 ps and 195 ± 45 ps respectively, compared to 0.3 ps and about 75 ps for the Ester- and Acyl-DBD dye which can be attributed to the carboxylate being a larger (due to the tert-Butylamine-group and the resulting lower diffusion coefficient) and being a charged molecule (stronger OH-bonding to solvent molecules). Absorption and emission maxima of the S_1-state also blueshifted substantially to 355 nm and 446 nm, respectively. Most importantly the molecule exhibits solvent relaxation which should be impossible for a fully symmetrical molecule with symmetric charge separation and zero dipole moment according to the Lippert–Mataga theory. In addition, in the transient absorption spectra of the Ester- and Acyl-DBD dyes only one spectrally shifting species is found. This confirms hypothesis ii), in which the solvent molecules are reorienting towards alterations in the overall charge distribution due to a change in their higher multipole moments and the Lippert–Mataga model cannot be applied (no dipole moment change). The strongest multipole moment, when both the monopole moment (total molecule charge) and the dipole moment are zero, is the quadrupole moment (electric potential falls off with $1/r^3$). That means the spectral shift due to changes in charge distribution can be described best by changes in the molecules quadrupole moment.

Togashi et al. developed a solvent relaxation model for linear quadrupolar molecules similar to the Lippert–Mataga approach (see eq. 3.8) [25]. This model describes the relation between $\Delta\nu_{SR}$, the solvent polarizability parameters (dielectric constant ε and refractive index n) [26, 27], the ground as well as the excited state quadrupole moment strengths (Θ_{gr} and Θ_{ex}, respectively), and the solvent

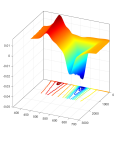

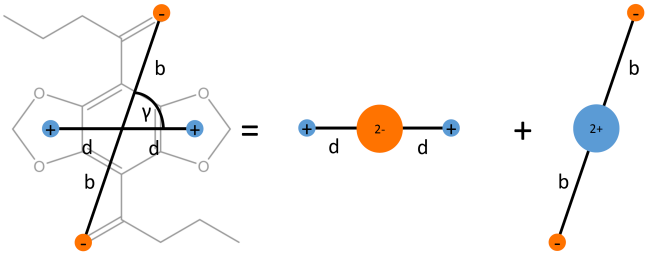

Figure 3.1.6: Visualization of a planar, parallelogramical quadrupole as a superposition of two linear quadrupoles [28].

cavity radius a, in which the fluorophore is residing in.

$$\Delta\nu_{SR} = \frac{1}{4\pi\varepsilon_0 hc}\left[-\frac{\Theta_{ex}^2 - \Theta_{gr}^2}{2a^5}Q(n^2) - \frac{\Theta_{gr}(\Theta_{ex} - \Theta_{gr})}{a^5}Q(\varepsilon, n^2)\right] \tag{3.8}$$

with

$$Q(n^2) = \frac{3(n^2-1)}{3n^2+2} \tag{3.9}$$

$$Q(\varepsilon, n^2) = \frac{3(\varepsilon-1)}{3\varepsilon+2} - \frac{3(n^2-1)}{3n^2+2} \tag{3.10}$$

For their derivation, they applied the Onsager-reaction-field model, where the change of the electric quadrupole potential (by excitation and charge redistribution) polarizes the dielectric solvent continuum around the solvent cavity. This polarization in return applies a reaction field $R^{(Q)}$ upon the quadrupole, which subsequently determines the energy of the molecules electronic state(s). To apply Togashi's model for linear quadrupoles to our molecule, we determined $R^{(Q)}$ for the planar, parallelogramical quadrupole which the DBD-dyes exhibit (see Figure 3.1.6). The reaction field of a quadrupole in a solvent cavity can be derived by solving the Laplace equation for the corresponding electric quadrupole potential V_{quad}=0 in the Onsager boundary conditions.

As can be seen in Figure 3.1.6, the solution gives the electric potential of the quadrupole V_{quad} [28] and the net reaction field $R_{net}^{(Q)}$ as the superposition of two linear quadrupole reaction fields $R_1^{(Q)}$ and $R_1^{(Q)}$ twisted by an angle $0° \leq \gamma \leq 90°$, with quadrupole lengths b and d. The reaction field for one

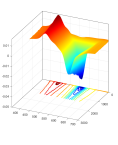

linear quadrupole $R_1^{(Q)}$ has been solved by Togashi and can be described by

$$R_1^{(Q)} = \frac{\Theta_1}{a^5}\frac{3(\varepsilon-1)}{3\varepsilon+2} = \frac{2qd^2}{a^5}\frac{3(\varepsilon-1)}{3\varepsilon+2} \tag{3.11}$$

with the elementary charge q and Θ being the scalar quadrupole strength in direction of the quadrupole axis. As the reaction field is a vector component, the total reaction field $R_{net}^{(Q)}$ can be calculated by vector addition from the single fields (superposition principle):

$$R_{net}^{(Q)} = \sqrt{R_1^{(Q)^2} + R_2^{(Q)^2} - 2R_1^{(Q)}R_2^{(Q)}\cos\gamma} \tag{3.12}$$

which gives the net reaction field as:

$$R_{net}^{(Q)} = \frac{2q\sqrt{d^4+b^4-2d^2b^2\cos\gamma}}{a^5}\frac{3(\varepsilon-1)}{3\varepsilon+2} \tag{3.13}$$

By substituting with the net quadrupole strength

$$\Theta_{net} = 2q\sqrt{d^4+b^4-2d^2b^2\cos\gamma} \tag{3.14}$$

we get (similarly to the linear quadrupole) a uniform, scalar net reaction field for the parallelogramic quadrupole:

$$R_{net}^{(Q)} = \frac{\Theta_{net}}{a^5}\frac{3(\varepsilon-1)}{3\varepsilon+2} \tag{3.15}$$

Setting either d or b to zero we get the reaction field used by Togashi, because the corresponding linear quadrupole "collapses" to zero and only the other linear quadrupole is left; while setting $\gamma = 0°$ and $b = d$ the quadrupole moment vanishes as well to zero as all charges overlap and cancel each other. With this definition, the resulting net reaction field $R_{net}^{(Q)}$ is a scalar value like the linear quadrupole and thus Togashi's derivation of the Stokes shift from the reaction field applies as well to the quadrupole of the DBD dyes. By this treatment of the reaction field we could show that Togashi's formulation

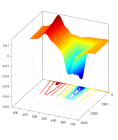

Table 3.1.2: Determined quadrupole moments Θ in Buckingham from the generalized Togashi's solvent relaxation model and the estimated charge redistribution Δq for both DBD dyes.

Dye	Θ_{ex} [B]	Θ_{gr} [B]	Δq [e]
Ester-DBD	4.6 ± 2.7	-4.1 ± 0.7	0.07 ± 0.03
Acyl-DBD	7.3 ± 4.4	-4.4 ± 0.5	0.10 ± 0.04

(eq. 3.8) can be generalized to any planar, parallelogramical quadrupole (which includes quadratic, rectangular, rhomboedric and linear quadrupoles) and thus we can apply it to the DBD dyes. Even though the Togashi-model is limited by many assumptions (spherical molecule/cavity, cavity radius does not change with solvent, quadrupole moment directions remain identical, a molecule being a pure quadrupole with point charges) it can give a good idea on the magnitude of the quadrupole moment strengths of the involved states. For a reasonable value of the cavity radius a we used a molecular dynamics simulation (Chem3D, MM2 force field parameters) of the fluorophores embedded in 30 ethanol molecules. From the optimized geometry we measured the longest distance of the molecule (methyl groups of the substituents) plus two carbon radii and took half of it as the cavity radius a. The calculations have been repeated five times with different starting geometries and we found values of a of 7.14 ± 0.08 Å and 7.58 ± 0.07 Å for the Ester- and Acyl-DBD dye, respectively. The difference in length is mostly due to the reduced bond lengths within the ester groups compared to the ketone groups, which shorten the total length of the Ester-DBD dye molecule compared to the Acyl-DBD dye.

With the given values for a, n and ε we were able to calculate the quadrupole moment strengths Θ for the Ester- and Acyl-DBD dye in their ground (Θ_{gr}) and excited states (Θ_{ex}) from the SR Stokes shifts $\Delta\nu$ (see Table 3.1.2). The quadrupole moment strength is quantified in Buckingham (B), as suggested by Peter Debye [29], and is equivalent to 1 Debye-Ångstrom (DÅ □ $3.34 \cdot 10^{-40}$ Cm^2 □ 0.208 $eÅ^2$). It can be understood as the quadrupole moment of two opposing dipoles with a dipole moment of 1 D, which are separated by 1 Å. The inversion of the sign from the ground to the excited quadrupole moment strengths corresponds to an inversion of all the charges of the quadrupoles, sim-

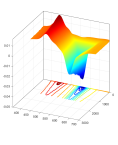

ilar to the direction inversion of a dipole moment when inverting the charges. This means, that in the ground state the partially negatively charged dioxol rings become positively charged while the substituents become negatively charged after the transition to the excited state. This is in agreement with previous theoretical calculations [5]. The absolute value of the quadrupole moment strength is corresponding to the actual strength of the quadrupole regardless of direction. For comparison, the found values are in the order of magnitude of methanol, formic acid and formamide (Θ_{xx} □ 1.9 B – 5.4 B) [30]. Under the assumption that the charges are transferred from the dioxol rings to the carbonyl oxygens (see Figure 3.1.6) and that the charge locations do not change upon excitation (only change in sign), we can calculate from the quadrupole moment strengths Θ and the charge geometry (distances b and d, angle γ) the amount of charge (Δq) that is transferred upon excitation. With equation 3.14 we can see that Δq is proportional to $\Delta\Theta$, with

$$\Delta\Theta = \Theta_{ex} - \Theta_{gr} \tag{3.16}$$

$$\Delta\Theta = 2(q_{ex} - q_{gr})\sqrt{d^4 + b^4 - 2d^2b^2\cos\gamma} \tag{3.17}$$

$$\Delta\Theta = 2\Delta q\sqrt{d^4 + b^4 - 2d^2b^2\cos\gamma} \tag{3.18}$$

The values b, d and γ are determined from the MM2 geometry optimization of the molecule in the solvent cavity, with the charges being in the center of the dioxol rings and on the carbonyl oxygens. With equation 3.18 we find values of 0.07 ± 0.03 e and 0.10 ± 0.04 e for the average charge transferred upon excitation for the Ester- and Acyl-DBD dye, respectively. Furthermore, the spectral differences in the different solvents of the PARAFAC2 deconvoluted and normalized ICT- and SR-related spectra for the Ester- and the Acyl-DBD dye are shown in Figure 3.1.5. The spectra are distinctively different for the non-polar solvent hexane. While the ICT-state is even better stabilized for the Ester-DBD dye than in any other solvent (highest $\Delta\nu_{ICT}$ of all solvents, Figure 3.1.5 A) it is the least stabilized Acyl-DBD ICT-state (lowest $\Delta\nu_{ICT}$ in all solvents, Figure 3.1.5 B). This leads us to the assumption that even slightly polar solvent molecules like DCM are strongly bound towards the molecule and stabilize the

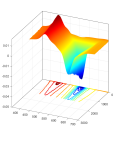

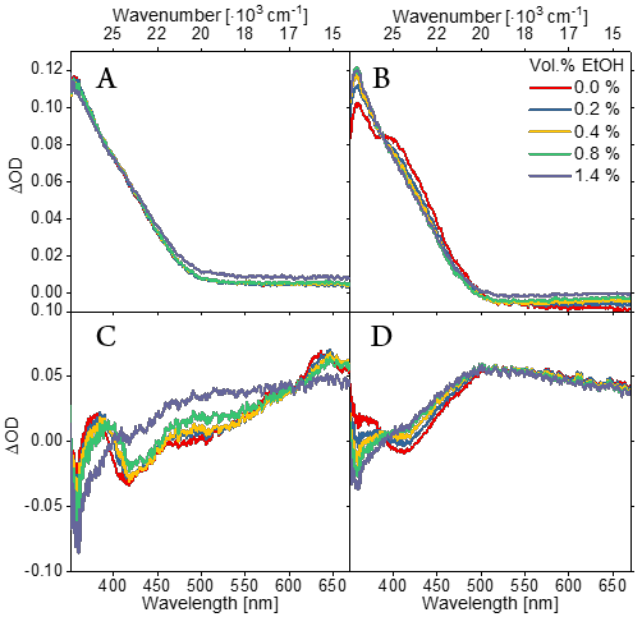

Figure 3.1.7: Spectral changes of the PARAFAC2 deconvoluted and normalized FC- (A, B) and ICT-states (C, D) of the Ester- (A, C) and the Acyl-DBD dye (B, D) in hexane with different Vol. % of EtOH added.

Acyl-DBD dyes excited state, while the Ester-DBD S_1(ICT) is destabilized by this. The strong blue shift of the GSB, i.e. ground state absorption peak, of the Acyl-DBD dye from around 410 to 430 nm further suggests that the solvent molecules are bound towards the molecule already in the ground state, while the Ester-DBD dye shows almost no change in ground state absorption. This might indicate that in the case of the Ester-DBD dye polar solvent molecules are "added" in its excited state, which subsequently relaxes the energy of this state stronger than in the Acyl-DBD dye. As these effects are also present in the aprotic solvents we can exclude a proton transfer reactions between the solvent and the DBD dye in the excited state. However, this does not exclude strong dipole and H-bonding towards solvent molecules (nor internal proton transfers).

To further investigate the binding strength of the polar solvent molecules to the DBD dyes we added minimal amounts of ethanol to the hexane solution, namely 0.2 to 1.4 Vol. %. These miniscule amounts of polar solvent should not change the bulk properties (like refractive index and dielectric constant) of the solution significantly and thus there should be no change in general solvent effects on the spectra. Instead, if there is strong binding of the polar solvent molecules towards the DBD dye

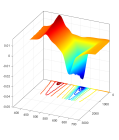

molecule, then there should be spectral changes even with minimal amounts of ethanol [20]. As can be seen in Figure 3.1.7 the spectral properties of both compounds are changing upon addition of traces of ethanol. This points to local binding of solvent molecules to the DBD molecules. As previously assumed the Ester-DBD dye seems not to be influenced by the ethanol in its ground state, as its FC-state (Figure 3.1.7 A) and GSB signal (Figure 3.1.7 C) do not change upon ethanol addition. Only the ICT-state spectra change with the addition of ethanol traces, which indicates ethanol binding in the excited state (Figure 3.1.7 C). But for that to occur within picoseconds the ethanol needs to be in close proximity to the Ester-DBD dye. It may be possible that the ethanol is not strongly bound to the Ester-DBD ground state but resides in its second coordination sphere. In case of the Acyl-DBD dye we see strong spectral changes in the FC- (Figure 3.1.7 B), GSB-, and ICT-state related signals (Figure 3.1.7 D), which supports the previous assumption of a strong ethanol binding in the Acyl-DBD ground state. This contradicting behavior of less binding of polar solvent molecules to the more polar Ester-DBD dye might be explained by its structure. The additional oxygen of the Ester-DBD dye may be interfering or blocking one of the dioxol ring oxygens, which in return blocks a coordination site for solvent molecules, while the Acyl-DBD dye is embracing a more open structure with more polar binding spots (or more space) for ethanol molecules.

In water the DBD dye photophysics is fundamentally different and no fluorescence was observed for excitation at 250 nm, but the 370 nm transient absorption of the S_1(FC)-state transforms into another broadband TA signal with an intensity maximum at around 700 nm (Figure 3.1.8). As the 700 nm absorption has no obvious peak maximum we cannot determine its exact wavelength; but a red, broadband absorption with a long lifetime of several µs [31] might be an indication for solvated electrons with an absorption maximum at 720 nm [32]. Based on this we can assume that the molecule is reaching its S_1(FC)-state from which an electron is released. This electron release reaction is slightly faster than the transition to the S_1(ICT)-state of the molecule ($4.2 \pm 0.2\ ps^{-1}$ compared to $2 - 3\ ps^{-1}$ depending on the solvent) which makes this competing deactivation process more probable than the ICT to the luminescent state. The solvated electron signal decays with 770 ± 100 ps much quicker in

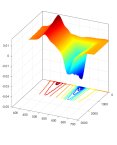

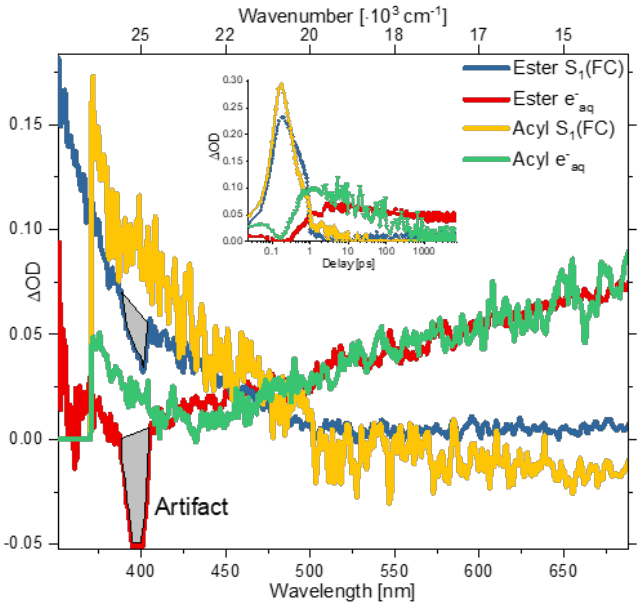

Figure 3.1.8: Transient absorption spectra of the Ester- and Acyl-DBD in water of the S_1(FC)-state (1 ps delay) and of the solvated electron (after 100 ps). Inset: Time traces of the corresponding components.

the Acyl- than in the Ester-DBD dye with a lifetime longer than 7 ns. As no other signals were detected, we were not able to resolve whether the signal decay is caused by electron-radical-recombination or other redox reactions of the solvated electron. Considering the similar structure of the main DBD dye body to phenol or salicylic acid, which is known to generate solvated electrons upon UV irradiation [33], we might assume a similar release mechanism as Gu et al. [34], where the remaining radical is stabilized by the benzene ring and the dioxol bridge opens to form a quinone type molecule. This mechanism also involves OH^- addition, which explains the existence of solvated electrons only in water and not in one of the other non-protic solvents. If there are hydroxide ions involved then pH dependent measurements should reveal a higher amount of electrons forming in high pH solutions. The lack of fluorescence emission or any other expected S_1(ICT) signals suggests that the molecule is either not reaching its S_1(ICT)-state in water after excitation at 250 nm due to molecule destruction or release of solvated electrons, while excitation in the S_1-state directly at 400 nm shows typical emission bands in steady state measurements.

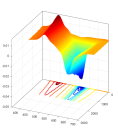

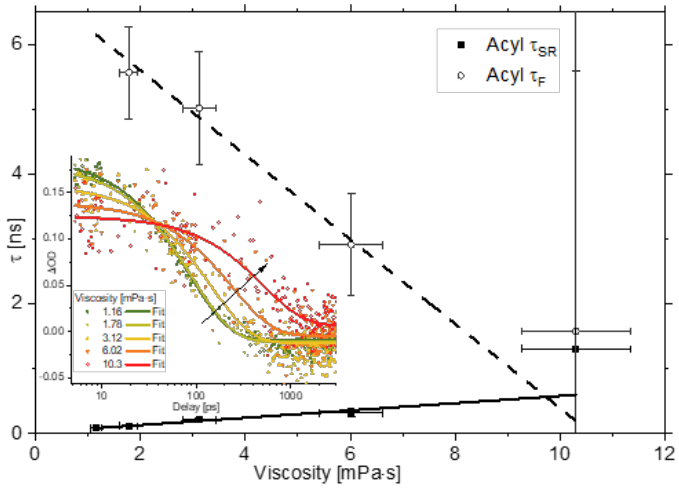

Figure 3.1.9: Viscosity dependence of the solvent relaxation time τ_{SR} and fluorescence decay time τ_F of the Acyl-DBD dye in Ethanol-Glycerol-mixtures. Inset: Monoexponential fit of data curves; see Figure A.1.2 for Ester-DBD dye.

3.1.6 Solvent Relaxation and Viscosity

While $\Delta\nu_{SR}$ is dependent on solvent polarity, τ_{SR} is dependent on medium viscosity, as with increasing viscosity the solvent molecules need a longer time to reorientate to the changed quadrupole moment of the fluorophore. As our current setup does not allow temperature dependent measurements, we used ethanol-glycerol-mixtures instead to increase solvent viscosity η. The ethanol and glycerol content has been determined by weight and the mole fractions calculated from their densities. Viscosities of these mixtures were calculated from the molar fractions of both solvents from data of Alkindi et al. [35].

As can be seen in Figure 3.1.9 the solvent relaxation time τ_{SR} for the Acyl-DBD dye is increasing linearly with viscosity from 83 ps to 512 ps (slope = 42.8 ± 5.0 ps/mPa·s), while the fluorescence lifetime decreases from 18 ns (TCSPC) to 3 ns, probably due to dynamical quenching by glycerol. At high viscosities both transition times converge into a single lifetime, where the lifetime of the fluorescent state is on the same timescale as the SR. For the Ester-DBD dye (see Figure A.1.2) the SR is increasing as well linearly with viscosity (slope = 19.7 ± 2.2 ps/mPa·s), but the fluorescence lifetime is not quenched as strong and remains very high (> 7 ns) and is not converging with the SR time.

The spectral relaxation time τ_{SR} is not equivalent to solvent molecule reorientation time, but the

Table 3.1.3: Calculated effective rotational volumes and estimated number of bound solvent molecules.

Dye	Slope τ_D/η [ps/mPa·s]	V_{eff} [Å^3]	Bound EtOH molecules in the S_1-state
Ester-DBD	209 ± 23	860 ± 210	8 ± 2
Acyl-DBD	456 ± 53	1880 ± 210	18 ± 3

measured spectral relaxation times can be used to estimate the rotational or dielectric relaxation time τ_D in ethanol [20] by eq. 3.19:

$$\tau_{SR} \approx \frac{2n^2+1}{2\varepsilon+1}\tau_D \approx 0.094\tau_D \tag{3.19}$$

These long dielectric relaxation times of 893 ps to several nanoseconds are in the magnitude of the longest rotational diffusion times of ethanol (191 ps) [20], propanol (430 ps), and butanol (668 ps) [36] and are corresponding to H-bond breaking times, as already assumed (vide supra). Due to the large strength of the H-bond it is tempting to assume that this relaxation mechanism is contributing the most to the total relaxation time and suggests to use the sticky rotational diffusion model, usually used for fluorescence anisotropy measurements. The general relation between dielectric relaxation times and viscosity has been derived by Debye [37]:

$$\tau_D \approx \frac{\eta V}{kT} \tag{3.20}$$

From this equation, we can calculate the effective volumes V of both DBD dyes (Table 3.1.3), which are molecule volumes including attached solvent molecules (volume of a sphere with a corresponding Stokes radius, similar to hydrodynamic volumes in water).

The calculated effective volumes show that the Acyl-DBD dye is having a vastly higher volume than the Ester-DBD dye in the respective excited states. However, considering the very similar ellipsoidal molecular volume of both substances, of 134 Å^3 and 123 Å^3 respectively (molecule dimensions from MD simulation, vide supra), we can further assume that many more solvent molecules are bound to

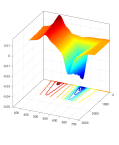

the Acyl-DBD dye as already suggested from the ethanol-hexane measurements. The difference between the calculated solvodynamic volumes and the ellipsoidal molecule volume must equal the total volume of attached solvent molecules. By subtracting the dyes molecular volumes from the solvodynamic volumes and dividing by the van-der-Waals volume of an ethanol molecule of 97 $Å^3$ (molar mass divided by density of pure ethanol), we get the approximate number of attached ethanol molecules (Table 3.1.3). For comparison the obtained solvation numbers are in similar size like rhodamine B for water 14 ± 5 and 1-butanol 8 ± 1 [38]. A similar viscosity effect is also visible for the geometry change step from the S_1(FC)- to the S_1(ICT)-state, which takes as well longer to be completed with higher viscosity, though it is not as strong as the solvent relaxation (0.32 ps to 0.48 ps in the Ester). This is probably caused by stronger resistance to move the solvent cage for a change in molecule dimension within the solvent cavity.

3.1.7 Conclusion

An Ester- and an Acyl-DBD dye were investigated by Transient Absorption Spectroscopy to improve the understanding of their photophysical properties. We found that the strong Stokes shift of these compounds is dominated by geometry changes of the molecule to form the excited intramolecular charge transfer state S_1(ICT), while solvent relaxation plays only a minor role. From spectral shifts in different solvents we were able to determine the change in the quadrupole moment of 8.8 ± 3.5 B and 11.7 ± 4.9 B for the Ester- and Acyl-DBD dye, respectively, by generalizing Togashi's theory [25] to planar, parallelogramical quadrupoles. Based on the solvent relaxation times it was deduced that the Acyl-DBD dye has more polar solvent molecules bound in its solvent sphere than the Ester-DBD dye. Measurements of ethanol/hexane-mixtures and viscosity dependent measurements showed a strong binding of protic solvents towards the molecule. Surprisingly the DBD dyes may also generate solvated electrons in water after excitation at 250 nm, while normal fluorescence is achieved by excitation into the S_1-state. Based on these results we postulate, that when the dioxol oxygens are replaced by nitrogens, to form secondary amines instead of ethers, an even higher Stokes shift should be achieved (see

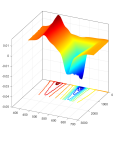

Figure A.1.3). The stronger push effect of the amine should further increase the charge separation and thus form a stronger quadrupole with stronger solvent relaxation (larger $\Delta\nu_{SR}$). On the other hand should the additional proton further stabilize the excited state molecule by an intramolecular proton transfer (IPT) from the 5-rings to the carbonyl substituents, instead of only an ICT in regular DBD dyes (larger $\Delta\nu_{ICT}$). This would introduce a new class of dyes with potentially enhanced two-photon absorption cross section (due to the stronger quadrupole moment) [39].

3.1.8 Acknowledgement

T.H. and M.U.K. are grateful to the Federal Ministry for Economic Affairs and Energy for the financial support (contract number 02E11415F).

3.1.9 Abbrevations

DBD, [1,3]dioxolo[4,5-*f*][1,3]benzodioxole; A, Acceptor; D, Donor; TAS, Transient Absorption Spectroscopy; PARAFAC, Parallel Factor Analysis; S, Singlet; GSB, Ground State Bleach; SR, Solvent Relaxation; ICT, Intramolecular Charge Transfer; IPT, Intramolecular Proton Transfer; FC, Franck–Condon; TCSPC, Time-Correlated Single Photon Counting; TBAH, Tetrabutylammonium Hydroxide; OD, Optical Density

References

[1] Hong Wen Liu et al. “Molecular engineering of two-photon fluorescent probes for bioimaging applications”. In: *Methods Appl. Fluoresc.* 5.1 (2017).

[2] Hwan Myung Kim and Bong Rae Cho. “Small-Molecule Two-Photon Probes for Bioimaging Applications”. In: *Chem. Rev.* 115.11 (2015), pp. 5014–5055.

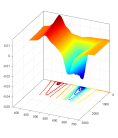

[3] Benjamin Hötzer, Igor L. Medintz, and Niko Hildebrandt. “Fluorescence in nanobiotechnology: Sophisticated fluorophores for novel applications”. In: *Small* 8.15 (2012), pp. 2297–2326.

[4] Robert Wawrzinek et al. “DBD dyes as fluorescence lifetime probes to study conformational changes in proteins”. In: *Chem. - A Eur. J.* 19.51 (2013), pp. 17349–17357.

[5] Pablo Wessig, Leonard John, and Monique Mertens. “Extending the Class of [1,3]-Dioxolo[4.5- f]benzodioxole (DBD) Fluorescent Dyes”. In: *European J. Org. Chem.* 2018.14 (2018), pp. 1674–1681.

[6] Johanna Heuveling et al. “Conformational changes of the bacterial type i ATP-binding cassette importer HisQMP2 at distinct steps of the catalytic cycle”. In: *Biochim. Biophys. Acta - Biomembr.* 1838.1 PARTB (2014), pp. 106–116.

[7] Christian Meyners et al. “A fluorescence lifetime-based binding assay for acetylpolyamine amidohydrolases from Pseudomonas aeruginosa using a [1,3]dioxolo[4,5-f][1,3]benzodioxole (DBD) ligand probe”. In: *Anal. Bioanal. Chem.* 406.20 (2014), pp. 4889–4897.

[8] Christian Meyners et al. “A Fluorescence-Lifetime-Based Binding Assay for Class IIa Histone Deacetylases”. In: *Chem. - A Eur. J.* 23.13 (2017), pp. 3107–3116.

[9] Robert Wawrzinek and Pablo Wessig. “Synthesis and spectroscopic properties of a FRET pair based on PPO and DBD dyes”. In: *Dye. Pigment.* 123.C (2015), pp. 39–43.

[10] P. Wessig et al. “Two-photon FRET pairs based on coumarin and DBD dyes”. In: *RSC Adv.* 6.40 (2016), pp. 33510–33513.

[11] Pablo Wessig et al. “FRET Pairs with Fixed Relative Orientation of Chromophores”. In: *European J. Org. Chem.* 2016.26 (2016), pp. 4476–4486.

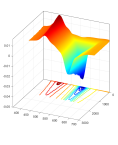

[12] Ursula Eisold et al. “Rigid Rod-Based FRET Probes for Membrane Sensing Applications”. In: *J. Phys. Chem. B* 120.37 (2016), pp. 9935–9943.

[13] Anna López de Guereñu et al. “Energy Transfer between Tm-Doped Upconverting Nanoparticles and a Small Organic Dye with Large Stokes Shift”. In: *Biosensors* 9.1 (2019), p. 9.

[14] Thomas Schwarze et al. “Highly K+-Selective Fluorescent Probes for Lifetime Sensing of K+ in Living Cells”. In: *Chem. - A Eur. J.* 23.68 (2017), p. 17156.

[15] Dörthe Büchner et al. “Detection of dsDNA with [1,3]Dioxolo[4,5-f]benzodioxol (DBD) Dyes”. In: *Chem. - A Eur. J.* 24.60 (2018), pp. 16183–16190.

[16] Rasmus Bro. “PARAFAC. Tutorial and applications”. In: *Chemom. Intell. Lab. Syst.* 38 (1997), pp. 149–171.

[17] *MATLAB and Optimization Toolbox 2018b*. Natick, Massachusetts, 2019.

[18] Rasmus Bro, Claus A. Andersson, and Henk A. L. Kiers. “PARAFAC2—Part II. Modeling chromatographic data with retention time shifts”. In: *J. Chemom.* 13.3-4 (1999), pp. 295–309.

[19] Henk A. L. Kiers, Jos M. F. ten Berge, and Rasmus Bro. “PARAFAC2—Part I. A direct fitting algorithm for the PARAFAC2 model”. In: *J. Chemom.* 13.3-4 (1999), pp. 275–294.

[20] Joseph R. Lakowicz. *Principles of fluorescence spectroscopy*. 3rd. New York: Springer, 2006, p. 954.

[21] Jonathan V. Caspar and Thomas J. Meyer. “Application of the energy gap law to nonradiative, excited-state decay”. In: *J. Phys. Chem.* 87.6 (1983), pp. 952–957.

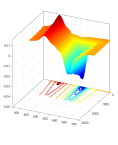

[22] Lars Onsager. “Electric Moments of Molecules in Liquids”. In: *J. Am. Chem. Soc.* 58.8 (1936), pp. 1486–1493.

[23] E. Lippert. “Spektroskopische Bestimmung des Dipolmomentes aromatischer Verbindungen im ersten angeregten Singulettzustand”. In: *Zeitschrift für Elektrochemie, Berichte der Bunsengesellschaft für Phys. Chemie* (1957).

[24] Noboru Mataga, Yozo Kaifu, and Masao Koizumi. “Solvent Effects upon Fluorescence Spectra and the Dipolemoments of Excited Molecules”. In: *Bull. Chem. Soc. Jpn.* (1956).

[25] Denisio M. Togashi et al. “Electric polarization effects on the electronic spectral shift of centrosymmetric compounds”. In: *Chem. Phys.* 300.1-3 (2004), pp. 267–275.

[26] David R. Lide. *CRC Handbook of Chemistry and Physics*. 84th. Boca Raton, FL: CRC Press, 2004, pp. 153–155.

[27] Ida Z. Kozma, Patrizia Krok, and Eberhard Riedle. “Direct measurement of the group-velocity mismatch and derivation of the refractive-index dispersion for a variety of solvents in the ultraviolet”. In: *J. Opt. Soc. Am. B* (2005).

[28] C. J. F. Böttcher et al. *Theory of Electric Polarization*. 1974.

[29] “Birefringence Gives CO’s”. In: *Chem. Eng. News Arch.* 41.16 (1963), pp. 40–43.

[30] K. Wolinski, A. J. Sadlej, and G. Karlström. “Molecular quadrupole moments”. In: *Mol. Phys.* 72.2 (1991), pp. 425–432.

[31] David C. Walker. “The Hydrated Electron”. In: (1967), pp. 79–108.

[32] G. C. Hug. “Optical Spectra of Nonmetallic Transient Species in Aqueous Solutions”. In: *Natl. Stand. Ref. Data Ser. NSRDS-NBS69* (1981).

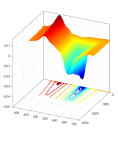

[33] Philipp-A. Primus and Michael U. Kumke. “Flash Photolysis Study of Complexes between Salicylic Acid and Lanthanide Ions in Water”. In: *J. Phys. Chem. A* 116.4 (2012), pp. 1176–1182.

[34] Jia Gu et al. “Hydrated electron (eaq−) generation from phenol/UV: Efficiency, influencing factors, and mechanism”. In: *Appl. Catal. B Environ.* 200 (2017), pp. 585–593.

[35] A S Alkindi, Y M Al-Wahaibi, and A H Muggeridge. “Physical Properties (Density, Excess Molar Volume, Viscosity, Surface Tension, and Refractive Index) of Ethanol plus Glycerol”. In: *J. Chem. Eng. Data* 53.12 (2008), pp. 2793–2796.

[36] S. K. Garg and C. P. Smyth. “Microwave absorption and molecular structure in liquids. LXVI. The dielectric relaxation of the water-dioxane system and the structure of water”. In: *J. Chem. Phys.* 43.9 (1965), pp. 2959–2965.

[37] Peter Debye. “Polar Molecules”. In: *J. Soc. Chem. Ind.* (1929).

[38] D. Noel and C. E. Meloan. “Determination of Solvation Numbers of Rhodamine B in Various Solvents by Viscosity and Gas Chromatography Measurements”. In: *Sep. Sci.* 7.2 (1972), pp. 105–114.

[39] Francesca Terenziani et al. “Charge instability in quadrupolar chromophores: Symmetry breaking and solvatochromism”. In: *J. Am. Chem. Soc.* 128.49 (2006), pp. 15742–15755.

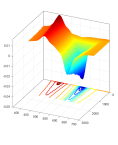

3.2 Investigating the Sulfur "Twist" on the Photophysics of DBD Dyes

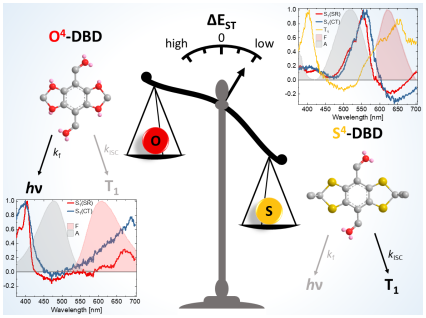

Figure 3.2.1: TOC graphic of "Investigating the Sulfur "Twist" on the Photophysics of DBD Dyes".

Haubitz, T., John, L., Freyse, D., Wessig, P., & Kumke, M. U., Investigating the Sulfur "Twist" on the Photophysics of DBD Dyes. *Journal of Physical Chemistry A*, 2020, *124*(22), 4345–4353.

Personal Contribution:

The here used samples were synthesized and provided by the "bioorganic chemistry" department of Prof. P. Wessig by L. John and D. Freyse. Fluorescence data were partly collected by L. John. All transient absorption measurements, data evaluation, tables, and graphs were done by myself. Furthermore, the large majority of the data interpretation, discussion, conclusions, and the writing of the manuscript were done by me.

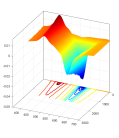

Investigating the Sulfur "Twist" on the Photophysics of DBD Dyes

Toni Haubitz, Leonard John, Daniel Freyse, Pablo Wessig, and Michael U. Kumke

University of Potsdam, Institute of Chemistry, Karl-Liebknecht-Str. 24-25, D-14476 Potsdam, Germany

3.2.1 Abstract

The so called DBD ([1,3]dioxolo[4,5-*f*][1,3]benzodioxole) dyes are a new class of fluorescent dyes, with tunable photophysical properties like absorption, fluorescence lifetime, and stokes shift. With the development of sulfur based DBDs this dye class is extended even further for possible applications in spectroscopy and microscopy. In this paper we are investigating the basic photophysical properties and their implications for future applications for S^4-DBD as well as O^4-DBD. Based on time-resolved laser fluorescence spectroscopy, transient absorption spectroscopy, and UV/Vis-spectroscopy we determined the rate constants of the radiative and non-radiative deactivation processes as well as the energy of respective electronic states involved in the electronic deactivation of S^4-DBD and of O^4-DBD. For S^4-DBD we unraveled the triplet formation with intersystem crossing quantum yields of up to 80 %. By TD-DFT calculations we estimated a triplet energy of around 13500 cm^{-1} to 14700 cm^{-1} depending on the DBD dye and solvent. Through solvent dependent measurements, we found quadrupole moments in the range of 2 B.

3.2.2 Introduction

For scientific investigations of biological and chemical systems, fluorescent organic dyes became indispensable in the last decades. They show remarkable use in microscopy, in water analytics and in many more analytical as well as diagnostic applications due to their tunable absorption and fluorescent characteristics. They can be applied in miniscule quantities and can operate in specifically tuned optical windows for maximum sensitivity in the needed wavelength range. Properties like emission

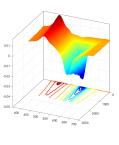

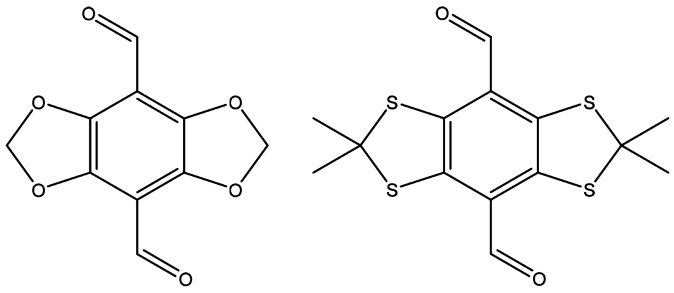

Figure 3.2.2: Structures of the two investigated ald-DBD dyes: O^4- (left) and S^4-DBD dye (right).

spectrum (often in combination with intensity measurements), luminescence lifetime, energy transfer efficiency among other photophysical parameters can be used for parallel and multidimensional analysis of sample properties like ion concentration [1], pH [2], oxygen concentration [3] or inter- as well as intra-molecular distances in (bio)macromolecules [4]. This wide field of application demands in return a high tunability in dye properties that can be adapted and optimized towards a specific application. A novel class of promising dyes emerged a few years ago, the so called DBD ([1,3]dioxolo [4,5-*f*][1,3]benzodioxole) dyes [5]. This dye class combines high absorption coefficients with good fluorescence quantum yield and, moreover, is highly flexible in absorption and fluorescence wavelength, as the spectral properties can be adjusted through substitution over a wide spectral range [6]. The substitution pattern further makes it possible to gain solubility in different solvents. Furthermore, due to their excellent spectral tunability, well adapted Förster resonance energy transfer (FRET) pairs can be realized for determining molecular distances on the nanometer scale [7, 8, 9, 10], which then can be used for example in protein conformation analysis [5, 11]. The most promising feature of the DBD dyes is their very large Stokes shift [12], due to a strong charge transfer character and high quadrupole moment [13], which is beneficial for application where the emission needs to be well separated from the excitation wavelength, like in optical microscopy applications. To extend the tunability in the optical properties of this dye class, the oxygen in the standard DBD dye (O^4-DBD) can be fully substituted by sulfur (S^4-DBD) (see Figure 3.2.2), while introducing methyl groups on each side of the DBD core. This introduces new opportunities for tuning photophysical properties [12]. Previously,

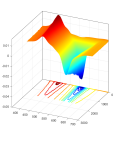

those were adjusted only by changes of the benzene substituents, which however also changes the solubility. This way the basic absorption and emission properties can be first roughly adjusted by changes to the DBD core and subsequently further fine-tuned through the substituents to reach the optimal solubility and spectral properties desired. As a drawback the introduction of sulfur leads to a decrease in luminescence lifetime and quantum yield [12], which may limit the application of S^4-DBD dyes for luminescence applications. Here, we investigate the photophysical properties of S^4-DBD and of (as reference) O^4-DBD dyes with an aldehyde side group (ald-DBD) in order to elucidate the triplet state formation in S^4-DBD dyes (as a major factor determining the reduced fluorescence efficiency and decay time), and further study the use of these dyes as triplet sensitizers.

3.2.3 Experimental Section

Dyes were synthesized following earlier described synthesis route (O^4-DBD [6], S^4-DBD [12]) and 0.25 mg were dissolved in 5 mL ACN, $CHCl_3$, $CHBr_3$, and Hexane (limited solubility, not fully dissolved). Solvents and 9,10-Diphenylanthracence were purchased from Sigma–Aldrich and are analytical grade. All measurements were performed at room temperature (T = 296.5 K) if not stated otherwise. As laser source for the transient absorption (TA) measurements a Ti:sapphire laser system (Spitfire Ace PA, Spectra Physics) operated at 800 nm was used. The transient absorption spectrometer (TAS, Newport) was operated in combination with a HE-TOPAS (Light Conversion) as pump source at a pump wavelength of 275 nm, unless stated otherwise, at a one kHz repetition rate and 40 fs pulse width. The pump power was adjusted via a ND-filter wheel and measured by a PEPS-3-9.5 sensor (Newport). An excitation at 275 nm was chosen, in order to avoid interferences from the pump light (FWHM about 6000 cm^{-1} at 40 fs pulse width), with the TA signals, which would have been the case for an excitation in the visible spectral range. As probe beam a white light continuum (350 nm < λ_{probe} < 700 nm) generated using a CaF_2 crystal, pumped by the 800 nm fundamental of the Ti:sapphire laser, was applied. The signal is generated as the difference in optical density (ΔOD) between the sample without and with previous irradiation by the pump puls. The time delay was

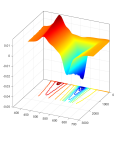

adjusted by a variable delay line between 0 ns to 7 ns. The system IRF was measured to be 90 fs to 150 fs depending on the probe wavelength and solvent used. Samples were measured in a quartz cuvette with 2 mm optical path length (Typ 21, Starna GmbH) and stirred by an Electronic Stirrer Model 300 (Rank Brothers Ltd.). Measurements were carried out in dependence of irradiation time by measuring several 2D spectra over the course of an hour, to compensate photodegradation effects with later analysis. Data deconvolution in spectral and time domain was performed using the Parallel Factor Analysis (PARAFAC) algorithm [14] implemented in the optimization toolbox of MATLAB 2018b (MathWorks) [15] after a second-order polynomial time domain baseline-correction to compensate for dispersion. Also, to deconvolve data containing spectral shifts the PARAFAC2 algorithm [16, 17] was used. General data treatment, peak fitting and data plotting was carried out using Origin 2018 (OriginLab, Northampton, MA). Emission measurements under cryogenic conditions were conducted with a helium cryostat (CKW-21, Sumitomo Heavy Industries Ltd.) in vacuum with a 10 Hz Nd:YAG Quantaray laser (Spectra-Physics) and an OPO (GWU-Lasertechnik Vertriebsges. mbH) as excitation source. An iCCD camera (iStar DH 720 18V 73) and spectrograph (Shamrock SR-303i) from Andor Technology were used for detection. Steady state measurements were performed using a Fluoromax 4 (HORIBA Scientific) in a 1 cm OS cuvette (Hellma Analytics). For excitation scans a 1 nm and 5 nm slit width in excitation and emission, respectively, were chosen. For emission scans a 5 nm and 1 nm slit width in excitation and emission were selected. Integration time per nm was 1 s. Quantum yields were determined using a Xenon/Mercury lamp and PMA-12 Photonic analyser (Absolute PL quantum yield spectrometer, HAMAMATSU Photonics).

3.2.4 Results and Discussion

As can be seen in Figure 3.2.3, the transient behavior of the oxygen ald-DBD dye is similar to the previously investigated acyl- and ester-DBD dyes [13]. There are several transient absorption signals (TA, positive signals) at around 400 nm and 690 nm for the O^4- and 550 nm for the S^4-DBD dye visible. Additionally, the ground state bleach (GSB, negative signal), as mirror image of the linear absorption

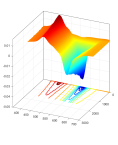

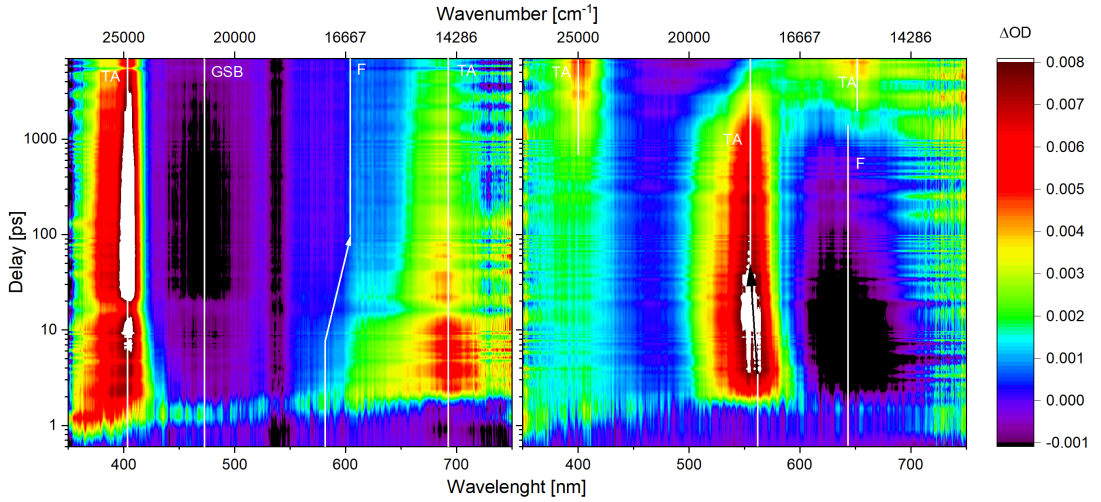

Figure 3.2.3: Comparison of the raw (not dispersion corrected) transient absorption spectra of the investigated ald-DBD dyes: O^4- (left) and S^4-DBD dye (right). (λ_{Ex} = 275 ± 10 nm, P_{pump} = 3 mW, IRF = 90-150 fs, in ACN). Visible Signals: ground state bleach (GSB), transient absorption (TA), stimulated fluorescence (F). Vertical stripe in the spectrum of the O^4-DBD dye at 545 nm is residual pump light (artifact).

spectrum, of the O^4-DBD dye is visible at around 475 nm, while the negative GSB signal of the S^4-DBD dye (at around 540 nm) is fully superimposed by the positive TA signal and thus masked by it (consequently not visible). The visible stimulated fluorescence (F, negative signal) is bathochromically shifted in comparison to the GSB signal, namely at around 605 nm for the O^4- and at 640 nm for S^4-DBD dye. For the O^4-DBD dye the negative stimulated fluorescence signal is compensated by the broad, positive transient absorption in the same spectral area to an overall signal $\Delta OD \square 0$. The stimulated fluorescence signal of the S^4-DBD dye is bathochromically shifting over several tens of picoseconds, indicating solvent relaxation as we have previously observed for the other DBD dyes. This is connected to the rearrangement of the solvent cage after excitation (charge redistribution) and thus the lowering of the energy of the fluorescent state. The simultaneous blue shift of the corresponding TA signals is indicating that those arise from S^4-DBD molecules in the same state as the fluorescing molecules (energy gap to higher states is becoming larger, thus absorption is blue shifting). As the red shifted fluorescence is found already very shortly after excitation (< 0.1 ps), we can conclude that after initial excitation by 275 nm pump light, the dyes quickly go from their initial Franck–Condon (FC)

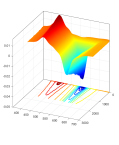

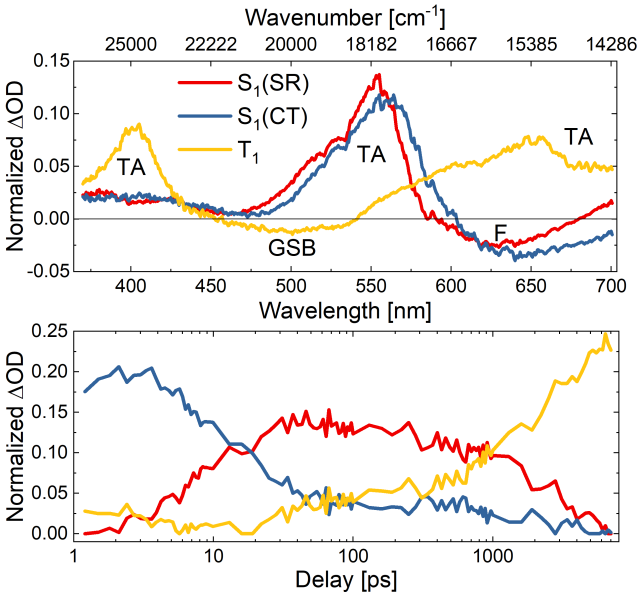

Figure 3.2.4: PARAFAC deconvoluted spectra and time traces (inlet) of the initial charge-transfer singlet state (S_1(CT)), the solvent-relaxed singlet state (S_1(SR)), and the triplet state (T_1) of the S^4-DBD dye in ACN. The GSB is compensated by TA for the S_1-state and only visible in T_1.

state into their geometry optimized charge transfer (CT) state, namely its fluorescent S_1 state. This state is characterized by a charge transfer from the DBD dyes 5-ring system to the aldehyde group [6] and the subsequent formation of a quadrupole [13]. Afterwards, over the course of tens of picoseconds, the TA is blue shifting due to solvent relaxation until it reaches its solvent relaxed (SR) S_1 state (vide supra). The changes in photophysics are dominated by the sulfur substitution and the additional methyl groups are expected to have only a minor impact on it.

An interesting spectral feature is the population of an electronic state in the S^4-DBD dyes at a longer delay time (> 1 ns) with new TA features at around 400 nm and 650 nm, respectively. This state was not observed previously with the acyl- and ester-O^4-DBD dyes nor with the here investigated ald-O^4-DBD dye. The population of this state is coupled to the deactivation of the S_1 state, which means we can assume that the fluorescence of the DBD dye might be in competition with the population of this additional state. As the formation and deactivation of molecules in this state is not yet completed within the accessible time-scale of the TAS experiment (maximum delay time 7 ns), it is not

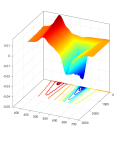

possible to determine its lifetime with sufficient precision and we can only state that it must be distinctly greater than 7 ns. The experimental spectra were deconvoluted into their single component spectra by applying the PARAFAC algorithm. With this algorithm, we model the sample data as a linear composition of three different components, i.e. populated states, namely signals arising from the non-relaxed charge transfer S_1 state (S_1(CT)), the solvent relaxed S_1 state (S_1(SR)), and the additionally populated state. The deconvoluted spectra and time traces for the S⁴-DBD dye are displayed in Figure 3.2.4 where the blue shift of the TA by SR signals is seen. While the GSB signal (at around 540 nm) is not observable in the spectrum of the S_1 state due to compensation by the TA (vide supra), it is prominent in the emerging state's spectrum. Due to the way PARAFAC is treating the data, it will combine two signal types (like GSB and TA) into one spectrum/component, if they express identical temporal behavior. This is the case, when a molecule in an excited state with a transient absorption is returning into the ground state (independent of the involved transition mechanism), as the decrease of the excited state population (decay of the TA signal) is corresponding to the refilling of the ground state population (decay of the GSB signal). This kinetic coupling indicates that an excited molecule is directly transitioning back into the ground state, either by fluorescence or by non-radiative processes. This means that the observed excited state must be an electronic state of the molecule and not a forming photoproduct (no GSB signal would be visible in this case). As the fluorescent state is most likely the S_1 state (Kasha's rule [18]) and thus the energetically lowest possible excited singlet state, the molecule has only a triplet state left to transition into. This, in combination with the long lifetime of molecules in this state ($\gg$ 7 ns) supports that the new transient absorptions might belong to the triplet state of the S⁴-DBD. An enhanced intersystem-crossing (ISC) of the S⁴-DBD dye would explain the lower fluorescence quantum yield and lifetimes, because the ISC rate (k_{ISC}) is becoming large enough to be on the scale of the fluorescence rate (k_f) to successfully compete.

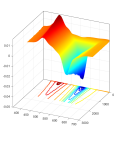

Table 3.2.1: Experimental (exp.), theoretically calculated (calc.) and estimated (est.) state energies in cm^{-1} of the two DBD dyes. S_1 energies (E_S) and peak width σ (FWHM ≈ 2.355 σ) from fitting of GSB signals of DBD dyes in $CHCl_3$. Experimental peak maxima are blue shifted compared the pure electronic state energy, due to vibronic broadening. E_T(est.) = E_S(exp.)-ΔE_{ST}(calc.) (see text for more details).

	O^4-DBD	S^4-DBD
E_S(exp.)	21150 ± 30	19770 ± 70
σ(exp.)	1150 ± 30	1500 ± 100
E_S(calc.)	21883	18798
E_T(calc.)	14694	13502
ΔE_{ST}(calc.)	7189	5296
E_T(est.)	14000	14500

3.2.5 Triplet Investigation

With a probable population of a triplet state, we also investigated the possibility of phosphorescence emission. As a first step to find the approximate energies of the DBD dyes triplet states and thus to approximate the wavelength range of the proposed phosphorescence, we conducted theoretical calculations on the DBD dyes. All calculations were done in ORCA 4.2 [19, 20] on the B3LYP [21] and ma-def2-TVZP [22, 23] (with auxiliary basis sets def2-TZVP/C [24] and def2/J [25]) level via TD-DFT in gas phase.

The calculations show good agreement of the S_1 absorption energy (E_S(calc.)) with the absorption maximum of the DBD dyes (E_S(exp.), less than 1000 cm^{-1} or 5 % for the S_1 state, see Table 3.2.1) and the values are well within the width of the peak. As we did not calculate shifts due to solvent relaxation, we assume that the energy loss through SR is similar in the singlet and triplet state and we could thus subtract the calculated energy difference between singlet and triplet (ΔE_{ST}(calc.)) from the S_1 absorption energy to estimate the corresponding triplet energy. This way we expected the phosphorescence emission to be at around 700 ± 50 nm for the investigated DBD dyes.

$$\Delta E_{ST}(\text{calc.}) = E_S(\text{calc.}) - E_T(\text{calc.}) \tag{3.21}$$

$$\Delta E_T(\text{est.}) = E_S(\text{exp.}) - \Delta E_{ST}(\text{calc.}) \tag{3.22}$$

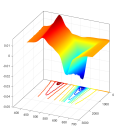

To reduce triplet quenching by oxygen and to reduce thermally induced non-radiative relaxation of the triplet state, we cooled the sample to 4 K (excitation at absorption maximum in the visible range). Although sensitivity settings of the instrumental set up were tuned to the maximum, we were not able to detect any phosphorescence signals with either DBD dye in the detectable emission range (550 nm up to 900 nm). Apparently even at 4 K, there are still non-radiative processes present which deactivate the triplet state of the molecule much faster than phosphorescence, most likely the ISC back to the S_0 state. Furthermore, we tried to prove the presence of a triplet state via triplet-triplet-annihilation up-conversion (TTA-UC) [12, 26]. Briefly, in this experiment, the DBD dyes are used as a triplet sensitizer for an upconversion activator, where in the first step the DBD dyes are excited to their S_1 state and then undergo the postulated ISC to their T_1 state. In the next step, the triplet energy is transferred from the sensitizer to an activator molecule via the Dexter-mechanism (triplet-triplet energy transfer, TTET). When sufficient activator molecules are in their triplet state, two triplet activator molecules can undergo TTA (Dexter-mechanism) to bring one of the molecules into its singlet ground state S_0 and the other into its first singlet excited state S_1, from which it can subsequently emit fluorescence. This way it is possible to transform two low energy photons (Sensitizer S_1 energy) into one higher energy photon (Activator S_1 energy). For an effective overall TTA-UC process, both triplet energies have to match and the lifetimes of the triplet state must be long enough for collisions to take place, due to the necessary small molecule distances for the Dexter-mechanism to take place (orbital overlap necessary). We used 9,10-diphenylanthracene (DPA), as it is an effective activator [26] and its triplet energy (14290 cm^{-1}) [27] should match the DBD dyes triplet energy (see Table 3.2.1), while its absorption and emission spectra only minimally overlap with the S^4-DBD dye spectra. As its own ISC quantum yield is rather low (Φ_{ISC} = 0.03) and its fluorescence quantum yield is high (Φ_F = 0.92) [27] the activators triplet state is preferentially populated via sensitization from a triplet sensitizer and we expect a high TTA-UC quantum yield Φ_{UC} from the TTA-UC induced fluorescence of DPA (445 nm) [26].

In Figure 3.2.5 the results of the DBD-DPA upconversion experiments are presented. An interesting phenomenon in the excitation spectrum of the S^4-DBD dye at λ_{em} = 640 nm (green curve) is that the

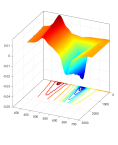

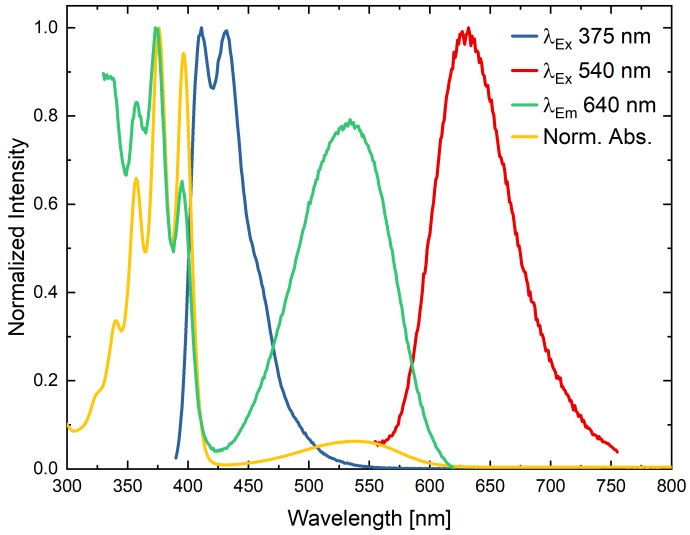

Figure 3.2.5: Normalized steady-state excitation, emission, and absorption spectra of the S⁴-DBD dye (0.29 μM) and DPA (2 μM) for the proposed TTA-UC system in DCM.

DBD fluorescence is observable when exciting the DPA directly into its S_1 state, visible as the vibronic band structure on the blue end of the spectrum, which resembles the DPA absorption spectrum. This can be attributed to a weak energy back-transfer from a DPA molecule in its S_1 state to a DBD molecule in the ground state, most likely a dipole-dipole FRET mechanism, as the DPA emission and the DBD absorption have a small spectral overlap around 500 nm. We calculated the overlap integral J for this FRET pair to be $3.29 \cdot 10^{13}$ nm^6/mol and thus the FRET radius R_0 to be 2.74 nm from the normalized DPA emission spectrum and the absorption spectrum of the DBD in M^{-1} cm^{-1}, for a refractive index n of 1.424 (DCM) [28] and a κ^2 of 2/3 for an isotropic arrangement of molecules in solution. The FRET efficiency E_{FRET} must be far lower than the fluorescence quantum yield of DPA $\Phi_{F\text{-}DPA}$, as we do not see any DBD emission at 640 nm when we excite the DPA directly at 375 nm (bottom spectrum, blue curve). QY measurements confirm the steady-state results, as the FRET efficiency is lower than 1 %. However, when going to a 1000-fold higher concentration (0.29 mM DBD and 2 mM DPA) a strong DBD emission was detected when exciting at 375 nm and a FRET efficiency of 20 % was found, due to the 10-fold smaller average donor-acceptor distance at this high concentration. As can be seen, no upconversion process was observed and thus it remains inconclusive if the observed state is actually

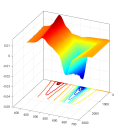

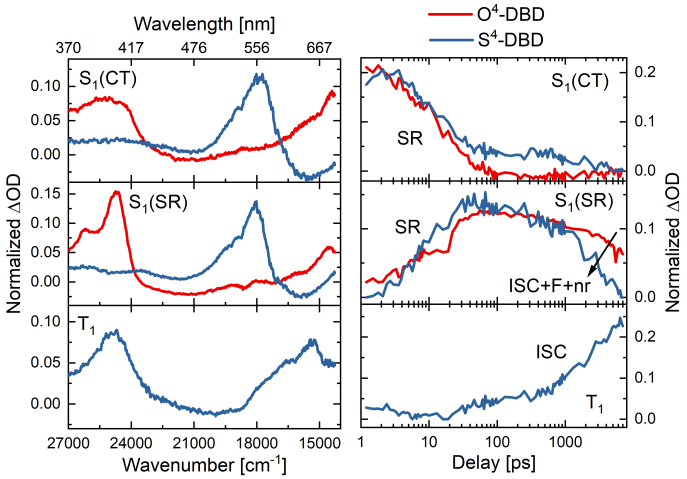

Figure 3.2.6: Comparison of the deconvoluted and normalized TA spectra (left) and time-traces (right) from PARAFAC analysis of the three involved excited states (top: S_1(CT), middle: S_1(SR), bottom: T_1) of the two DBD dyes O^4 (red) and S^4 (blue) in ACN at λ_{Ex} = 275 nm. T_1 state of O^4-DBD is not observed, as k_{ISC} is low and T_1 is populated outside of the observable timescale of the TAS-setup.

the triplet state of the molecule. Even though no direct evidence was found, the triplet hypothesis is the strongest explanation for the observed TAS signal.

3.2.6 Comparison of Kinetics

From the collected TAS data and the deconvoluted time-traces it is possible to determine the rate constants for the deactivation processes (solvent relaxation, fluorescence, and ISC) from (de)population of the three involved states, namely the S_1(CT), S_1(SR) and T_1 state (see Figure 3.2.6). As the depopulation of S_1(CT) and population of S_1(SR) are temporally coupled via the solvent relaxation rate k_{SR}, it can be directly determined from global fitting an exponential curve to the respective decay and rise kinetics simultaneously. On the other hand, the depopulation of S_1(SR) and the population of the proposed T_1 are only indirectly coupled, as the rate determined from the depopulation of S_1(SR) is the sum of several different deactivation routes (k_f, k_{ISC} and non-radiative processes with rate k_{nr}) while the population rate of the T_1 state can be directly related to k_{ISC}. Via the measured fluorescence lifetime τ_F, the previously measured Φ_F, and the measured k_{ISC} we can determine all involved rates k

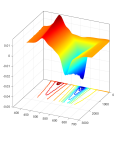

and the ISC quantum yield Φ_{ISC} via the following equations:

$$\tau_F = \frac{1}{k_f + k_{ISC} + k_{nr}} \tag{3.23}$$

$$\Phi_F = \frac{k_f}{k_f + k_{ISC} + k_{nr}} = k_f \cdot \tau_F \tag{3.24}$$

$$k_f = \frac{\Phi_F}{\tau_F} \tag{3.25}$$

$$\Phi_{ISC} = \frac{k_{ISC}}{k_f + k_{ISC} + k_{nr}} = k_{ISC} \cdot \tau_F \tag{3.26}$$

$$k_{nr} = \frac{1}{\tau_F} - k_f - k_{ISC} \tag{3.27}$$

The kinetic results are summarized in Table 3.2.2 and we can see that the fluorescence rate k_f is identical for both DBD dyes with around 0.03 ns^{-1} and that the non-radiative deactivation processes, like the ISC, mainly dominate the final fluorescence lifetime τ_F. While the ISC rate for the O^4-DBD dye was not accessible due to the slow filling of its triplet state, we can see from the S^4-DBD dyes that the ISC rate is decreasing with increasing solvent polarity and thus the fluorescence lifetime and quantum yield are increasing. This could be an indication that the singlet and triplet energies shift differently with alteration of solvent polarity, which would lead to a decrease in singlet-triplet overlap (larger energy gap) and subsequently would result in a smaller ISC rate. The general increase in k_{ISC} with sulfur substitution might be caused by the heavy-atom-effect of the four sulfur atoms in comparison to the oxygen atoms [29]. A heavier atom thus causes stronger spin-orbit coupling which in return causes a higher ISC rate. This effect might be cumulative with increasing number of sulfur atoms (see Table 3.2.2) and that hypothetical DBD dyes S^1-O^3, S^2-O^2, and S^3-O^1 would have ISC rates in-between the ones investigated. Remarkably, the ISC quantum yield reaches about 80 % in the S4-DBD dye.

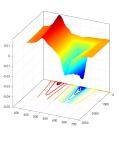

Table 3.2.2: Summary of kinetic data of the two investigated DBD dyes O^4 and S^4 in the four investigated solvents Hexane, $CHCl_3$, $CHBr_3$, and ACN. [a]ref. [6], [b]ref. [12], [c]value for DCM used in calculation, [d]not determined

Solvent	k_{SR} [ns^{-1}]	k_{ISC} [ns^{-1}]	k_f [ns^{-1}]	k_{nr} [ns^{-1}]	Φ_F	Φ_{ISC}	τ_F(TAS) [ns]
				O^4-DBD			
Hexane	–	–	[d]	[d]	[d]	–	3.3 ± 0.9
$CHCl_3$	34 ± 2	–	0.031 ± 0.004	0.031 ± 0.006	0.49 [a,c]	–	16 ± 1
$CHBr_3$	10.2 ± 0.5	–	[d]	[d]	[d]	–	22 ± 3
ACN	64 ± 4	–	0.035 ± 0.007	0.07 ± 0.02	0.32 [a]	–	9.2 ± 0.9
				S^4-DBD			
Hexane	-	0.42 ± 0.04	[d]	[d]	[d]	0.9 ± 0.8	2 ± 2
$CHCl_3$	59 ± 2	0.31 ± 0.01	0.04 ± 0.02	0.05 ± 0.03	0.10 [b,c]	0.78 ± 0.04	2.51 ± 0.05
$CHBr_3$	–	0.36 ± 0.03	[d]	[d]	[d]	0.80 ± 0.07	2.2 ± 0.9
ACN	38 ± 3	0.33 ± 0.04	0.03 ± 0.02	0.02 ± 0.05	0.09 [b]	0.9 ± 0.2	2.6 ± 0.2

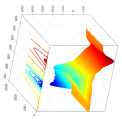

3.2.7 Comparison of TA Spectra

When comparing the spectra of the three involved states (see Figure 3.2.6) it is obvious that the substitution by sulfur in the DBD dyes causes a strong redshift in the spectra (transient absorptions, GSB, and fluorescence, respectively). This redshift can be explained by the stronger electronic push-effect of the thioether of the S^4- in comparison to the ether of the O^4-DBD dye, mainly due to the lower electronegativity of sulfur in comparison to oxygen (weaker -I-effect) and slightly stronger +M-effect. In combination, this stronger push-pull-character of the sulfur substituted DBD compound then leads to smaller energy of the excited state.

All peaks are, similar to the peaks in the linear absorption spectrum, asymmetrically broadened towards the blue end of the spectrum. This originates from the fact that the molecules vibrations couple to the electronic states of the molecule. The distance of the vibronic sublevels are thus corresponding to a vibration of the excited molecule (for absorption spectra), but as the molecule is exhibiting a whole spectrum of vibrations (C=O, aromatic, C-H, C-O, ...) all the vibronic sublevels superimpose and are not resolvable at room temperature, like for example in anthracene, leading to broad and asymmetric peaks. That is why energy determination for absorption peaks is done by fitting one or two Gaussian peaks to the experimental absorption spectrum, rising the problem of not knowing the exact lowest vibronic state energy. Same phenomenon is true for the fluorescence peaks (here, the vibronic structure would resemble the vibrations of the ground state).

With all the collected spectroscopic data, we are able to develop a detailed Jabłoński-diagram for both investigated DBD dyes (see Figure 3.2.7). The energy of nearly all involved states is lowering in energy by sulfur substitution. While the linear absorption and fluorescence are shifting already moderately due to sulfur substitution (about 2000 cm^{-1}) the TA peaks are shifting much stronger up to the point, at which the TA completely overlaps with the GSB (shift of about 7000 cm^{-1}!). We investigated the different DBD dyes in four different solvents (hexane, $CHCl_3$, $CHBr_3$, and ACN) and, as expected from results previously obtained for the acyl- and ester-DBD dyes [13], we observed a distinct solvent dependency in the spectra. Especially interesting is hereby the spectral shift due to solvent re-

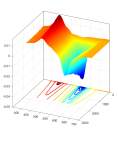

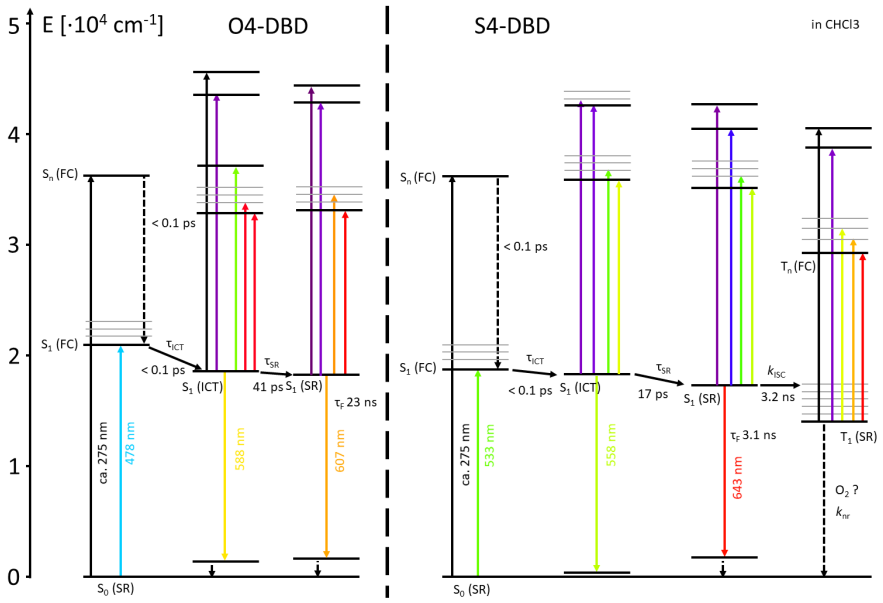

Figure 3.2.7: Jabłoński-diagram of the O⁴- and S⁴-DBD dye in chloroform. Color of the transition corresponds to color of absorbed/emitted photon.

laxation $\Delta\nu_{SR}$, as this shift corresponds to the electric moment of the molecule, where a more polar molecule is exhibiting a stronger $\Delta\nu_{SR}$ in polar solvents. As the symmetric O⁴- and S⁴-DBD dye have no permanent dipole moment, the next strongest multipole moment to describe the molecules charge distribution is the quadrupole moment (QM) and its effect on the surrounding dielectric. As shown previously [13], it is possible to apply Togashi's model of solvent relaxation for linear quarupoles [30] as well to parallelogramical quadrupoles like the DBD dyes [13]. DBD dyes form parallelogramical quadrupoles upon excitation, as a charge/electron of the two 5-rings (two positive poles) is transferred evenly onto the aldehyde groups (two negative poles), forming a molecular quadrupole in the electronically excited state. In this model (see eq. 3.28) the shift due to solvent relaxation $\Delta\nu_{SR}$ is dependent on the quadrupole strength of the molecule in the ground state Θ_{gr} and excited state Θ_{ex}, the solvents refractive index n and dielectric constant ε [28], and the radius of the solvent cavity a that the molecule is displacing. Furthermore, the scalar quadrupole strength Θ of a parallelogramical quadrupole is defined in this model as the superposition between two linear quadrupoles with the charge q, the

Table 3.2.3: Determined quadrupole moments Θ of the ground (gr) and excited (ex) state of the two investigated DBD dyes in units of Buckingham (1 B = $3.34 \cdot 10^{-40}$ Cm^2 = 1 eÅ^2 = 1 DÅ).

Dye	Θ_{ex} [B]	Θ_{gr} [B]	Δq [e]
O^4	-1.3 ± 0.3	0.82 ± 0.07	0.021 ± 0.003
S^4	-2.1 ± 2.8	2.4 ± 0.6	0.04 ± 0.03

quadrupole lengths b and d, and the angle between the opposite charges γ (see eq. 3.31).

$$\Delta\nu_{SR} = \frac{1}{4\pi\varepsilon_0 hc}\left[-\frac{\Theta_{ex}^2 - \Theta_{gr}^2}{2a^5}Q(n^2) - \frac{\Theta_{gr}(\Theta_{ex} - \Theta_{gr})}{a^5}Q(\varepsilon, n^2)\right] \tag{3.28}$$

with

$$Q(n^2) = \frac{3(n^2-1)}{3n^2+2} \tag{3.29}$$

$$Q(\varepsilon, n^2) = \frac{3(\varepsilon-1)}{3\varepsilon+2} - \frac{3(n^2-1)}{3n^2+2} \tag{3.30}$$

$$\Theta_{net} = 2q\sqrt{d^4 + b^4 - 2d^2b^2\cos\gamma} \tag{3.31}$$

To determine the cavity radius a, we used a molecular mechanics calculation that is implemented in Chem3D with the MM2 force field, where we embedded the two DBD dyes investigated in this study in 30 $CHCl_3$ molecules and ran geometry optimizations from five different starting configurations. The final radius is then calculated from the respective DBD dyes diameter (furthest nuclei to nuclei) plus two van-der-Waals-radii of carbon or hydrogen and then dividing the whole diameter by two to get the cavity radius. The found mean values are 5.32 ± 0.01 Å and 6.5 ± 0.1 Å for the O^4- and S^4-DBD dye, respectively. The growth of the cavity radius is expected, due to the larger sulfur atoms in comparison to oxygen and the additional methyl groups of the sulfur DBD dyes, causing a larger solvent displacement.

The determined quadrupole moments can be found in Table 3.2.3. The absolute value is then corresponding to the quadrupole moment strength, meaning further charge separation or more charge being separated. While the sign for each molecule is somewhat arbitrary (depending on how the charge

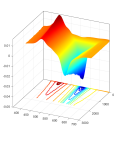

position is defined in space/coordinate system), a flip in the sign of the QM (like between ground and excited state) means an inversion of charges and thus an inversion of the QM orientation. This is similar to a direction change of a dipole moment when all charges are inverted. As can be seen from the data, the ald-DBD dyes only exhibit a small QM (as could be expected from the small SR shifts), but similar to the previously investigated DBD dyes we observed a complete inversion of the quadrupole which means a strong charge transfer from the 5-rings to the aldehyde. Comparing the two DBD dyes with one another, we can see that the sulfur DBD exhibits a stronger quadrupole moment, as could be expected from the larger charge separation (sulfur larger than oxygen) and from the stronger push effect of sulfur. As previously shown, we can derive an additional parameter from the change in quadrupole momenta: The average transferred charge Δq upon excitation. Via the previously defined scalar, parallelogramical quadrupole moment (see eq. 3.31) and the assumption that the quadrupole lengths b and d are identical in the ground and excited state (no change in molecule geometry), we can estimate the transferred charge Δq from the change in quadrupole moment $\Delta\Theta$ (= $|\Theta_{ex}\text{-}\Theta_{gr}|$).

$$\Delta\Theta = 2\Delta q\sqrt{d^4 + b^4 - 2d^2b^2\cos\gamma} \tag{3.32}$$

Quadrupole lengths b and d, and the angle γ were taken from the previously done molecular mechanics simulation, with the center of the dioxol-rings as one linear quadrupole and the aldehyde oxygens as the other linear quadrupole (see ref. [13]). As can be seen in Table 3.2.3 the transferred charge upon excitation in the ald-O^4-DBD dye is about 0.02 e, which is less than half of the amount of the ester- and acyl-O^4-DBD dyes with 0.07 ± 0.03 and 0.10 ± 0.04, respectively [13]. This behavior can be explained by the fact, that a negative charge that is transferred onto the substituents oxygen is better stabilized on a ketone or ester than on an aldehyde group, due the additional side chain. However, due to the large error of Δq for the S^4-DBD dye we can draw no conclusion on the magnitude of the larger push-pull-effect due to sulfur substitution.

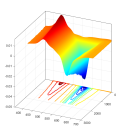

Table 3.2.4: Spectral properties of the investigated DBD dyes. Data for GSB are the value with lowest error of the three possible states. Wavenumber, peak width σ (FWHM $\approx 2.355\,\sigma$) and extinction coefficient ε of the transient absorption at highest intensity in the solvent relaxed S_1- (TA-S1) and T_1-state (TA-T1). [a] low solubility/not determinable, [b] GSB superimposed by TA.

Solvent	$\nu_{GSB} \pm \sigma$ [cm^{-1}]	$\Delta\nu_{ICT}$ [cm^{-1}]	$\Delta\nu_{SR}$ [cm^{-1}]	$\nu_{TA\text{-}S1} \pm \sigma$ [cm^{-1}]	$\varepsilon_{TA\text{-}S1}$ [$M^{-1}\,cm^{-1}$]	$\nu_{TA\text{-}T1} \pm \sigma$ [cm^{-1}]	$\varepsilon_{TA\text{-}T1}$ [$M^{-1}\,cm^{-1}$]
				O^4-DBD			
Hexane	[a]	[a]	0	25700 ± 4400	[a]	–	–
$CHCl_3$	21150 ± 1145	3810 ± 50	28 ± 159	24710 ± 410	22400	–	–
$CHBr_3$	21130 ± 1150	4170 ± 80	-4 ± 10	24147 ± 440	[a]	–	–
ACN	21340 ± 1400	4310 ± 40	118 ± 81	24678 ± 435	19700	–	–
				S^4-DBD			
Hexane	19850 ± 855	3110 ± 30	0	19160 ± 730	[a]	25310 ± 990	[a]
$CHCl_3$	19770 ± 1450	4360 ± 80	327 ± 23	17850 ± 410	27400	24680 ± 850	27900
$CHBr_3$	[b]	[b]	0	17625 ± 410	[a]	24000 ± 2000	[a]
ACN	19950 ± 1050	4510 ± 60	250 ± 22	17990 ± 400	21400	24890 ± 920	39300

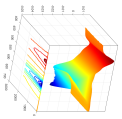

As we have shown before [13], we can also find the extinction coefficient of the transient absorption ε_{TA} from the ratio of ΔOD of the TA and GSB signal and the ground state extinction coefficient ε_{GS} at the corresponding wavelength:

$$-\frac{\Delta OD_{TA}(\lambda_{TA})}{\Delta OD_{GSB}(\lambda_{GS})} = \frac{\varepsilon_{TA}(\lambda_{TA})}{\varepsilon_{GS}(\lambda_{GS})} \tag{3.33}$$

This equation is applicable when one can be assured, that all the molecules that are missing in the ground state (ΔOD_{GSB} corresponds to the concentration of those molecules) are residing in the state from which the TA is originating from ($c_{GSB} = c_{TA}$). This condition is fulfilled at long decay times (beyond 1 ns), as by then all other relevant non-radiative deactivation pathways can be assumed to be completed and the molecules arrived either in their S_1 or T_1 state. As PARAFAC gives the pure spectra at these times, the TA extinction coefficients can then be directly calculated from the known linear extinction coefficients of the O^4- and S^4-DBD dyes in ACN and DCM (2950, 3360 and 5091, 5646 M^{-1} cm^{-1}, respectively) [6, 12] and the found peak intensities for GSB and TA. As could be expected from the raw spectra, the extinction coefficients for the transient absorptions are 7-fold greater than the ground state absorption coefficient in the visible region and 3-fold greater than in the UV region. This means that the S_1-S_n wavefunctions and the T_1-T_n wavefunctions overlap much better than the corresponding S_0-S_1 and S_0-S_n wavefunctions, showing that after the initial excitation and charge transfer in the S_1 and T_1 state the charge distribution does not change much when exciting into higher states like S_n and T_n. A summary of the spectral properties of the investigated DBD dyes is given in Table 3.2.4.

3.2.8 Conclusion and Outlook

We could conclusively show, that the sulfur DBD's low fluorescence lifetime and quantum yield are originating from a stronger spin-orbit coupling and thus from a faster ISC which is then in competition with radiative deactivation process. The high ISC quantum yield of 80 % for the S4-DBD makes it a good triplet generator. This opens applications as a sensitizer, for example for singlet oxygen genera-

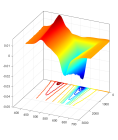

tion. Due to the expected tunability of the singlet and triplet energies by substituents of the DBD dye, the sensitizer would also be adjustable towards the energies required for desired activator molecules. To increase the total TTA-UC efficiency of the S^4-DBD/DPA-pair, one could covalently couple a stack of molecules in a DBD-DPA-DPA-DBD configuration to preorientate the molecules in terms of their transition dipole moments and eliminate the diffusion steps for the TTET and TTA. From these results we can further postulate that a theoretical selenium based DBD dye, for example a Se^4-DBD dye with all sulfur atoms replaced by selenium, might have an even stronger heavy-atom-effect with a higher ISC rate leading to a very high Φ_{ISC} of 90 % or more. Sulfur substitution also leads to a stronger push-pull-effect in the DBD dye molecule, which leads to a smaller singlet and triplet energy. This smaller energy corresponds to red shifts of all spectra (absorption, fluorescence, and transient absorption) and can be used as further tuning tool, if the filling of the DBD triplet state is desired, e.g. for singlet oxygen generation (vide supra). Solvent dependent measurement showed only minor dependency of fluorescence on solvent polarity, represented by quadrupole moments on the order of 1 to 2 B, with the sulfur DBD having a stronger quadrupole moment.

3.2.9 Acknowledgement

T.H. and M.U.K. are grateful to the Federal Ministry for Economic Affairs and Energy for the financial support (contract number 02E11415F). We would also like to thank Sean M. McGee for his support on the 4 K emission measurements.

3.2.10 Abbreviations

DBD, [1,3]dioxolo[4,5-*f*][1,3]benzodioxole; A, Acceptor; D, Donor; TAS, Transient Absorption Spectroscopy; PARAFAC, Parallel Factor Analysis; S, Singlet; T, Triplet; GSB, Ground State Bleach; SR, Solvent Relaxation; ICT, Intramolecular Charge Transfer; ISC, Intersystem crossing; FC, Franck–Condon; TCSPC, Time-Correlated Single Photon Counting; OD, Optical Density; DPA, 9,10-Diphenylanthracene; TTA, triplet-triplet annihilation; TTET, triplet-triplet energy transfer; UC, up-

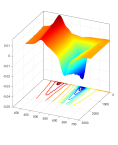

conversion; QM, quadrupole moment

References

[1] Rajesh Kumar et al. “Revisiting Fluorescent Calixarenes: From Molecular Sensors to Smart Materials”. In: *Chem. Rev.* 119.16 (2019), pp. 9657–9721.

[2] Junyan Han and Kevin Burgess. “Fluorescent indicators for intracellular pH”. In: *Chem. Rev.* 110.5 (2010), pp. 2709–2728.

[3] Dörte Steinbrück et al. “An Innovative LASER-Based Sensing Platform for Real-Time Optical Monitoring of Oxygen”. In: *Jt. Int. IMEKO TC1+ TC7+ TC13 Symp.* 2011.

[4] Atsushi Miyawaki. “Development of Probes for Cellular Functions Using Fluorescent Proteins and Fluorescence Resonance Energy Transfer”. In: *Annu. Rev. Biochem.* 80.1 (2011), pp. 357–373.

[5] Robert Wawrzinek et al. “DBD dyes as fluorescence lifetime probes to study conformational changes in proteins”. In: *Chem. - A Eur. J.* 19.51 (2013), pp. 17349–17357.

[6] Pablo Wessig, Leonard John, and Monique Mertens. “Extending the Class of [1,3]-Dioxolo[4.5- f]benzodioxole (DBD) Fluorescent Dyes”. In: *European J. Org. Chem.* 2018.14 (2018), pp. 1674–1681.

[7] Ursula Eisold et al. “Rigid Rod-Based FRET Probes for Membrane Sensing Applications”. In: *J. Phys. Chem. B* 120.37 (2016), pp. 9935–9943.

[8] P. Wessig et al. “Two-photon FRET pairs based on coumarin and DBD dyes”. In: *RSC Adv.* 6.40 (2016), pp. 33510–33513.

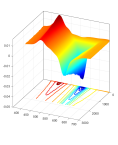

[9] Pablo Wessig et al. “FRET Pairs with Fixed Relative Orientation of Chromophores”. In: *European J. Org. Chem.* 2016.26 (2016), pp. 4476–4486.

[10] Robert Wawrzinek and Pablo Wessig. “Synthesis and spectroscopic properties of a FRET pair based on PPO and DBD dyes”. In: *Dye. Pigment.* 123.C (2015), pp. 39–43.

[11] Johanna Heuveling et al. “Conformational changes of the bacterial type i ATP-binding cassette importer HisQMP2 at distinct steps of the catalytic cycle”. In: *Biochim. Biophys. Acta - Biomembr.* 1838.1 PARTB (2014), pp. 106–116.

[12] Pablo Wessig et al. “Fluorescent dyes with large Stokes shifts based on benzo[1,2-d:4,5-d’]bis([1,3]dithiole) (“S4-DBD dyes”)”. In: *European J. Org. Chem.* (2020).

[13] Toni Haubitz et al. “Photophysics of Acyl- and Ester-DBD Dyes: Quadrupole-Induced Solvent Relaxation Investigated by Transient Absorption Spectroscopy”. In: *J. Phys. Chem. A* 123.22 (2019), pp. 4717–4726.

[14] Rasmus Bro. “PARAFAC. Tutorial and applications”. In: *Chemom. Intell. Lab. Syst.* 38 (1997), pp. 149–171.

[15] *MATLAB and Optimization Toolbox 2018b*. Natick, Massachusetts, 2019.

[16] Henk A. L. Kiers, Jos M. F. ten Berge, and Rasmus Bro. “PARAFAC2—Part I. A direct fitting algorithm for the PARAFAC2 model”. In: *J. Chemom.* 13.3-4 (1999), pp. 275–294.

[17] Rasmus Bro, Claus A. Andersson, and Henk A. L. Kiers. “PARAFAC2—Part II. Modeling chromatographic data with retention time shifts”. In: *J. Chemom.* 13.3-4 (1999), pp. 295–309.

[18] Michael Kasha. “Characterization of Electronic Transitions in Complex Molecules”. In: *Trans. Faraday Soc.* 9.c (1950), pp. 14–19.

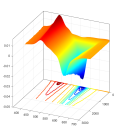

[19] Frank Neese. “Software update: the ORCA program system, version 4.0”. In: *Wiley Interdiscip. Rev. Comput. Mol. Sci.* (2018).

[20] Frank Neese. “The ORCA program system”. In: *Wiley Interdiscip. Rev. Comput. Mol. Sci.* (2012).

[21] A Becke. “B3LYP”. In: *J. Chem. Phys.* (1993).

[22] F. Weigend and R. Ahlrichs. “Balanced Basis Sets of Split Valence, Triple Zeta Valence and Quadruple Zeta Valence”. In: *Phys. Chem. Chem. Phys.* (2005).

[23] Jingjing Zheng, Xuefei Xu, and Donald G. Truhlar. “Minimally augmented Karlsruhe basis sets”. In: *Theor. Chem. Acc.* 128.3 (2011), pp. 295–305.

[24] Arnim Hellweg et al. “Optimized accurate auxiliary basis sets for RI-MP2 and RI-CC2 calculations for the atoms Rb to Rn”. In: *Theor. Chem. Acc.* 117.4 (Apr. 2007), pp. 587–597.

[25] Florian Weigend. “Accurate Coulomb-fitting basis sets for H to Rn”. In: *Phys. Chem. Chem. Phys.* 8.9 (2006), pp. 1057–1065.

[26] Martin P. Rauch and Robert R. Knowles. “Applications and prospects for triplet–triplet annihilation photon upconversion”. In: *Chimia (Aarau).* 72.7-8 (2018), pp. 501–507.

[27] John B. Birks. *Photophysics of aromatic molecules*. London: Wiley-Interscience, 1970, p. 704.

[28] David R. Lide. *CRC Handbook of Chemistry and Physics*. 84th. Boca Raton, FL: CRC Press, 2004, pp. 153–155.

[29] G. Lancelot. “The role of sulphur 3d orbitals in spin-orbit coupling of thiopurines and thiopyrimidines”. In: *Mol. Phys.* 31.1 (1976), pp. 241–254.

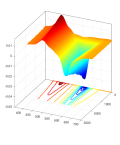

[30] Denisio M. Togashi et al. “Electric polarization effects on the electronic spectral shift of centrosymmetric compounds”. In: *Chem. Phys.* 300.1-3 (2004), pp. 267–275.

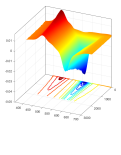

3.3 pH Sensitive Fluorescence Switching of Pyridylanthracenes: The Effect of the Isomeric Pattern

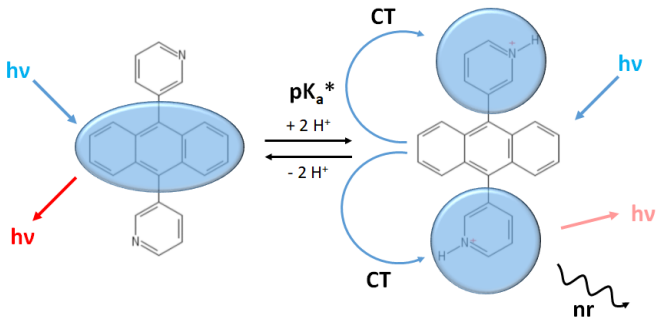

Figure 3.3.1: TOC graphic of "pH-Sensitive Fluorescence Switching of Pyridylanthracenes: The Effect of the Isomeric Pattern".

Haubitz, T., Fudickar, W., Linker, T., & Kumke, M. U., pH-Sensitive Fluorescence Switching of Pyridylanthracenes: The Effect of the Isomeric Pattern. *Journal of Physical Chemistry A*, 2020, *124*(52), 11017–11024.

Personal Contribution:

The used samples in this manuscript were synthesized and provided by the "organic chemistry" department of Prof. T. Linker by W. Fudickar. All absorption, luminescence measurements, and theoretical calculations were conducted by W. Fudickar. All transient absorption measurements, data evaluation, tables, and graphs were done by myself. Furthermore, the large majority of the data interpretation, discussion, and conclusions were done by me. The writing of the manuscript was done in majority by me and in part by W. Fudickar.

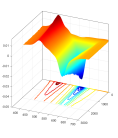

pH Sensitive Fluorescence Switching of Pyridylanthracenes: The Effect of the Isomeric Pattern

Toni Haubitz, Werner Fudickar, Torsten Linker, and Michael U. Kumke

University of Potsdam, Institute of Chemistry, Karl-Liebknecht-Str. 24-25, D-14476 Potsdam, Germany

3.3.1 Abstract

The class of 9,10-substituted anthracenes are known for their useful optical properties like fluorescence, which makes them frequently used probes in sensing applications. In this paper we investigate the fundamental photophysical properties of three pyridyl substituted variants. The nitrogen atoms in the pyridinium six-membered rings are located in the ortho-, meta-, or para position in relation to the anthracene core. Absorption, fluorescence, and transient absorption measurements were carried out and were complemented by theoretical calculations. We monitored the photophysics of the anthracene derivatives in chloroform and water investigating the protonated as well as their non-protonated forms. We found that the optical properties of the non-protonated forms are strongly determined by the anthracene chromophore, with only small differences to other 9,10 substituted anthracenes, for example diphenyl anthracene. In contrast, protonation leads to a strong decrease in fluorescence intensity and lifetime. Transient absorption measurements and theoretical calculations revealed the formation of a charge-transfer state in the protonated chromophores, where electron density is shifted from the anthracene moiety towards the protonated pyridyl substituents. While the para- and ortho-derivatives' charge transfer are still moderately fluorescent, the meta derivative is affected much stronger and shows nearly no fluorescence. This nitrogen-atom-position dependent sensitivity to hydronium activity makes a combination of these fluorophores very attractive for pH sensing applications covering a broadened pH range.

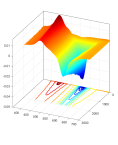

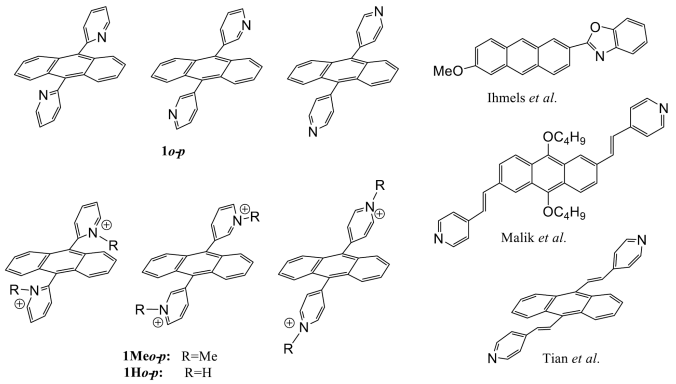

Figure 3.3.2: Structures of anthracene based fluorophores [5, 6, 7].

3.3.2 Introduction

Anthracenes belong to the class of polyaromatic hydrocarbons, which are important for applications as sensors and luminescent devices (e.g., in photonics, optoelectronics, and energy harvesting applications) owed to their optical properties [1, 2, 3, 4]. In combination with a specific substituent such fluorophores can be useful as pH or ion sensors since they respond on binding by a noticeable color change. A straight forward strategy towards their design is to endow the anthracene core with a substituent, which becomes converted into a π-acceptor moiety upon protonation or complexation. The changes in structure can correlate with a shift of wavelengths in absorbance and emission spectra but also with fluorescence quenching.

Examples of such anthracene-based fluorophores are presented in Figure 3.3.2. Ihmels et al. attached an oxazoline at the 2-position of the anthracene [5, 8]. Generation of the oxazolinium upon protonation resulted in a strong red-shift of absorbance and emission spectra, which allowed its use as indicator. A 2,6-di-*p*-vinylpyridine appended anthracene was used by Malik et al. to detect picric acid [6]. Protonation of the pyridines caused rather small changes in absorbance spectra but a strong quenching of the emission as result of intramolecular charge transfer (ICT). Finally, also a 9,10 substituted *p*-divinylpyridylanthracene was investigated by Tian et al. This system responded to pH-alteration by a strong red-shift of absorbance and emission but not by noticeable reduction of emission

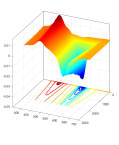

intensity [7]. All these reports led to believe that influences of such acceptor units on the main chromophore are hardly predictable and don't follow a clear pattern. However, an unraveling of such effects would be supported by comparison of a series of isomers, which vary only by one simple pattern. Such a pattern, for example, is accessible by using isomeric pyridine substituents. Indeed, Linker et al. recently introduced a series of ortho-, meta-, and para substituted 9,10-dipyridylanthracenes *10-p* (see Figure 3.3.2), which could ideally serve as such reference fluorophores [9]. Initially, our interest was directed towards the reversible reaction between these compounds and singlet oxygen to give endoperoxides. However, since the kinetic of this reaction is clearly related to the electron donor/acceptor properties of the substituent, [10, 11] we became interested in effects arising from alkylation of the pyridyl units [12]. Their conversion into the methylated forms 1Me*o-p* rendered them water soluble and made them strong DNA binders [13]. Interestingly, while the non-protonated forms in organic solvents behaved indistinguishable, the absorption and emission spectra of 1Me*o-p* in water showed strong differences between each other based on the position of the nitrogen atom. The most intriguing observation, however, was that the meta isomer 1Me*m* exclusively showed no fluorescence. Thus, variation of the isomeric pattern of positively charged pyridiniumanthracenes results in different effects of bathochromism and ICT. This prompted us to more deeply investigate the gradual transition from the free-base pyridylanthracenes *10-p* to the corresponding complexed forms. This could be accomplished by gradual protonation to finally give *10*-H-*p*-H, which we present herein (Figure 3.3.2). Localization and delocalization of excitation energy in combination with structural motion in excited state has been investigated for anthracene in combination with different substituents in 9,10-position, such as benzothiazole [14] or pyrimidine [15]. The dynamic planarization of molecules and subsequent consequences for a charge transfer, e.g., twisted vs. non-twisted intramolecular charge transfer, excited state torsion-induced non-radiative deactivation ("molecular rotor"), were considered. For the understanding of excited state conformational motion triggered by delocalization/localization of electronic energy and subsequently electronic charge distribution a well-defined class of reference molecules is desirable. Here, *10-p* and *10-H-p*-H as model compounds come into play. *10-p* are small molecules con-

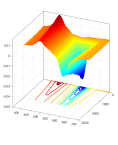

sisting of two planar sub-units (anthracene and pyridine) with a limited spectrum of possible motion relative to each other (only rotation of the pyridine unit relative to the plane of the anthracene — leaving only one degree of conformational freedom). The spectral pattern related to the anthracene unit is very specific and easily identified in the spectra. The positon of the nitrogen atom in the pyridine unit relative to the anthracene can be systematically varied and moreover, easily protonated allowing for a systematic study on the influence of charge loclization/delocalization and spatial limitations.

3.3.3 Experimental Section

Syntheses of the pyridylanthracenes 10-p. The synthesis of the three pyridylanthracene isomers has been described in detail previously [9]. *Protonation with trifluoroacetic acid (TFA) in $CHCl_3$.* Solutions of the pyridylanthracenes in $CHCl_3$ ($1 \cdot 10^4$ M) were prepared as samples of 2 mL. The samples were titrated with TFA from a stock solution in $CHCl_3$ (0.1 M) starting with an aliquot of 2 µL. For fluorescence spectra both, sample and TFA stock solution were diluted 10 times. *Preparation of aqueous solutions.* Dissolving of the pyridylanthracenes in water was realized by using 10% methanol as co-solvent. Therefore, anthracenes were first dissolved in 10% methanol/water ($1 \cdot 10^{-3}$ M) followed by dilution with water. To adjust pH=1, dilution was carried out with aqueous HCl (0.1 M). Solutions having various pH values between pH=1 and 9 were prepared by using a phosphate buffer, to which HCl (1 M) was added. pH values were then measured by using a standard pH meter (Hanna). In the transient absorption (TA) measurements [16, 17] a Ti:sapphire laser system (Spitfire Ace PA, Spectra Physics) operated at 800 nm was used. The transient absorption spectrometer (TAS, Newport) was combined with a HE-TOPAS (Light Conversion) as pump source (pump wavelength of 275 nm, unless stated otherwise) at a one kHz repetition rate and 40 fs pulse width. The pump power was adjusted via a ND-filter wheel and measured by a PEPS-3-9.5 sensor (Newport). As probe beam a white light continuum (350 nm < λ_{probe} < 700 nm) generated with a CaF_2 crystal, was applied. The signal is generated as the difference in optical density (ΔOD) between the sample without and with irradiation by the pump pulse. The time delay was adjusted by a variable delay line between 0 ns to 7 ns. The system

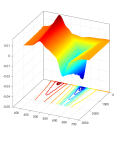

IRF was measured to be 90 fs to 150 fs depending on the probe wavelength and solvent used. Samples were measured in a quartz cuvette with 2 mm optical path length (Typ 21, Starna GmbH). The samples were stirred by an Electronic Stirrer Model 300 (Rank Brothers Ltd.). Measurements were performed depending on irradiation time by measuring several 2D spectra over the course of an hour, to compensate photodegradation effects interfering with later analysis. Data deconvolution in spectral and time domain was performed using the Parallel Factor Analysis (PARAFAC) algorithm [18] implemented in the optimization toolbox of MATLAB 2018b (MathWorks) [19] after a second-order polynomial time domain baseline-correction to compensate for dispersion. General data treatment, peak fitting and data plotting was carried out using Origin 2018 (OriginLab, Northampton, MA). Absorption spectra were recorded on a Unicam UV3 spectrometer. Steady state fluorescence spectra were measured on a Jasco FP 6300 spectrometer. Gains were adjusted according to the intensities ($CHCl_3$=low, water=high). Fluorescence quantum yields were determined from equation (3.34) [20],

$$\Phi = \Phi_{\text{ref}} \cdot \left(\frac{I}{I_{\text{ref}}}\right) + \left(\frac{A}{A_{\text{ref}}}\right) \tag{3.34}$$

where Φ_{ref} is the quantum yield of a reference. For the non-protonated forms dissolved in $CHCl_3$ 9,10-dicyanoanthracene was used ($\Phi_{\text{ref}} = 0.63$) [21], in water at pH = 7 1-anthracenesulfonate ($\Phi_{\text{ref}} = 0.25$) [22], and at pH=1 quinine sulphate ($\Phi_{\text{ref}} = 0.55$) [20]. I and I_{ref} are the integrated areas of the emission peaks, and A and A_{ref} are the absorbances at excitation wavelength (375 nm) of the acene and the reference, respectively. Refractive indexes are not considered since solvents of sample and reference were identical. Theoretical calculations were performed by using the Gaussian 09 D0.1 software. A 6-31G* basis set and the B3LYP functional were applied for the optimization of the ground state structures. This calculation was performed with a frequency analysis, which confirmed the absence of imaginary frequencies and a regular population analysis in order to obtain the energy and profiles of the highest occupied and lowest virtual orbitals. The solvent was included by a self-consistent reaction field (SCRF) method using the conductor-like polarizable continuum model (CPCM) with the solvents chloroform and water. Using these structures TD-DFT calculations were performed with a

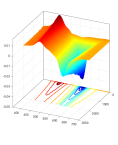

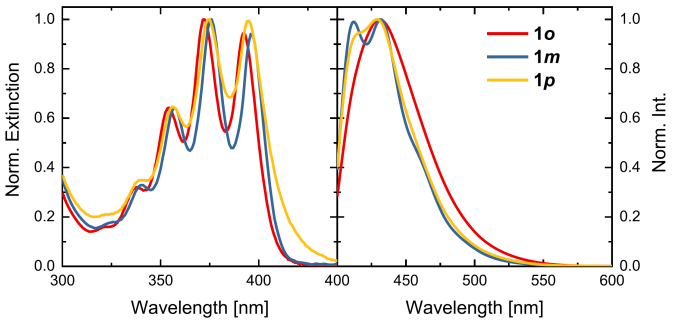

Figure 3.3.3: Absorption (left, 10^{-4} M acene) and fluorescence (right, λ_{ex} = 375 nm, 10^{-5} M acene) spectra of ***1o-p*** in chloroform.

PBE1PBE functional to obtain the first 10 vertical excitations. Allowed and forbitten transitions were identified based of the oscillator strength *f*.

3.3.4 Results and Discussion

In Figure 3.3.3 the absorption (left) and the emission (right) spectra of *1o-p* in chloroform are compared. In the absorption spectra the typical anthracene vibrational pattern of C-C as well as C-H bonds was observed. Within the three anthracene derivatives (*1o-p*) only very small differences in the peak location were found in their absorption spectra, with the meta derivative being the furthest red-shifted. In contrast, the fluorescence spectra (Figure 3.3.3, right) show larger deviation of the spectral intensity distribution when compared to unsubstituted anthracene. The vibrational pattern is less resolved. This already indicates that upon excitation in a locally excited state (anthracene chromophore) the molecules undergo an intramolecular rearrangement and the emissive state is no longer of pure anthracene character. Charge redistribution due to an intramolecular charge transfer (ICT) possibly in combination with a reorientation (rotation as well as planarization) of the pyridyl units could occur. Such mechanism has been described for other 9,10-anthracene derivatives carrying acceptor units [14, 15]. In order to further elucidate the influence of the position of the nitrogen on the excited state processes we investigated the effect of protonation on the photophysics of *1o-p*.

Absorption and emission spectra — influence of protonation in $CHCl_3$

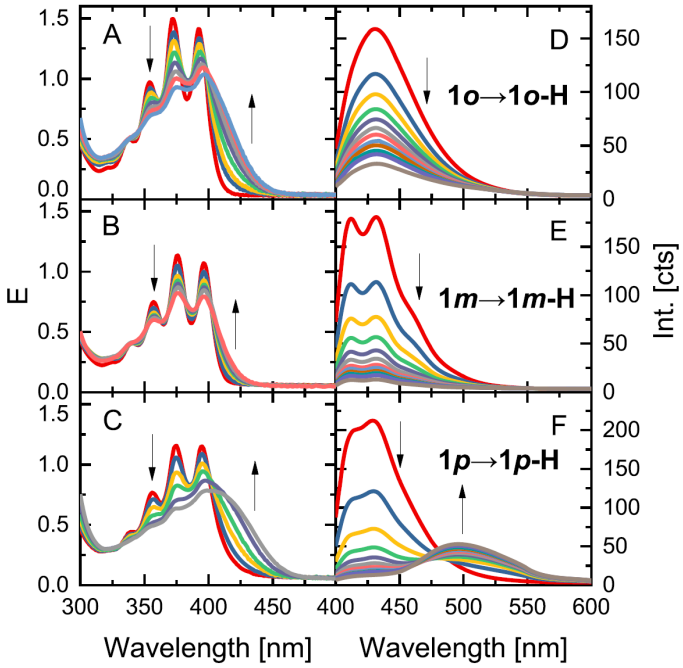

Figure 3.3.4: Left: UV/Vis absorbance spectra in $CHCl_3$ upon addition of TFA to ortho- (A), meta- (B), and para- (C) pyridinium anthracene. Concentrations: 10^{-4} M acene and 0 to 10^{-2} M for TFA. Right: Emission spectra (excitation at 375 nm) of ortho- (D), meta- (E), and para- (F) pyridinium anthracene upon addition of TFA. Concentrations: 10^{-5} M acene and 0 and 10^{-3} M for TFA.

Table 3.3.1: Spectroscopic data of the pyridylanthracenes **1*o*-*p*** and their protonated forms **1*o*-H-*p*-H**. [a]Excitation at 375 nm, [b]9,10-dicyanoanthracene used as reference. [c]Quinine sulphate used as standard at pH 1 and 1-anthracenesulfonate as standard at pH 7.

Species	in $CHCl_3$			in H_2O/1% methanol		
	λ_{max} / nm	I^a_{max} / nm	Φ^b	λ_{max} / nm	I^a_{max} / nm	Φ^c
1*o*	354, 372, 392	430	0.58	352, 370, 390	426	0.07
1*o*-H	356, 374, 394	-	□ 0	375, 394	495	< 0.01
1*m*	365, 375, 395	412, 431	0.67	363, 381, 403	417, 438	0.04
1*m*-H	365, 374, 395	-	□ 0	356, 372, 393	530	□ 0
1*p*	365, 373, 393	428	0.62	361, 380, 402	415, 438	0.17
1*p*-H	378, 402, 426	498	0.13	396	536	< 0.01

Chloroform solutions of the three isomeric pyridylanthracenes were titrated with trifluoroacetic acid (TFA). As shown in the absorption spectra (Figure 3.3.4A–C) 1*o*-*p* all show a distinct alteration of their absorption spectra upon addition of TFA. In all cases the intensity of the vibrational bands is decreased and a new lower energy, less structured absorption evolves, for which it is tempting to attribute it to the protonated forms of the respective molecule. This is strongest pronounced for the ortho and para isomers and only weakly seen for the meta isomer (see Figure 3.3.4 A–C).

The loss of the vibrational structure upon protonation in the absorption spectra indicates that the (Franck–Condon) excited state of the molecules is no longer dominated by the "pure" anthracene chromophore. Instead a noticeable participation of the pyridine units to the overall light absorption of the molecules is seen, most probably due to a charge transfer. Complementary to the alteration in the absorption also the fluorescence is affected. Here, a strong decrease of the fluorescence intensity upon titration with TFA is found (Figure 3.3.4 D–F). Striking is also that a new emission emerges for the para isomer, for which its maximum is red-shifted by about 70 nm. It is tempting to assign this new emission to the protonated species (1*p*-H) with a strong Stokes shift as compared to its free base form (1*p*). Upon TFA titration of the other two isomers, new emission maxima could be also found, yet at significantly weaker intensity. The specific absorption and emission properties of both the free bases and the protonated forms of the three isomers are summarized in Table 1.

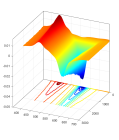

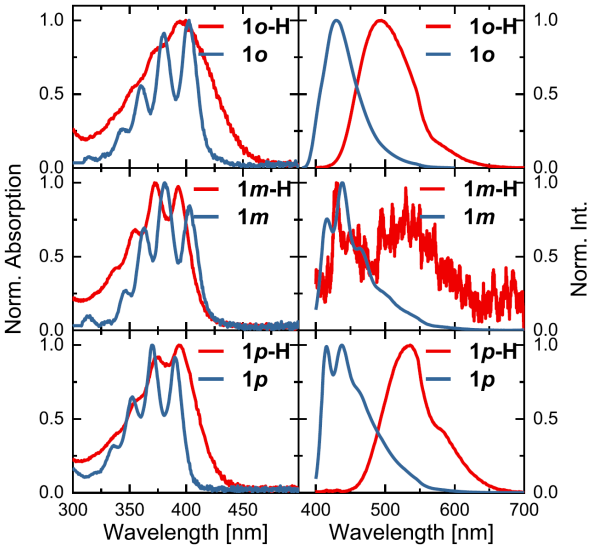

Figure 3.3.5: Absorption (left) and emission spectra (right) of the ortho (top), meta (middle), and para (bottom) isomer at pH 1 (red curve) and pH 7 (blue curve) in water. Acene concentration was 10^{-5} M, λ_{ex} = 375 nm. Aqueous solutions contain 0.1% methanol for solvation. High gain setting necessary in acidic samples.

Absorption and emission spectra — influence of protonation in water

As can be seen in Figure 3.3.5, the spectral behaviour is quite similar in aqueous solution as it is in chloroform. Besides a massive drop in fluorescence intensity (and consequently in quantum yield, see Table 3.3.1) we see a strong red shift of the emission, which is strongest for 1*p*-H. The decrease in vibronic features is here as well indicative of a strong participation of the pyridine substituents to the absorption and emission compared to the anthracene dominated absorptions and emissions of the unprotonated molecule. It is also apparent that the meta fluorescence is even lower than that of the other isomers (vide infra).

For a pK_a determination we measured the fluorescence of buffered aqueous solutions of the compounds in the range between pH 1 and pH 9. Plotting the emission intensities of the three isomers at different pH revealed that protonation of the excited state occurs between pH 3 and 7 (Figure 3.3.6). All isomers show signs of the expected two pK_a values, first for the protonation of one of the pyridinium nitrogens and then for the second. While the meta- and para-isomer have clear steps in their emission intensities, the ortho isomer shows only one significant step. However, as one can also see is

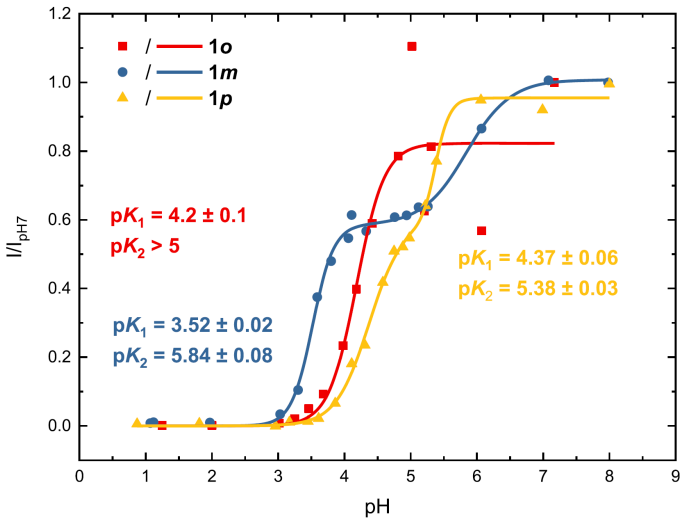

Figure 3.3.6: Plot of the emission intensities of pyridylanthracenes **1*o*-*p*** against the pH. Emission wavelength corresponds to the data assembled in Table 3.3.1 and are normalized to intensity at pH 8. Acene concentration was 10^{-5} M, λ_{ex} = 375 nm. Aqueous solutions contain 0.1% methanol for solvation. Sigmoidal fits are used for pK_a determination.

that the data points above a pH of 5 are more scattered for the ortho-isomer, which can be attributed to the low emission intensity due to low solubility in its neutral form. So an increase in noise is equivalent to the molecule becoming charge neutral, i.e. deprotonation.

From data analysis using a sigmoidal fit function we determined the pK_a values of the isomers (see Figure 3.3.6). It is important to mention that the determined pK_a values are the values of the excited molecule and not of the ground state molecule, as the determination was done based on the fluorescence spectra. Ground state pK_a values can be (but do not have to be) different from excited state ones depending on the molecule [23]. Due to low concentration/solubility of the unprotonated samples, ground state pK_a determinations could not be conducted by absorption spectroscopy. With respect to pH sensing applications the three isomers cover the medium pH range (ca. $3 < pH < 6$) and using a combination of them in an optical sensor would increase the applications range compared to single chromophores. Here, the advantage would be that with respect to instrumental parameters like excitation and emission no adaptations would be necessary, which minimizes costs. It is intriguing that the observed pK_a values with respect to the nitrogen position did not follow the expected order "para-ortho-meta" based on mesomerism, which consider the ground state properties. The observed

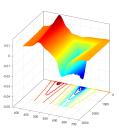

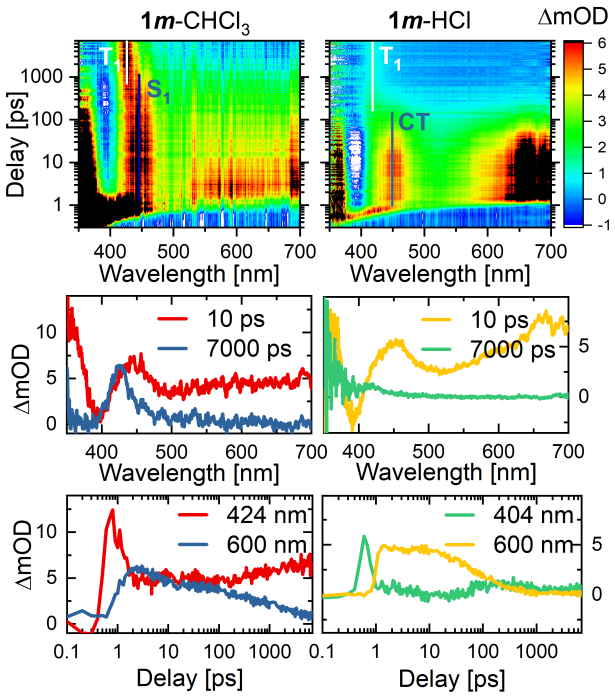

Figure 3.3.7: TAS spectra of **1*m*** in $CHCl_3$ (left) and HCl (right) at λ_{ex} = 275 nm and a pulse energy of 1.5 μJ. Acene concentration is 10^{-5} M.

(opposite) trend seemed to be better correlated with the excited state properties, which may be a consequence of the fact that the pK_a values were determined by fluorescence.

Transient Absorption Spectroscopy

In Figure 3.3.7 the transient absorption spectra (TAS) of the meta derivative are displayed. In chloroform (left) typical anthracene signals can be observed [24]. After 1 ps the formation of the anthracene dominated singlet state (S_1) is visible with a broad transient absorption (positive signal) which is having a higher intensity at the blue end of the spectrum. This broad positive absorption is superimposed by a negative peak at around 400 nm, which can be interpreted as the ground state bleach (GSB) of the anthracene which is indicating the depletion of the number of molecules in the ground state. This GSB is additionally superimposed by the negative stimulated emission signal of the S_1, giving the whole peak a broad and unstructured appearance. After this initial formation of S_1 we can see its decay on the nanosecond timescale, which resembles the return of the molecules form the

S_1 to the ground state and includes the fluorescence lifetime of the molecule (bottom left, blue curve). However, simultaneously to the depopulation of the S_1 the formation of a new signal is visible at 420 nm. This signal can be assigned to the population of the triplet state of anthracene via inter-system crossing (ISC) [24]. Some of the 9,10-substituted anthracenes are known for a high ISC quantum yield [25] which is reducing the fluorescence quantum yield as the fluorescence is competing with the ISC. On the other hand, transient absorption spectra of the protonated form (See Figure 3.3.7, only fully protonated forms present in the excited state at pH 0) show two distinct changes: 1) The decay time of molecules in the initial fluorescent state is strongly decreased from several nanoseconds to several hundred picoseconds, which explains the quenching of the fluorescence intensity upon protonation (see Figure 3.3.4 D-F, and Table 3.3.1), and 2) additional absorptions at the red end of the spectrum (around 650 nm) indicating the involvement of more excited states in the deactivation process(es) than in the unprotonated molecule. As the intensity of the absorption related to the anthracene-dominated triplet state is decreased, we can conclude that the triplet state is less populated and that the quenching of fluorescence is most likely not introduced by an increased ISC rate but instead by faster competing non-radiative decay mechanisms.

DFT Calculations

To further investigate the involved electronic states of the derivatives, the first 20 lowest excited states of the pyridylanthracenes were computed by time dependent density functional theory (TD-DFT) using the PBE1PBE functional [26]. Vertical transitions were taken from optimized ground state structures calculated on the B3LYP/6-31p* level [27]. The results for the three anthracenes in the solvent $CHCl_3$ based on the CPCM model can be seen in Figure 3.3.8. For all three isomers calculations revealed only one pertinent excitation, which is assigned to a transition from the HOMO into the LUMO, which is a π^* orbital (Figure 3.3.8) corresponding to an anthracene-dominated transition. The calculated wavelength of ca. 365 nm is in range of experimental values, though systematically off by around +0.24 eV. The lowest unoccupied orbital is probably the one populated by the electron after exciting the molecule, leading to the first excited singlet state S_1, which is (as only anthracene

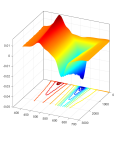

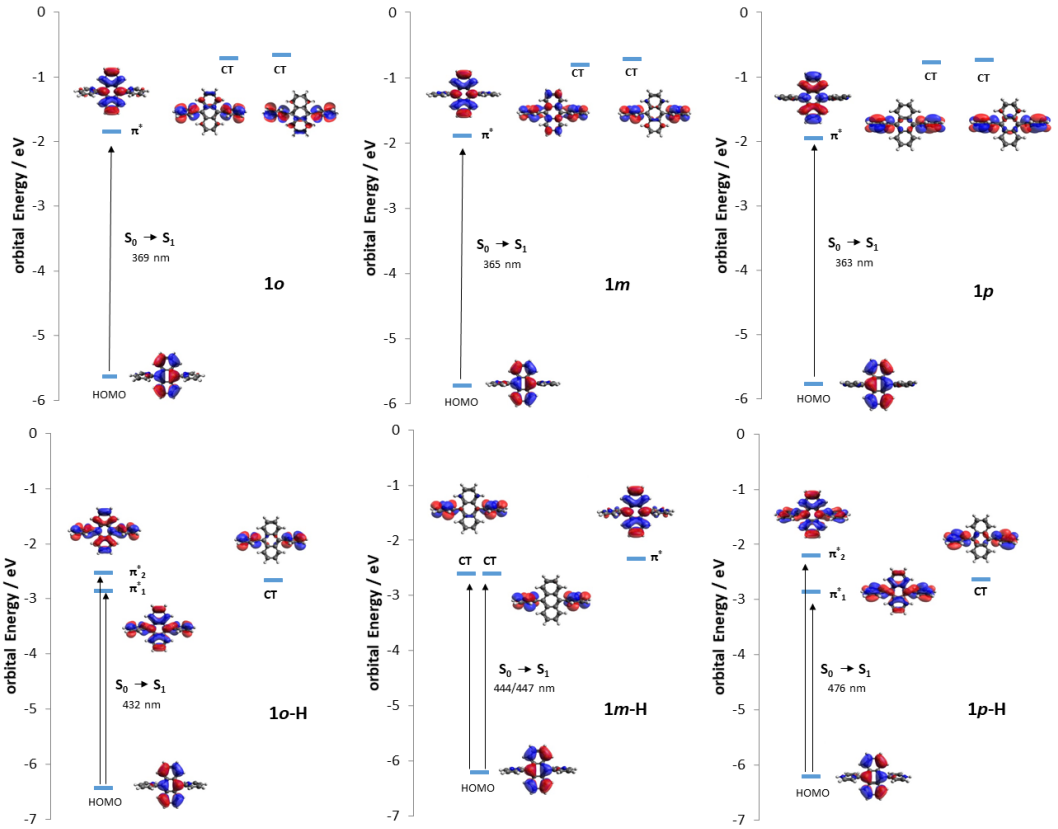

Figure 3.3.8: Diagram showing orbital energies involving the first optical transitions. Ground state geometry optimization were conducted on the B3LYP/6-31p* level with CPCM solvation model, while transitions were calculated by TD-DFT with PBE1PBE functional. Top row left to right: Pyridiniumderivatives ortho, meta, and para in $CHCl_3$. Bottom row left to right: Protonated pyridiniumderivatives ortho, meta, and para in water.

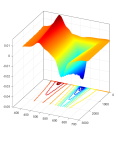

orbitals are involved) equivalent to an anthracene S_1. This state is then the fluorescing state of the pyridiniumanthracenes with its typical anthracene optical properties. However, as can be seen from the emission spectra (Figure 3.3.3) the fluorescence is broadened and it does not resemble the typical symmetric behaviour relative to its absorption spectrum as pure anthracene would. This broadening and loss of vibronic character is attributed to the pyridyl substituents. We assume that after initial excitation the molecule is reorganizing into a more planar and more stiff configuration altering the features of the fluorescence spectra (see Figure 3.3.4 and Figure 3.3.5). TD-DFT calculations of the di-cationic forms *1o*-H-*p*-H with water as solvent for the CPCM model yielded significantly different results (Figure 3.3.8): For the ortho- and para-derivatives, two options for the first excited state corresponding to a transition into two orbitals (LUMO and LUMO+2) are found. Both show a strong orthogonal electron density assigned to the pyridinium groups in addition to the population of the acene moiety (Figure 3.3.8). Importantly, both isomers have an orbital (i.e. LUMO+1), which cannot be accessed directly upon excitation from the ground state. Its population is oriented orthogonally with respect to the acene plane. However, its energy lies about 0.3 eV below the LUMO+2. Thus charge transfer (CT) from LUMO+2 into LUMO+1 could occur. In contrast to the other two isomers, the absorption spectrum of *1m*-H is dominated by an electronic transition which directly promotes into LUMO+2. Thus two orbitals with CT character lie below and become accessible. As it becomes clear from Figure 3.3.8, protonation causes for all three isomers stabilization of CT orbitals with population at the pyridinium sites. This lowering in energy makes this orbital accessible by an electron through the anthracene dominated S_1 state, which then forms a molecule in a CT state. In addition, this state is then probably energetically lowered even further due to stabilization through solvent relaxation (SR). The reason behind this is, that the strong polar character of the protonated forms leads to strong solvent reorganization in strongly polar solvents [28]. Both of these stabilization factors make the CT state now the excited state with lowest energy and by this the favoured excited state over the anthracene-dominated excited state. The formation of CT state explains the observed weak fluorescence due to protonation, as this state is photophysically different than the anthracene-dominated S_1 state and is

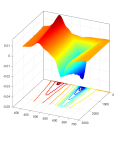

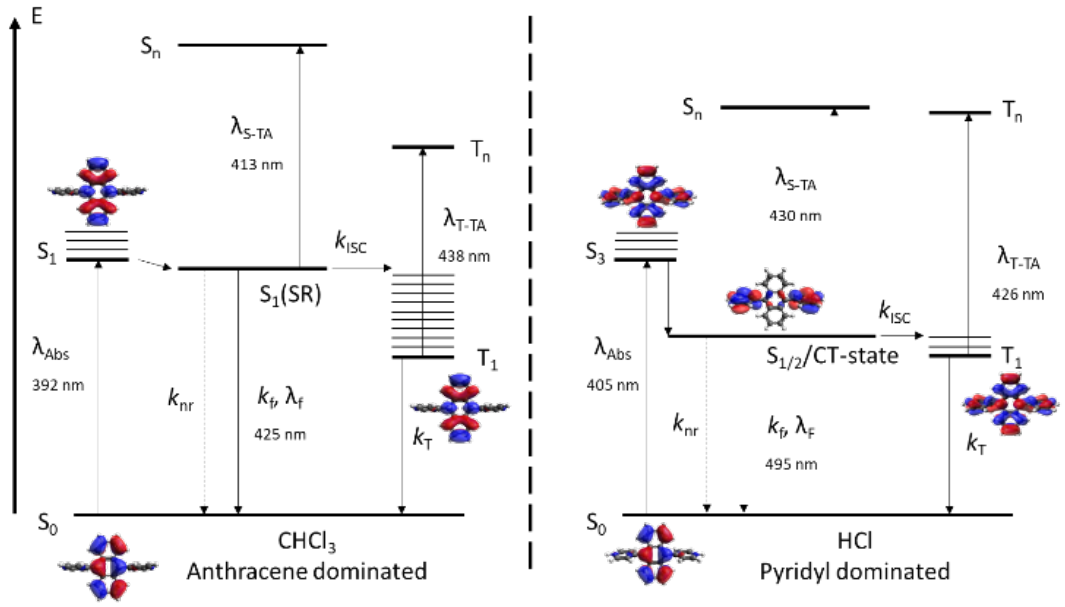

Figure 3.3.9: General scheme of the pyridiniumanthracene's Jabłoński-diagram (ortho derivative as example) in $CHCl_3$ (left) and 1 M HCl (right). Transition energies not to scale.

probably experiencing stronger quenching effects, either vibrational relaxation or quenching by solvent molecules. As these quenching effects are visible in both water and chloroform, we can exclude proton abstraction/intramolecular proton transfer.

With the information of the involved electronic states we can now assign the bands in the transient absorption to photophysical processes (see Figure 3.3.9). The initial state of the unprotonated molecule is the fluorescent S_1 state of the anthracene moiety and behaves photophysically very similar to pure anthracene, except the vibrational pattern of the emission (vide supra). The absorption signals are assigned as singlet transient absorptions (S-TA) into higher singlet states S_n. After initial excitation, the solvent molecules have to adjust to the new dipole moment of the molecule which lowers the energy of the initial S_1 state, this is known as solvent-relaxation (SR). The fluorescence is in competition with the anthracene typical triplet state T_1 (via ISC), which has a 420 nm absorption (T-TA) into higher triplet states Tn. The initial excited state of the protonated molecules can then be assigned to the lower lying CT-state with the electron density moved towards the protonated pyridinyl rings.

Table 3.3.2: Data from TAS measurements of the three isomeric pyridylanthracenes in chloroform and in 1 M HCl.

Species	$\lambda_{S\text{-}TA}$ [nm]	$\lambda_{T\text{-}TA}$ [nm]	$\frac{1}{k_f+k_{ISC}+k_{nr}}$ [ps]	$\frac{1}{k_T}$ [ns]
1*o*	413	438	1020 ± 70	>7
1*m*	445	425	1400 ± 95	>7
1*p*	402	<390	4200 ± 200	>7
1*o*-H	430	426	495 ± 5	>7
1*m*-H	450	416	119 ± 3	>7
1*p*-H	480	370	540 ± 20	>7

This state must be energetically lower than the anthracene S_1 state, as its very weak emission is strongly red shifted (see Figure 3.3.5). The strong quenching and limited formation of triplet indicates a strong solvent or vibrational relaxation.

The exact energies and rates for each derivative can be found in Table 3.3.2. As can be seen from the lifetime of the S_1/CT state ($1/(k_f+k_{ISC}+k_{nr})$) and as previously discussed we can clearly show that the fluorescence is dramatically different upon protonation with water by a factor of 2 – 10. This drastic shortening of the luminescent states lifetime is complemented by the low quantum yield (< 0.01) of the fluorescence, as nearly all CT molecules decay via a non-radiative pathway. Furthermore one can see from the S_1 deactivation rates in Table 3.3.2 and the fluorescence spectra in Figure 3.3.5 that the meta-isomer fluorescence is even stronger quenched than of the other two isomers. We attribute this effect to the stronger conjugation between the anthracene core and the pyridinyl substituents in comparison to the ortho- and para-isomer, which leads to a shorter bond and more vibrational interaction between the two moieties. This decrease in degrees of freedom and the additional interactions lead to even more deactivation pathways (higher k_{nr}) and thus lower fluorescence in the meta-isomer.

3.3.5 Conclusion and Outlook

We could conclusively show, that the reason for fluorescence quenching of pyridinium anthracenes by protonation is caused by the formation and energetic stabilization of the pyridine dominated charge-

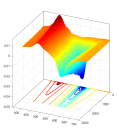

transfer state. This state exhibits a far lower fluorescence quantum yield mostly due to additionally introduced non-radiative decay processes and less by a change in the rate of ISC to triplet anthracene.

3.3.6 Acknowledgement

T.H. and M.U.K. are grateful to the Federal Ministry for Economic Affairs and Energy for the financial support (contract number 02E11415F).

3.3.7 Abbreviations

S, Singlet; CT, charge-transfer; T, Triplet; TAS, Transient absorption spectroscopy; TA, Transient absorption; GSB, Ground state bleach; SR, Solvent-relaxation; ISC, intersystem crossing; HOMO, Highest occupied molecular orbital; LUMO, Lowest unoccupied molecular orbital; TD-DFT, Time-dependent density functional theory; m, Meta; o, Ortho; p, Para; TFA, Trifluoroacetic acid

References

[1] Thomas J. J. Müller and Uwe H. F. Bunz. *Functional Organic Materials*. Weinheim: WILEY-VCH Verlag, 2007, pp. 511–546.

[2] John E. Anthony. "Functionalized acenes and heteroacenes for organic electronics". In: 106.12 (2006), pp. 5028–5048.

[3] Hong Gyu Lee et al. "An anthracene-based fluorescent sensor for sequential detection of zinc and copper ions". In: *Inorg. Chem. Commun.* 39 (2014), pp. 61–65.

[4] Chao Yao et al. "Highly fluorescent anthracene derivative as a non-fullerene acceptor in OSCs with small non-radiative energy loss of 0.22 eV and high PCEs of over 13%". In: *J. Mater. Chem. A* 7.17 (2019), pp. 10212–10216.

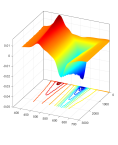

[5] Heiko Ihmels et al. “Anthryl-substituted heterocycles as acid-sensitive fluorescence probes”. In: *J. Org. Chem.* 70.10 (2005), pp. 3929–3938.

[6] Dines Chandra Santra et al. “Charge-Transfer-Induced Fluorescence Quenching of Anthracene Derivatives and Selective Detection of Picric Acid”. In: *Chem. - A Eur. J.* 22.6 (2016), pp. 2012–2019.

[7] Yujie Dong et al. “Multi-stimuli responsive fluorescence switching: The reversible piezochromism and protonation effect of a divinylanthracene derivative”. In: *J. Mater. Chem. C* 1.45 (2013), pp. 7554–7559.

[8] Heiko Ihmels, Andreas Meiswinkel, and Christian J. Mohrschladt. “Novel fluorescence probes based on 2,6-donor-acceptor-substituted anthracene derivatives”. In: *Org. Lett.* 2.18 (2000), pp. 2865–2867.

[9] Werner Fudickar and Torsten Linker. “Synthesis of Pyridylanthracenes and Their Reversible Reaction with Singlet Oxygen to Endoperoxides”. In: *J. Org. Chem.* 82.17 (2017), pp. 9285–9262.

[10] Werner Fudickar and Torsten Linker. “Why triple bonds protect acenes from oxidation and decomposition”. In: *J. Am. Chem. Soc.* 134.36 (2012), pp. 15071–15082.

[11] Werner Fudickar and Torsten Linker. “Remote substituent effects on the photooxygenation of 9,10-diarylanthracenes: strong evidence for polar intermediates.” In: *Chem. Commun.* (2008), pp. 1771–1773.

[12] Werner Fudickar and Torsten Linker. “Singlet Oxygen Release of Singlet Oxygen from Aromatic Endoperoxides by Chemical Triggers Angewandte”. In: *Angew. Chem. Int. Ed.* 57.39 (2018), pp. 12971–12975.

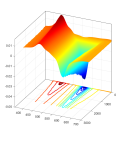

[13] Werner Fudickar and Torsten Linker. “Structural motives controlling the binding affinity of 9,10-bis(methylpyridinium)anthracenes towards DNA”. In: *Bioorg. Med. Chem.* 28.8 (2020), p. 115432.

[14] Rajib Ghosh et al. “Ultrafast Conformational Relaxation Dynamics in Anthryl-9-benzothiazole: Dynamic Planarization Driven Delocalization and Protonation-In-duced Twisting Dynamics”. In: *J. Phys. Chem. B* 123.25 (2019), pp. 5307–5315.

[15] Antonio Santoro et al. “Pyrimidyl-substituted anthracene fluorophores: Syntheses, absorption spectra, and photophysical properties”. In: *Dye. Pigment.* 159 (2018), pp. 619–636.

[16] Toni Haubitz et al. “Photophysics of Acyl- and Ester-DBD Dyes: Quadrupole-Induced Solvent Relaxation Investigated by Transient Absorption Spectroscopy”. In: *J. Phys. Chem. A* 123.22 (2019), pp. 4717–4726.

[17] Toni Haubitz et al. “Investigating the Sulfur ”Twist” on the Photophysics of DBD Dyes”. In: *J. Phys. Chem. A* 124.22 (2020), pp. 4345–4353.

[18] Rasmus Bro. “PARAFAC. Tutorial and applications”. In: *Chemom. Intell. Lab. Syst.* 38 (1997), pp. 149–171.

[19] *MATLAB and Optimization Toolbox 2018b*. Natick, Massachusetts, 2019.

[20] Knut Rurack. “Fluorescence Quantum Yields: Methods of Determination and Standards”. In: *Stand. Qual. Assur. Fluoresc. Meas. I*. Vol. 5. Springer Berlin Heidelberg, 2008, pp. 101–145.

[21] Andres F. Olea et al. “Solvent effects on the photophysical properties of 9,10-dicyanoanthracene”. In: *Phys. Chem. Chem. Phys.* 4.2 (2002), pp. 161–167.

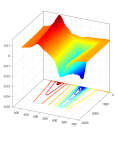

[22] A. K. Gupta, Sekhar Basu, and K. K. Rohatgi-Mukherjee. “Substituent positional effect on radiative lifetimes of anthracene sulphonates”. In: *Can. J. Chem.* 58.10 (1980), pp. 1046–1050.

[23] J. F. Ireland and P. A.H. Wyatt. “Acid-Base Properties of Electronically Excited States of Organic Molecules”. In: *Adv. Phys. Org. Chem.* 12.C (1976), pp. 131–221.

[24] Bernhard Lang et al. “Broadband ultraviolet-visible transient absorption spectroscopy in the nanosecond to microsecond time domain with sub-nanosecond time resolution”. In: *Rev. Sci. Instrum.* 84.7 (2013).

[25] Victor Gray et al. “Photophysical characterization of the 9,10-disubstituted anthracene chromophore and its applications in triplet-triplet annihilation photon upconversion”. In: *J. Mater. Chem. C* 3.42 (2015), pp. 11111–11121.

[26] Carlo Adamo and Vincenzo Barone. “Inexpensive and accurate predictions of optical excitations in transition-metal complexes: The TDDFT/PBE0 route”. In: *Theor. Chem. Acc.* 105.2 (2000), pp. 169–172.

[27] A Becke. “B3LYP”. In: *J. Chem. Phys.* (1993).

[28] Noboru Mataga, Yozo Kaifu, and Masao Koizumi. “Solvent Effects upon Fluorescence Spectra and the Dipolemoments of Excited Molecules”. In: *Bull. Chem. Soc. Jpn.* (1956).

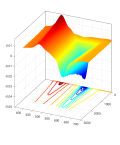

3.4 Quenching Mechanism of Uranyl(VI) by Chloride and Bromide in Aqueous and Non-Aqueous Solution

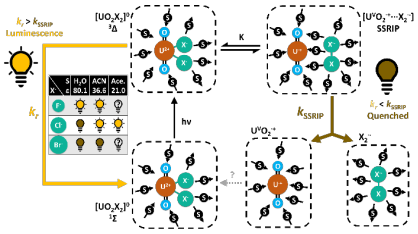

Figure 3.4.1: TOC graphic of "Quenching Mechanism of Uranyl(VI) by Chloride and Bromide in Aqueous and Non-Aqueous Solution".

Haubitz, T., Drobot, B., Tsushima, S., Steudtner, R., Stumpf, T., & Kumke, M. U., Quenching Mechanism of Uranyl(VI) by Chloride and Bromide in Aqueous and Non-Aqueous Solution. *Journal of Physical Chemistry A*,2021*125*(20), 4380–4389.

Personal Contribution:

The here used samples were prepared and provided by the Institute of Resource Ecology (HZDR) of Prof. T. Stumpf by Dr. R. Steudtner. Luminescence and absorption measurements were conducted by Dr. R. Steudtner and Dr. B. Drobot. Quantum mechanical calculations were conducted by Prof. Dr. S. Tsushima. All transient absorption measurements and the large majority of data evaluation, tables, and graphs were done by myself. Furthermore, the large majority of the data interpretation, discussion, and conclusions of the manuscript were done by me. The writing of the manuscript was done in majority by me and in part by Dr. B. Drobot and Prof. Dr. S. Tsushima.

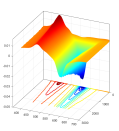

Quenching Mechanism of Uranyl(VI) by Chloride and Bromide in Aqueous and Non-Aqueous Solution

Toni Haubitz[1], Björn Drobot[2], Satoru Tsushima[2,3], Robin Steudtner[2], Thorsten Stumpf[2], and Michael U. Kumke[1*]

[1]University of Potsdam, Institute of Chemistry, Karl-Liebknecht-Str. 24-25, D-14476 Potsdam, Germany

[2]Helmholtz-Zentrum Dresden-Rossendorf, Institute of Resource Ecology, Bautzner Landstraße 400, D-01328 Dresden, Germany

[3]Tokyo Tech World Research Hub Initiative (WRHI), Institute of Innovative Research, Tokyo Institute of Technology, Tokyo, 152-8550, Japan

3.4.1 Abstract

A major hindrance in utilizing uranyl(VI) luminescence as standard analytical tool, for example in environmental monitoring or nuclear industries, is quenching by other ions such as halide ions, which are present in many relevant matrices of uranyl(VI) speciation. Here we demonstrate through a combination of time-resolved laser-induced fluorescence spectroscopy, transient absorption spectroscopy, and quantum chemistry that coordinating solvent molecules play a crucial role in U(VI) halide luminescence quenching. We show that our previously suggested quenching mechanism based on an internal redox reaction of the 1:2-uranyl-halide-complex holds also true for bromide-induced quenching of uranyl(VI). By adopting specific organic solvents, we were able to suppress the separation of the oxidized halide ligand $X_2^{\bullet-}$ and the formed uranyl(V) into fully solvated ions and thereby "reigniting" U(VI) luminescence. Time-dependent density functional theory calculations show that quenching occurs through the outer-sphere complex of U(VI) and halide in water, while the ligand-to-metal charge transfer is strongly reduced in acetonitrile.

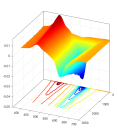

3.4.2 Introduction

Health risk of humans due to exposure to uranium includes radiological as well as chemical toxicity [1]. The average U concentration in drinking water among OECD countries varies between 0.9 ng L^{-1} and 0.4 µg L^{-1}. A small supplier may have a much higher level of U as in the case of a private supplier in Canada who reported U concentration as high as 700 µg L^{-1} [2]. Uranium content in aquifers is of potential health concern and establishment of an in situ measuring technique is indispensable. Time-resolved laser-induced fluorescence spectroscopy (TRLFS) is one of the most promising techniques for such purpose due to its outstanding sensitivity and selectivity [3]. Each U(VI) species exhibits a characteristic luminescence spectrum and a corresponding luminescence decay time allowing spectral deconvolution to get a species distribution from mixed samples. Recently, we demonstrated that U(VI) speciation in a given U(VI) solution of micromolar concentration over a wide pH range can be obtained through a combination of TRLFS and parallel factor analysis (PARAFAC) [4]. This principle can be applied to many environmental-relevant U(VI) systems but is often hindered due to quenching by coexisting matrix compounds. Various organic and inorganic substances are known to quench U(VI) luminescence [5]. For instance, most aqueous U(VI) complexes with carbonate and chloride are non-luminescent or only minimal luminescent at room temperature [6, 7]. Carbonate and chloride are both environmentally abundant and quenching by these ions is consequently a critical problem for the determination of U(VI) speciation in the real-world samples. The mechanism of U(VI) luminescence quenching has been intensively studied both experimentally and theoretically [5, 7, 8, 9, 10, 11, 12, 13]. Whereas experimental studies focused primarily on dynamic quenching, theoretical calculations were performed exclusively on static quenching in $[UO_2X]^+$ ($X = Cl^-, Br^-, I^-$). This gap will be addressed in the present investigation. We found that U(VI) luminescence quenching by halide ions is getting suppressed when solvent water is replaced by acetonitrile (ACN) or acetone (Ace.). This motivated us to revise our previous model on the mechanism of chloride-induced quenching of U(VI) emission [13]. Here, we investigate the influence of chloride and bromide in aqueous solution in a large concentration range of 0 – 1 M and 0 – 0.1 M, respectively, and discuss

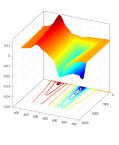

differences found for uranyl(VI) with chloride in ACN solution.

3.4.3 Experimental Section

A uranyl(VI) stock solution was prepared by dissolving solid UO_3 in $HClO_4$. The final uranyl(VI) concentration in each sample for transient absorption measurement was set to be (0.098 ± 0.001) M (checked by ICP-MS) to receive a maximum signal with a low degree of self-quenching. The pH values were measured by a double junction pH electrode Profitrode 125 mm from Merck with a 3 M $NaClO_4$ solution as a bridge electrolyte, to avoid chloride contamination by the electrode. For dilution, deionized water was used and was generated by a Milli-Q Reference Water Purification System of Merck Millipore to 18.2 MΩ. All measurements were performed at room temperature (T = 295 K) if not stated otherwise. As background electrolyte, 1 M perchloric acid was chosen in all samples. To adjust the ligand concentrations, for chloride samples, 1 M hydrochloric acid, while for the bromide sample, 1 M sodium bromide solutions were used as complexation agents that replaced the background electrolyte accordingly. This procedure results in samples with a pH of about 0 if not stated otherwise. However, for higher concentrated bromide samples, the pH might be slightly higher. In the highest concentrated bromide sample of 0.1 M NaBr, nine parts of the solution were 1 M perchloric acid and one part was 1 M NaBr solution. This equates to a maximum ΔpH of about 0.05. For measurements in ACN, LiBr and LiCl were used. TRLFS measurements were conducted with a quadrupled Nd:YAG Laser (Minilite, Continuum) at 266 nm using a 0.3 mJ per 5 ns pulse. For detection a iHR550 spectrograph and an iCCD camera (Horiba Jobin Yvon, 100 lines/mm grid) with a spectral resolution of 0.2 nm were used. UV/Vis measurements were performed on a CARY 5G spectrometer (Varian) with a spectral resolution of 0.1 nm or 1 nm. In both cases, the samples were measured in 4 mL quartz cuvettes with a 1 cm pathway (Hellma Analytics). Photoluminescence measurements were performed on a QuantaMaster 40 spectrofluorometer (PTI, now Horiba) equipped with a 75 W xenon arc lamp. Excitation and emission wavelengths were chosen by corresponding motorized monochromators with a bandwidth of 10 nm and 2 nm, respectively. Spectra were recorded by scanning emission with 1

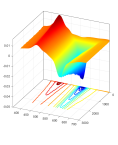

nm resolution and an integration time of 1 s. Temperature constants was achieved via a temperature controllable cuvette holder (TC125 Temperature Control, Quantum Northwest). The PARAFAC algorithm [14], implemented in the optimization toolbox of MATLAB 2017 (MathWorks) [15], was utilized to deconvolute the spectra and time traces into the single contained species. A numerical approach has been chosen to fit a kinetic model to the deconvoluted time traces, in which the corresponding ordinary differential equations (ODEs) of the model were solved by the ODE45 algorithm in Matlab 2017 (MathWorks). The rate constants k of the rate equations were varied to achieve a least square minimum between the numeric model and the experimental time traces by the fmincon algorithm. Quantum chemical calculations were performed using the Gaussian 09 program employing the density functional theory (DFT) by using a conductor-like polarizable continuum model in ACN ($\varepsilon = 36.64$) as previously described [4]. Structure optimizations were performed at the B3LYP level followed by vibrational frequency analysis at the same level to confirm no imaginary frequencies are present. For the calculations of the lowest-lying triplet states two approaches were taken. First, single configuration DFT was used and spin multiplicity of molecules was set to triplet and the lowest-lying state structure was achieved. Second, non-equilibrium time-dependent DFT (TD-DFT) calculations were applied to obtain lowest-lying triplet state structures. For the calculations of emission energy from the triplet excited state to the ground state, state-specific non-equilibrium solvation calculations have been performed. The energy-consistent small-core effective core potential and the corresponding basis set suggested by Küchle et al. [16] were used for uranium. The most diffuse basis functions on uranium with the exponent 0.005 (all s, p, d, and f type functions) were omitted. For chlorine, oxygen, and hydrogen, the valence triple-zeta plus polarization basis was used. The spin-orbit effects and basis set superposition error corrections were neglected. Transient absorption spectroscopy (TAS) measurements were conducted with a Titan-Sapphire-laser system Spitfire Ace PA (Spectra-Physics) as the light source ($\lambda = 800$ nm, pulse length of approximately 100 fs, repetition rate of 1 kHz). The fundamental laser beam is split into a pump and a probe beam. The pump beam wavelength was adjusted using a HE-TOPAS (Light Conversion) parametric amplifier. Unless stated otherwise, a pump

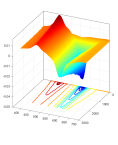

wavelength of λ_{pump} = 310 nm (bandwidth $\Delta\lambda$ approx. 40 nm) was chosen, as uranyl(VI) complexes studied here can be excited in this range. Both beams were coupled into the transient absorption spectrometer (Newport). The probe beam is sent over a variable optical delay line, adjustable between 0 m and 2.4 m delay path length, which corresponds to a maximum time delay between λ_{pump} and λ_{probe} of Δt = 8 ns with a maximum time resolution of 26.6 fs. For white light generation the probe beam was coupled into a CaF_2 crystal to create a white light continuum of 350 nm < λ_{probe} < 700 nm. The transient signal (ΔOD) was calculated based on the logarithmic ratio between the white light intensity with and without a pump beam by the controller software (TAS software Newport, version 2.1). The pump power in the sample was adjusted by a neutral density filter and the resulting pump power was measured by a PEPS-3-9.5 sensor and a 1918-R power meter (Newport) prior to and after each measurement. 2 mm quartz cuvettes from Starna GmbH(Typ 21) were used for measurements and were rigorously stirred during the measurements (Electronic Stirrer Model 300, Rank Brothers Ltd.).

3.4.4 Results and Discussion

Uranyl(VI) with Halides in Aqueous Solution

Figure 3.4.2(left) shows the PARAFAC results of experimental UV/Vis data of the uranyl(VI) absorption in 0.01 M concentration at pH □ 0 and I = 1 M ($HClO_4$). As can be seen, the PARAFAC deconvolution algorithm was able to extract two distinct species of uranyl(VI) for each of the raw data sets with chloride and bromide as a ligand. As the absorption spectra for the free and complexed uranyl(VI) species are very similar in shape, especially for the bromide sample, the main information source for the deconvolution of the two species was the increase in absorption upon addition of ligand, as the complexed species have a significantly higher extinction coefficient (at least 20% higher). The corresponding concentration distribution for both of these species can be seen in Figure 3.4.2(Center). We can identify one of these species (present in both samples at 0 M ligand concentration) as the free uranyl(VI) aquo ion [17]. With increasing ligand concentration the aquo ion is steadily replaced by the second uranyl(VI) species. It can easily be argued that this is the first uranyl(VI)-halide complex

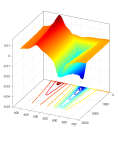

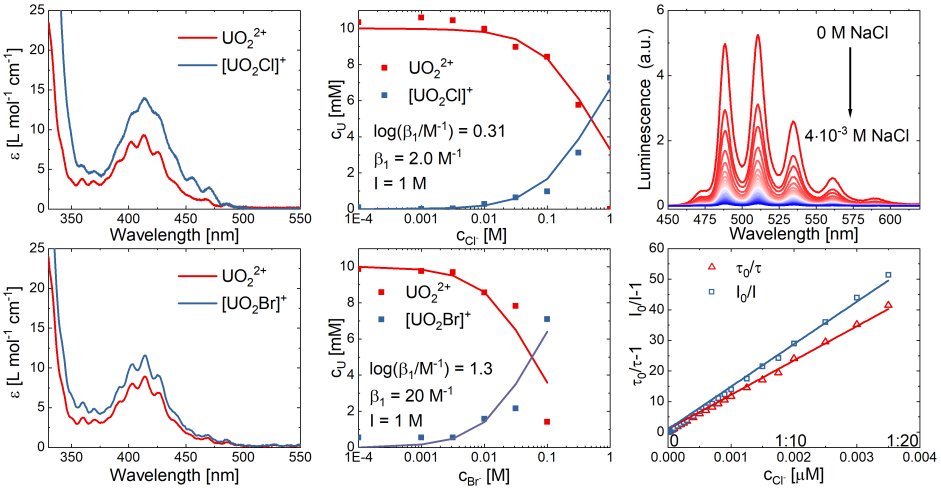

Figure 3.4.2: Spectroscopic results of the investigated samples. Left: PARAFAC deconvoluted UV/Vis data of the free uranyl(VI) and the first chloride complex (top) and the first bromide complex (bottom). Center: PARAFAC deconvoluted speciation plot with fitted complex stability constants and extinction coefficients from UV/Vis data of the free uranyl(VI) and the first chloride complex (top) and the first bromide complex (bottom). Right: U(VI) luminescence spectra with increasing NaCl concentration (top) and its Stern–Volmer plot (bottom). Experimental conditions: UV/Vis: c_U = 0.01 M, c_{Cl} = 0 – 1 M, c_{Br} = 0 – 0.1 M, pH ≈ 0, I = 1 M ($HClO_4$). Luminescence: pH 2, U(VI) $2{\cdot}10^{-5}$ M, $0 \leq Cl^-/UO_2^{2+} \leq 20$, and 0.1 M $NaClO_4$.

$[UO_2X]^+$, respectively. By fitting the PARAFAC normalized speciation data by least-square parameter optimization (fmincon, MATLAB) of symbolically solved complex equilibria (symbolic toolbox, MATLAB), we received fitted extinction coefficients ε and complex stability constants β_1 for both ligand samples. We can see that for the first complex stability constant β_1, chloride ions form a 10 times weaker complex than with bromide, 2.0 M^{-1} (Soderholm/NEA-Database [18]: 1.5 m^{-1} at I = 5.3 m^{-1}) compared to 20 M^{-1} (Razik [19]: 65 m^{-1} at I = 0.05 M^{-1}), respectively.

Figure 3.4.2(right) shows the evolution of U(VI) emission in aqueous solution at pH 2 (no hydrolysis present at pH < 3 [20]) with increasing NaCl concentration ($0 \leq Cl^-/UO_2^{2+} \leq 20$). Species distribution changes from $[UO_2(H_2O)_5]^{2+}$ (aquo ion) to uranyl(VI)-chloro complexes with increasing chloride concentration. The non-linearity of the Stern–Volmer intensity plot as well as the smaller slope of the lifetime plot indicate a combination of dynamic quenching (via UO_2^{2+}(aq)-Cl^- ion pair) and minor contribution of static quenching ($[UO_2Cl]^+$). In comparison to this at pH 8 (where uranyl(VI)-chloro complexes are absent in high saline solutions [21] and where the stronger polynu-

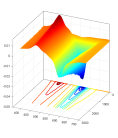

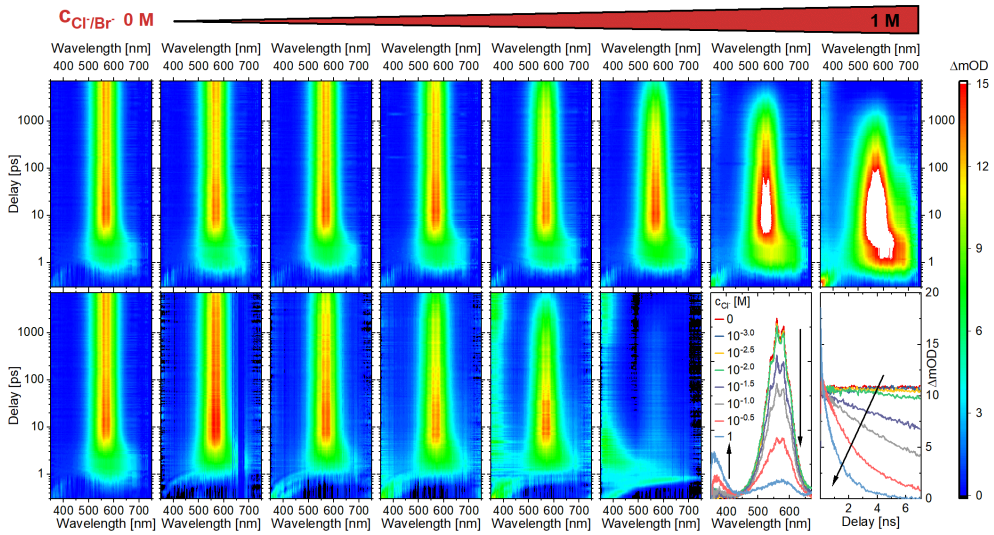

Figure 3.4.3: Transient absorption spectra of uranyl(VI) solutions at eight different chloride concentrations (top row) and six different bromide concentrations (bottom row, left). Bottom right: Transient Spectra (at 7 ns delay) and time traces (at 550 nm) of the chloride samples. c_U = 0.01 M, c_{Cl} = 0 – 1 M, c_{Br} = 0 – 0.1 M, pH ≈ 0, I = 1 M, λ_{exc} = 310 nm, E_{pulse} = 4 μJ, τ_{IRF} = 100 fs.

clear uranyl(VI)-hydroxo species predominate the Stern–Volmer plot) the uranyl(VI) luminescence shows different features (Figure A.2.1). With increasing NaCl concentration both intensity and lifetime plots show slopes close to zero indicating complete absence of dynamic and static quenching. While prevention of static quenching is obvious because of lack of uranyl(VI)-chloro species (which are displaced by the stronger hydroxo complexes due to the higher pH), absence of dynamic quenching can be attributed to less probable ion-pair formation between negatively charged hydroxo uranyl(VI) species (stoichiometry $(OH^-)/(UO_2^{2+}) > 2$) and negatively charged chloride ions. In comparison, for the case of the positively charged UO_2^{2+} aquo ion association with Cl^- is possible as demonstrated by molecular dynamics (MD) simulations [22] thereby contributing to dynamic quenching.

In Figure 3.4.3 one can see the transient absorption spectra at pH □ o with increasing chloride concentration. As one can see in the free uranyl(VI) spectrum (o M chloride), the TA spectroscopy of uranyl(VI) is determined by two major features: After excitation by UV radiation a broad absorption appears, which we previously assigned as the absorption from the $^3\Phi$ into the $^3\Gamma$ state of the uranyl(VI) [23]. A few picoseconds later the signal is replaced via internal conversion by an absorption spectrum

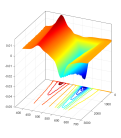

with a defined vibronic structure, which is blue shifted in comparison to the absorption from the $^3\Phi$ state. This absorption was previously assigned to the absorption due to a transition from the $^3\Delta$ state into the $^3\Pi$ state of the uranyl(VI) and is the energetically lowest excited state from which the uranyl(VI) luminescence with several microsecond lifetime occurs. After initial population of the $^3\Delta$ state, this state remains populated within the time window accessible by the TAS setup used (observable time window of the TAS is about 7 ns). This is because with a lifetime of several microseconds only a minimal fraction of molecules return to the ground state within the observation window. With increasing halide concentrations, we can gradually see the acceleration of the depopulation of this state, corresponding to the quenching of luminescence by halide ions. This is true for both investigated halide ions (bromide and chloride). Furthermore, it is visible that at high chloride concentrations, not only the lifetime becomes considerably shorter (below 1 ns) but also that more spectral features appear in the TA spectrum (see Figure 3.4.3). These are even broader and more red-shifted than the ones observed for the free uranyl(VI)'s $^3\Phi$ state, but also have a longer lifetime and a stronger absorption than in the $^3\Delta$ state. These additional features can be assigned to (1) the complex formation of $[UO_2Cl]^+$ and (2) the formation of photoproducts.

At 1 M concentration it is visible, that at 360 nm and after 20 ps a signal starts to evolve, which we assigned to the formation of the dichloride radical $Cl_2^{\cdot-}$. This radical forms, when the excited $[UO_2Cl]^+$ complex collides with an additional chloride ion and the chloride is being oxidized by the excited uranyl(VI) (electrochemical potential of excited uranyl(VI) about +2.61 V [24], comparable to elemental fluorine). This process is the origin for the uranyl(VI)'s phosphorescence typical dynamic quenching character in the presence of chlorides. The previously determined mechanism for this is that the collision forms the excited $[UO_2Cl_2]^0$ complex, which immediately undergoes a redox reaction, where a ligand to metal electron transfer occurs. After this charge transfer, the transient species $U(V)O_2^+$-$Cl_2^{\cdot-}$ radical complex is present, which is shortly after separating into two fully solvated separate ions of $U(V)O_2^+$ and $Cl_2^{\cdot-}$. This separation is then the actual quenching mechanism of the excited state. As both molecules are present in their fully separated solvated ground state, the transient ab-

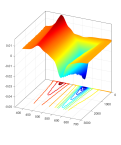

sorption spectra represent their ground state absorption spectra. It is well known that $U(V)O_2^+$ is not stable in aqueous solution and will disproportionate into uranyl(VI) and uranium(IV) within a few milliseconds under our sample conditions [25]. However, any forming uranium(IV) and uranyl(V) are not long-term stable under aerobic conditions and will be at some point reoxidized by $Cl_2^{\bullet-}$, its products, or solvated oxygen to uranyl(VI) due to its higher electrochemical potential, completing the cycle with the sample being practically unchanged and the luminescence quenched.

Bromide shows a very similar luminescence quenching behavior in comparison to chloride in water (Figure A.2.2). To control the postulated mechanism to also apply to the uranyl(VI)-bromide-system and to separate the raw data into single component spectra and their respective temporal behavior, all spectra were globally analyzed and deconvoluted by a PARAFAC analysis. As dimensions for the deconvolution tensor we used the wavelength, delay time, and excitation energy (two different energies were used for the collection of the TA spectra). As the temporal behavior changes from sample to sample for each component (which is not covered by the PARAFAC model), we combined all time traces into one "stacked" time trace. This means the time vector had a length of not only 681 datapoints (one complete TA spectrum with 681 different delay steps) but also 681 x 8 x 3 (data points x samples x scans per sample). The full tensor has then the dimension energies x delay x wavelength. The fit was done under non-negative constraints on all three dimensions, until good enough starting values were found to loosen the constraint on the time domain (noise around ΔOD=0 is typical for TAS). From this deconvolution we recovered five different species for the chloride samples and three different species for the bromide samples. Next to the four found in our previous publication, we were able to separate the $^3\Delta$ state of the free and the complexes from one another. This was made possible based on the additional data points for intermediate halide concentrations. For the bromide samples however, as the 1:0- and 1:1-complexes are spectrally very similar in luminescence [26], it can be assumed that their transient spectra are also very similar and are difficult to be separated spectrally due to the broad character of transient absorptions. Additionally, their temporal behavior is coupled via the complexation equilibrium, which makes them both appear as one component in a PARAFAC

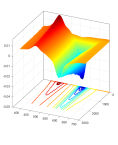

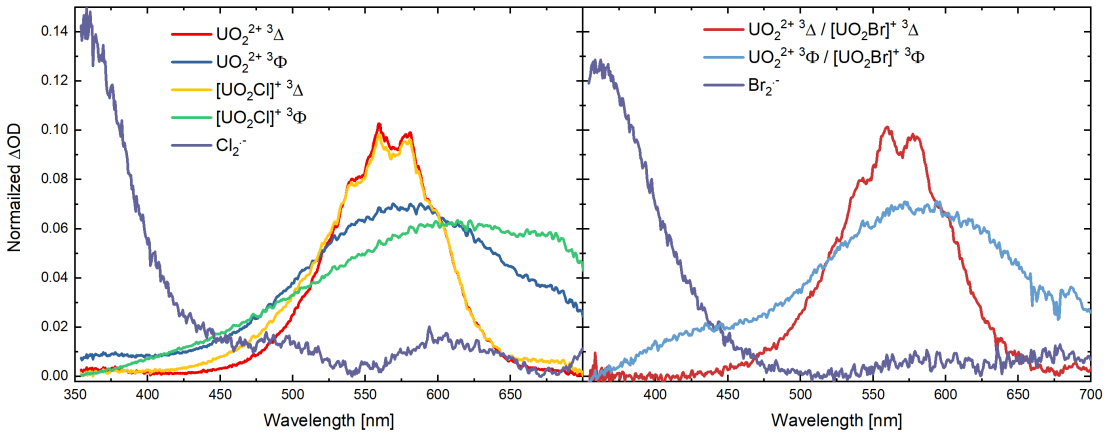

Figure 3.4.4: PARAFAC deconvoluted spectra of uranyl(VI) species in chloride (left) and bromide (right) samples. For bromide PARAFAC was able to differentiate the different states, but not the different complexes. c_U = 0.01 M, c_{Cl} = 0 – 1 M, c_{Br} = 0 – 0.1 M, pH ≈ 0, I = 1 M.

deconvolution and leading to a reduced number of components observable in the bromide samples.

As can be seen in Figure 3.4.4, the spectra of the free uranyl(VI) and its complexes are very similar, in energy as well as in shape. However, the bromide complex signals are slightly red shifted ((0.7 ± 0.2) nm) compared to the chloride signals. The energetic structure of the transient absorption represents the vibronic pattern of the absorption, meaning, that absorptions not only are conducted into the lowest vibronic state of the electronically excited state, but also into higher vibronic states as well. This means, that the energetic difference in the vibronic pattern represents the vibrational energies of the molecule, for example, the symmetric or antisymmetric stretch vibration, of the $^3\Pi$ state.

The dihalide radical signals fit well with the literature data, where the maximum of the dichloride radical of 340 nm [27] is not detectable by the transient spectrometer (lower limit 350 nm) and the maximum of the dibromide radical is found to be 361 nm (Lit. 360 nm [27]).

Furthermore no uranium(IV) or uranyl(V) transients were detected, which might be due to a mismatch in excitation wavelength, low extinction coefficient at the excitation wavelength of the ground state, low concentration, and/or low extinction coefficients in the observed spectral window of the excited states of these ions.

The deconvoluted time traces (Figures A.2.3 and A.2.4) give insights on how the involved electronic

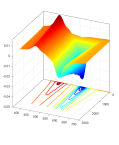

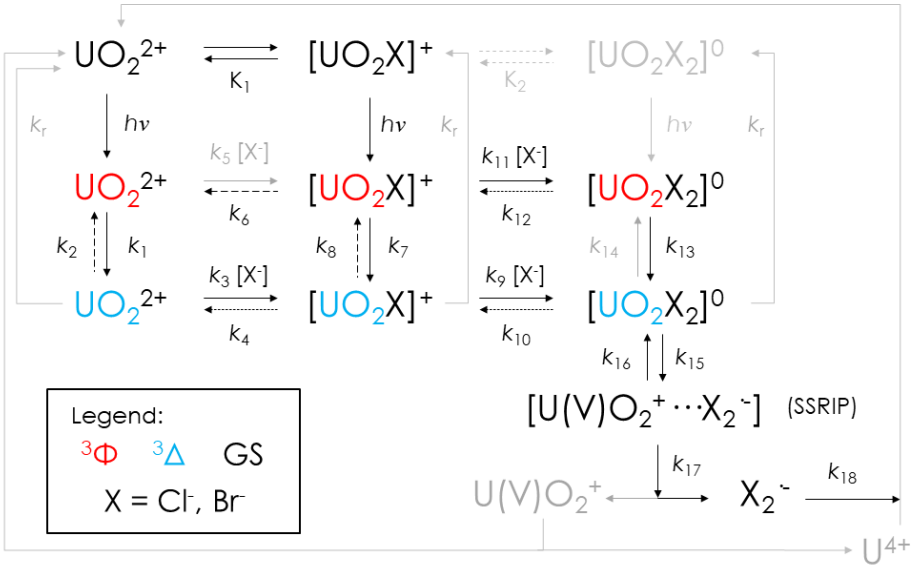

Figure 3.4.5: Kinetic scheme of possible excitation, complexation, internal conversion, and redox pathways. Lines depicted in gray: not utilized for kinetic modelling; dashed lines: kinetic pathways only relevant for chloride kinetic modeling; pointed lines: Kinetic pathways only relevant for bromide kinetic modeling. $k_{17} \approx 0$ in frozen or low dielectric solvents.

states and species are interconnected. A general mechanistic scheme based on our previous findings [23] can be seen in Figure 3.4.5: While the three electronic states of each complex ($^1\Sigma$ ground state, $^3\Phi$ and $^3\Delta$ excited states) are coupled via excitation, internal conversion, and intersystem crossing processes from electron orbital transitions, the complexes themselves are coupled via halide addition or abstraction kinetics, that is, complexation. Not all depicted kinetic rates are relevant and/or necessary for a full description of the deconvoluted time profiles (overparameterization). For example, certain diffusion limited processes/pathways (like the equilibration of the first excited complex by k_5) are usually much slower than certain electronic processes (internal conversion, vibrational relaxation) and can therefore not compete with the faster processes. Also, depending on the halide (hard/soft character, size, properties), certain complex formation equilibria can be or cannot be observed in the measured concentration range. Furthermore, the luminescence rates k_r will not be observed by the transient absorption spectrometer, as being far too slow ($k_r < 0.01\ ns^{-1}$) and thus being outside of the detection range of the instrument. These irrelevant rates were set to zero in the ODE solver and thus ignored in

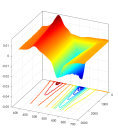

Table 3.4.1: Most Important Fitted Kinetic Rates k. Ground state complex stability constants β from UV/Vis data. Complete fitted data can be found in Table A.2.1. c_U = 0.01 M, c_{Cl} = 0 – 1 M, c_{Br} = 0 – 0.1 M, pH ≈ 0, I = 1 M.

	Cl^-	Br^-	Unit
β_1	2.0	20	$[M^{-1}]$
k_1	210	400	$[ns^{-1}]$
k_3	45	60	$[ns^{-1}M^{-1}]$
k_4	6.0	< 0.01	$[ns^{-1}]$
k_9	12	22	$[ns^{-1}M^{-1}]$
k_{10}	< 0.01	410	$[ns^{-1}]$
k_7	1.0	12	$[ns^{-1}]$
k_{13}	14	410	$[ns^{-1}]$
k_{15}	110	580	$[ns^{-1}]$
k_{16}	15	5.4	$[ns^{-1}]$
k_{17}	2.2	2.9	$[ns^{-1}]$
k_{18}	0.07	0.08	$[ns^{-1}]$

the numerical fitting.

The kinetic fitting of the model to the data was conducted by numerically solving the ODE of the model (see eq. A.1 to A.9 for differential equations) and then least square fitting of the involved rates k and relative extinction coefficients of the states (fmincon, MATLAB) to the generated time profiles by the ODE solver (ODE45, MATLAB). Ground state uranyl- and complex-concentrations were fully modeled in terms of the fitted complex stability constant β_1 (UV/Vis data, vide supra), as a simple one step complexation gives an analytically solvable law of mass action. Relative extinction coefficients were treated relative to uranyl(VI) ground state absorption (setting ε equal to 1 L mol^{-1} cm^{-1}) for each state and species to account for different absorption intensities.

The most important rates and ground state complex stability constants can be found in Table 3.4.1. From the fitted rates, we derive complex stability constants K_{ex} for the energetically lowest and luminescent excited states ($^3\Delta$) by taking the ratio of the formation rate and the dissociation rate ($K_{ex1} = k_3/k_4$, $K_{ex2} = k_9/k_{10}$, respectively). For the chloride ions these are low, $K_{ex1}(Cl^-)$ = 7.5 M^{-1} and $K_{ex2}(Cl^-)$ > 120 M^{-1} ($\lg(\beta_{ex1}(Cl^-)/M^{-1})$ = 0.88 and $\lg(\beta_{ex2}(Cl^-)/M^{-1})$ = 3.0) and for the bromide system $K_{ex1}(Br^-)$ > 6000 M^{-1} and $K_{ex2}(Br^-)$ = 0.056 M^{-1} ($\lg(\beta_{ex1}(Br^-)/M^{-1})$ > 3.7 and

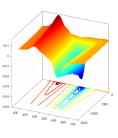

$\lg(\beta_{ex2}(Br^-)/M^{-1}) = 2.5$). It can be seen that both complex stability constants for both ions are, for some even several orders of magnitude, higher than for their ground state equivalents, meaning the excited state complexes are more stable (clearly visible already in raw data in Figure 3.4.3). This can be due to the elongation of one of the yl-oxygen bonds by excitation (Table 3.4.2) and thus an increased space in the equatorial plane, which leads to a closer approach of the uranium and halide ion and a better orbital overlap.

While there are large differences in complex stability constants, the photochemical and quenching behavior for chloride and bromide are quite similar (k_{15--18}). Previously, we were not able to differentiate between the association step of the second chloride ion and the redox step [23]. We can now clearly conclude from our kinetic data, that at first the second stage complex forms, which then undergoes the actual redox step to uranyl(V) and the dihalide radical $X_2^{\cdot -}$. This redox step is very rapid in comparison to the complex formation rate ($k_{15} \gg k_9$), but via a return reaction (k_{16}), a stable equilibrium between the oxidized form (radical ion pair) and the $^3\Delta$ state of the $[UO_2Cl_2]^\circ$ forms, which lies strongly on the side of the oxidized form ($k_{15} > k_{16}$). After this equilibrium is established, the radical ion pair complex of UO_2^+ and $X_2^{\cdot -}$ will separate into their respective fully separated and solvated ions and no luminescent $^3\Delta$ state is accessible again ($k_r \ll k_{17} = 2.2$ and $2.9\ ns^{-1}$, respectively). As this "separation" rate is the slowest in the whole process, it can be considered as the dominant rate competing with k_r and can be compared to the macroscopically observable quenching rate k_q in luminescence spectroscopy. Indeed, literature values for $k_q(Cl^-) = 1.9\ ns^{-1}$ and $k_q(Br^-) = 4.8\ ns^{-1}$ (ref. [8]) agree very well with the here observed rates for k_{17}.

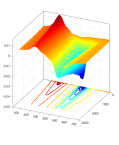

Table 3.4.2: Major Bond Distances (in Å) in Singlet Ground State (S_0) and Lowest-Lying Triplet State (T_1) of U(VI) Aquo, Chloro-Aquo, and Chloro-ACN Complexes and Emission Energy (in eV) from T_1 to S_0 as Obtained by DFT and TD-DFT Calculations.

Complex	sym.	Ground state				Lowest triplet					ref.
			U-O_{ax}	U-O_w	U-Cl		U-O_{ax}	U-O_w	U-Cl	emiss.	
$[UO_2(H_2O)_5]^{2+}$	D_{5h}		1.750	2.462	–		1.796	2.469	–	2.421	[23]
$[UO_2Cl(H_2O)_4]^{+}$	C_{2v}	$^1A_1$	1.758	2.505	2.674	$^3B_2$	1.798	2.560	4.488	0.759	[23]
$[UO_2Cl_2(H_2O)_3]^{0}$	C_{2v}	$^1A_1$	1.763	2.524	2.731	$^3B_2$	1.794	2.553	3.107	1.385	[23]
$[UO_2Cl(CH_3CN)_4]^{+}$	C_{2v}	$^1A_1$	1.758	–	2.656	$^3A_1$	1.791	–	2.717	2.320	this work
$[UO_2Cl_2(CH_3CN)_3]^{0}$	C_{2v}	$^1A_1$	1.764	–	2.711	$^3A_1$	1.797	–	2.745	2.360	this work

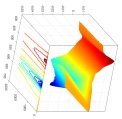

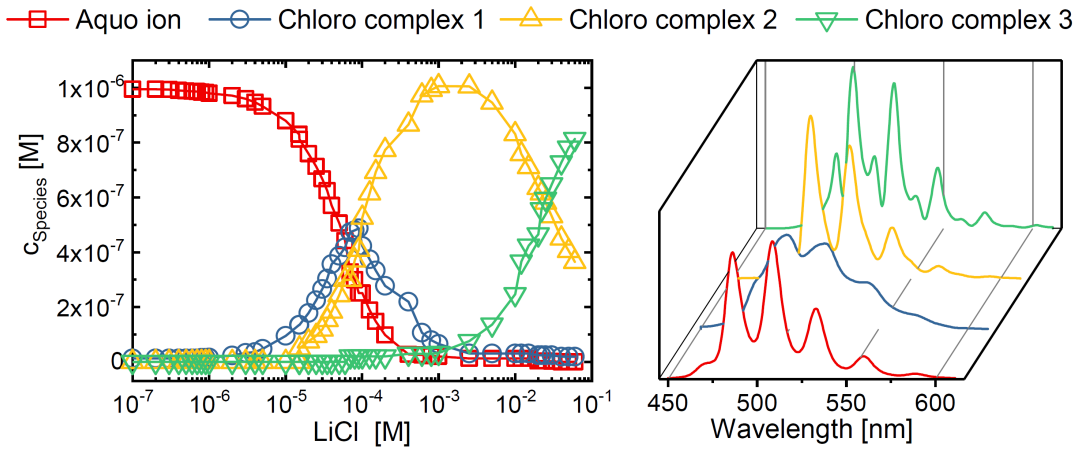

Figure 3.4.6: U(VI) species distribution with increasing LiCl concentration (left) and extracted luminescence spectra for the five independent species (right) in U(VI)-Cl-CH_3CN system. U(VI) 10^{-6} M and $HClO_4$ 10^{-2} M.

This quenching mechanism, based on 1:2 complex formation and reduction, further explains the fact, that luminescence in cryogenically frozen samples by all complexes is possible [28], as the diffusion controlled dissociation step is suppressed in a frozen matrix (k_{17} = 0 ns^{-1}) and the equilibrium between the radical ion pair and the second stage complex (k_{15}/k_{16}) opens the possibility of a radiative deactivation pathway through the second stage complex, in other words luminescence. Furthermore, it explains the complete absence of dynamic quenching in higher pH ranges (vide supra, Figure A.2.1), as the stronger hydroxo complexes prevent any formation of the 1:2-chloro complex.

Uranyl(VI) with Halides in Non-Aqueous Solution

Although the quenching mechanisms discussed above do not indicate any active role of solvent molecules, it is well-known that reaction pathways including radical ion pairs are strongly affected by the solvent [29]. Therefore, we selected ACN as alternative solvent for uranyl(VI) chloride luminescence studies in an attempt to manipulate excitation and deexcitation schemes. In addition to its physico-chemical properties (miscible with water, certain solubility of salts), this system is useful since the U(VI)-Cl-CH_3CN system was extensively studied experimentally and theoretically [30, 31, 32, 33]. We measured the luminescence spectra of the U(VI)-chloride-ACN system. The well-known luminescence spectrum of the uranyl(VI) aquo ion was observed in the U(VI)-ACN system in the absence of

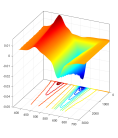

Cl^- as well, but with a remarkable long lifetime of 30 μs (compared to 1 – 4 μs in water [4]). Addition of Cl^- (as LiCl) to ACN solutions did not affect the luminescence lifetime of the uranyl(VI) ion. By increasing the Cl^- concentration up to 0.1 M and using PARAFAC, four additional complexes were found (Figure 3.4.6, left) which correspond to a step-wise coordination of chloride to uranyl(VI). The luminescence spectrum of each species was obtained by spectral deconvolution (Figure 3.4.6, right). It was thus found that in the ACN system, the uranyl(VI)-chloro species are luminescent.

Previous works showed that as the Cl^- concentration increases coordinating waters are co-substituted by chloride and ACN although the exact number of coordinating water and ACN remains somewhat ambiguous. Four chloro complexes in Figure 3.4.6 presumably correspond to the complexes with stepwise increase of chloride coordination from one to four. For DFT modeling, for the sake of simplicity we used $[UO_2Cl_n(CH_3CN)_{5-n}]^{2-n}$ (n = 1 and 2, Figure 3.4.7). Deexcitation energies from T_1 to S_0 in $[UO_2Cl(CH_3CN)_4]^+$ and $[UO_2Cl_2(CH_3CN)_3]^0$ are 2.320 and 2.360 eV, respectively, which is close to 2.421 eV in $[UO_2(H_2O)_5]^{2+}$ (Table 3.4.2). This corroborates the experimental results that chloride is capable of quenching U(VI) luminescence in water but not in ACN. When we examine MOs near the HOMO in U(VI)-chloride-ACN complexes, we find C 2p AOs are merged into HOMOs whereas contribution of Cl AOs to HOMOs is clearly reduced. Thus in U(VI)-chloride-ACN complexes there is much reduced chloride-to-uranium charge transfer in its lowest triplet state. This indicates that other organic solvents containing carbon may have a similar trend as ACN. We tested this hypothesis using acetone and found that uranyl(VI) chloride luminescence quenching indeed does not occur in acetone (Figure A.2.5). We thereby support our initial hypothesis that uranyl(VI) luminescence quenching is a solvent specific phenomenon and water can be regarded as rather peculiar solvent in this respect.

Because uranyl(VI) luminescence quenching by halides gets more pronounced as the atomic number of halide increases, quenching may be again observed in the uranyl(VI)-bromide-ACN system. We studied this point experimentally and theoretically. Figure A.2.2 shows the Stern–Volmer plot of uranyl(VI) luminescence lifetime and intensity with increasing Br^- concentration for the water as

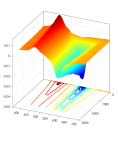

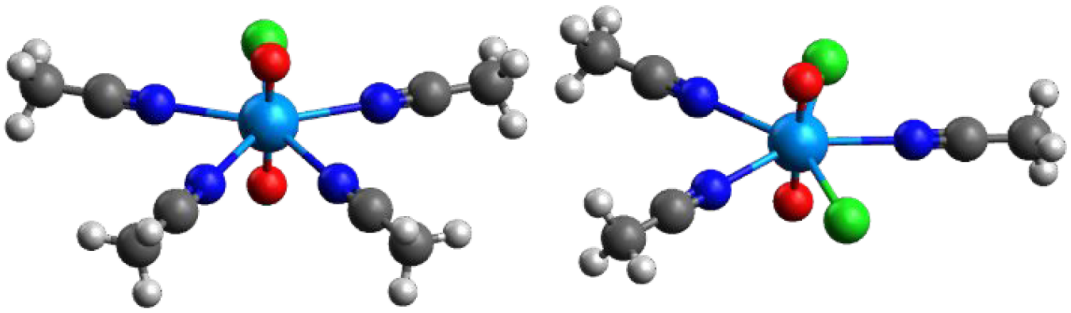

Figure 3.4.7: DFT optimized structures of two uranyl(VI) chloro-ACN complexes $[UO_2Cl(CH_3CN)_4]^+$ (left) and $[UO_2Cl_2(CH_3CN)_3]^0$ (right). Uranium: light blue, oxygen: red, chlorine: green, nitrogen: dark blue, carbon: dark gray, hydrogen: white.

well as ACN system. Obviously and in contrast to Cl^-, quenching occurs for both solvents. The spin density $\alpha - \beta$ of T_1 of uranyl(VI) bromide complexes with water and ACN coordination obtained by TD-DFT calculations are given in Figure A.2.6 which shows bromine-to-uranyl charge transfer upon photoexcitation thereby confirming experimental findings.

It can be seen in Figure 3.4.8 that transient spectra of uranyl(VI) with 1 M Cl^- in ACN are similar to the water samples, with the two excited states $^3\Phi$ and $^3\Delta$, and an additional absorption for a dichloride radical. However, some major differences are apparent. First, from the inset, one can see that the internal conversion between both excited states is dominated by a thermal equilibrium (k_{13} = 650 ns^{-1}/k_{14} = 97 ns^{-1}), as the $^3\Phi$ state never reaches a ΔOD of 0 and stays present for the whole time frame accessible for the TAS setup (7 ns). By taking the ratio of the rates as an occupation ratio (in equilibrium: $N_1/N_0 = k_{14}/k_{13}$), we can calculate via a Boltzmann population at room temperature an energy gap of 407 cm^{-1} between the $^3\Phi$ and $^3\Delta$ states. Second, the lifetime of the luminescent state $^3\Delta$ is longer than the TAS observable delay time, indicating, as expected from the luminescence data, no quenching is present and an emission of luminescence despite 1 M chloride is possible. Third, the spectra of the dichloride radical and the $^3\Delta$ state could not be separated by PARAFAC. This may indicate that the radical ion pair is not separating into different species/components with their own characteristic time profiles. On the other hand, when both ions remain together in a radical ion pair, they both

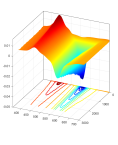

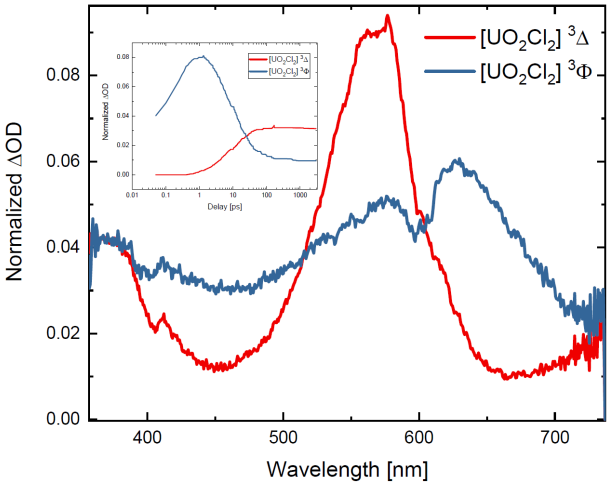

Figure 3.4.8: Deconvolution of the uranyl(VI) sample in ACN. The main graph shows the spectra, the inset shows the time profile of both excited states. Dips in spectra at 590 nm and 390 nm are laser artifacts/residuals from sum frequency generation. c_U = 0.01 M, c_{Cl} = 1 M

follow the same time profile as they remain in equilibrium and are considered by PARAFAC as one component. Furthermore, this equilibrium supports the findings of the TD-DFT calculations, as a stable equilibrium between the oxidized and reduced form indicates a weaker charge-transfer character in these uranyl(VI)-chloride-complexes.

From these data and the established mechanism, it can be understood why the luminescence of uranyl(VI) in ACN is not quenched by chloride: The radical ion pair of uranyl(V) and the dichloride radical $Cl_2^{\bullet-}$ seem to be stable in ACN and do not break apart into separate ions with their own respective solvent shell and thus the second stage chloride complex can still luminesce similar to the solid solvent cage in frozen uranyl(VI) samples (k_{17} = 0 ps^{-1}).

The reason for the different stability of radical ion pairs in different solvents is explained in literature [34] due to the difference in dielectric constants of the solvents (continuum approach, specific ion/solvent-interactions are ignored), where the lower dielectric constant of ACN (ε = 36.64 [35]) makes the complexes more stable than in the high dielectric water (ε = 80.1 [35]). The dielectric constant is a measure on how well a medium/solvent is isolating/weakening an electric field, the higher the constant the stronger the isolation of electric fields. That means that water is very good in shield-

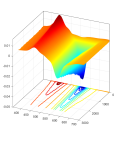

ing the positive charge of the uranyl(V) radical ion from the negative charge of the dichloride radical. Thus, the Coulombic attraction between those ions reduces strongly, thus lowering the stability of the radical ion pair. The lower dielectric constant of ACN on the other hand does not isolate the charges as strongly from one another and the complex remains stable. In literature these radical ion pairs with a shared solvent cage are usually classified as two kind of complexes [34]: Contact radical ion pairs (CRIPs, inner-sphere complex), where the ions stay in direct contact with one another, and solvent-separated radical ion pairs (SSRIPs, outer-sphere complex), where solvent molecules are located between both ions but they still remain a complex with one larger and shared solvation sphere. From the spectra it is visible, that both ions seem to be quantum-mechanically well separated (typical dichloride radical peak visible as if it would be fully solvated), which indicates a somewhat own solvation sphere for each ion in the complex (solvent separated ions). Furthermore, the fact that ACN has a much lower dielectric constant but is still quite high compared to many other solvents (Gould and Farid calculated that SSRIPs dominate in ACN [34]) and our previously found theoretical evidence for an outer-sphere complex formation [23] speak for the radical ion pair existing in a solvent-separated (SSRIP) configuration. We assume that these findings are consistent with the luminescence data in acetone (Figure A.2.5, vide supra), where luminescence is as well present due to the formation of an SSRIP in the low dielectric medium acetone ($\varepsilon = 21.01$) [35].

In the case of bromide in ACN, the luminescence is clearly quenched again (Figure A.2.2), so we assume that the SSRIP is not stable in the case of the bromide complexes. This might be because the dibromide radical ion is a far larger ion with the same amount of charge as the dichloride ion thus it has a lower charge density, higher polarizability, and lower hardness. This means, in return, that the Coulombic attraction between the dibromide radical and the uranyl(V) ion is much lower than in the dichloride radical and makes the SSRIP fall apart even in the lower dielectric medium ACN and the luminescence is being quenched. This would mean that uranyl-bromide in acetone might not be quenched, as the dielectric constant might be low enough to stabilize the weaker Coulombic bond between the ions.

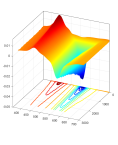

In comparison to chloride and bromide, uranyl(VI) luminescence is not dynamically quenched by fluoride ions. This is true for the uranyl(VI)-fluoride system in water (Figure A.2.7) as well as in ACN (Figure A.2.8, $\tau = (1.70 \pm 0.04)\ \mu s$). For the 1:1 uranyl(VI)-fluoride complex the luminescence lifetime is even strongly increased to $(52 \pm 10)\ \mu s$. This indicates that the higher charge density of the smaller difluoride radical ion leads to a stronger Coulombic attraction within the SSRIP, which is strong enough to stabilize the ion pair even in the highly dielectric water.

3.4.5 Conclusions

In this study, we investigated the validity of our previously proposed quenching mechanism of U(VI)-H_2O-chloride for a larger concentration range of chloride and for bromide as well for the non-aqueous solvent CH_3CN by TAS, luminescence spectroscopy, and theoretical calculations. Since chloride is omnipresent in majority of uranyl(VI) systems, the here presented results are of fundamental interest. Our results show that uranyl(VI) luminescence quenching by halide ions is not a general phenomenon but strongly correlated to equatorial solvent coordination.

For both halides the dominating luminescence quenching mechanism occurs via the formation of the corresponding 1:2-complex $[UO_2X_2]^0$ and subsequent fast redox reaction to uranyl(V) and the corresponding dihalide radical $X_2^{\cdot -}$. We found that this newly formed radical ion pair remains in equilibrium with the 1:2-uranyl-halide complex. The subsequent separation into fully solvated separated ions can be described as the macroscopically observed quenching rate k_q (dynamic component), while the initial formation of the 1:1-complex $[UO_2X]^+$ is the static component of the uranyl(VI) quenching process.

By measurements in non-aqueous media we could further show, that in media with a lower dielectric constant than water, this radical ion pair does not separate into solvated independent ions, but remains in close proximity as an SSRIP (outer-sphere complex). Without this dissociation step in those media, the equilibrium between the SSRIP and the 1:2-uranyl(VI)-halide-complex (re)opens a pathway for uranyl(VI)-complex-luminescence and explains the less quenched behavior in non-aqueous

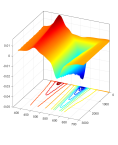

solutions. Furthermore, this dissociation step can also not occur in aqueous media in case of a frozen sample, thus making emission possible.

Thus we have not only explained the two quenching mechanisms but furthermore demonstrated that uranyl(VI) TAS is a useful spectroscopic technique for investigating a variety of chloride-containing uranyl(VI) systems. Furthermore, we can conclude that luminescence measurements with quenching ions in long-term repository research should be conducted under cryogenic conditions, as these do not only suppress the dynamic quenching effects due to reduction but also keep the ground state equilibrium concentration ratios fixed to guarantee measuring only the ground state, and not excited state, equilibrium constants.

3.4.6 Supporting Information

Luminescence data of chloride at pH 8, quenching by bromide in ACN, fit of kinetic model to kinetic data, emission spectra in acetone, spin densities of bromide complexes, and luminescence data with fluoride in water and ACN

3.4.7 Acknowledgement

T.H. and M.U.K. are grateful to the Federal Ministry for Economic Affairs and Energy for the financial support (contract number 02E11415F).

We would like to thank H.D. Burrows for his valuable insights and preliminary measurements on the topic.

3.4.8 Abbreviations

TAS, Transient Absorption Spectroscopy; PARAFAC, Parallel Factor Analysis; TRLFS, Time-resolved Laser-induced Fluorescence Spectroscopy; IC, Inner Conversion; ISC, Inter System Crossing; LMCT, Ligand to Metal Charge Transfer; TD-DFT, Time-dependent Density Functional Theory; NIR, Near Infrared; ACN, Acetonitrile; S, Singlet; T, Triplet; RIP, Radical ion pair; CRIP, Contact radical ion

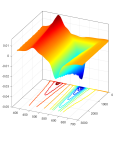

pair; SSRIP, Solvent-separated radical ion pair; ODE, ordinary differential equation; MD, molecular dynamics; Ace., Acetone

References

[1] Stephanie Handley-Sidhu et al. "A review of the environmental corrosion, fate and bioavailability of munitions grade depleted uranium". In: *Sci. Total Environ.* 408.23 (2010), pp. 5690–5700.

[2] "WHO | Uranium in drinking-water". In: *WHO* (2012).

[3] Euo Chang Jung et al. "Uranium determination in groundwater using laser spectroscopy". In: *Rev. Anal. Chem.* 33.4 (2014), pp. 245–254.

[4] Björn Drobot et al. "Combining luminescence spectroscopy, parallel factor analysis and quantum chemistry to reveal metal speciation – a case study of uranyl(VI) hydrolysis". In: *Chem. Sci.* 6 (2015), pp. 964–972.

[5] Hugh D. Burrows et al. "Quenching of the luminescent state of the uranyl ion (UO) by metal ions. Evidence for an electron transfer mechanism". In: *J. Chem. Soc. Faraday Trans. 1 Phys. Chem. Condens. Phases* 72.0 (1976), pp. 163–171.

[6] C. Götz, G. Geipel, and G. Bernhard. "The influence of the temperature on the carbonate complexation of uranium(VI): A spectroscopic study". In: *J. Radioanal. Nucl. Chem.* 287 (2011), pp. 961–969.

[7] Hugh D. Burrows. "Electron transfer from halide ions to uranyl(2+) excited-state ions in aqueous solution: formation and decay of dihalide radical anions". In: *Inorg. Chem.* 29 (1990), pp. 1549–1554.

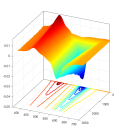

[8] Yu Yokoyama, Masataka Moriyasu, and Shigero Ikeda. “Electron transfer mechanism in quenching of uranyl luminescence by halide ions”. In: *J. Inorg. Nucl. Chem.* 38 (1976), pp. 1329–1333.

[9] Shukichi Sakuraba and Ryoka Matsushima. “Photochemical Reactions of Uranyl Ions with Organic Compounds. IV. The Uranyl Fluorescence Quenching by Aliphatic Alcohols”. In: *Bull. Chem. Soc. Jpn.* 44.11 (1971), pp. 2915–2918.

[10] Masataka Moriyasu, Yu Yokoyama, and Shigero Ikeda. “Quenching mechanisms of uranyl luminescence by metal ions”. In: *J. Inorg. Nucl. Chem.* 39.12 (1977), pp. 2205–2209.

[11] Tomoo Yamamura et al. “New mechanism in deactivation of excited uranyl(VI) ion by lanthanide(III) ions”. In: *Phys. Chem. Chem. Phys.* 1.15 (1999), pp. 3491–3496.

[12] Sebastião J Formosinho et al. “Deactivation processes of the lowest excited state of [UO2(H2O)5]2+ in aqueous solution.” In: *Photochem. Photobiol. Sci.* 2 (2003), pp. 569–575.

[13] Satoru Tsushima, Christian Götz, and Karim Fahmy. “Photoluminescence of uranium(VI): Quenching mechanism and role of uranium(V)”. In: *Chem. - A Eur. J.* 16 (2010), pp. 8029–8033.

[14] Rasmus Bro. “PARAFAC. Tutorial and applications”. In: *Chemom. Intell. Lab. Syst.* 38 (1997), pp. 149–171.

[15] *MATLAB and Optimization Toolbox 2018b*. Natick, Massachusetts, 2019.

[16] W. Küchle et al. “Energy-adjusted pseudopotentials for the actinides. Parameter sets and test calculations for thorium and thorium monoxide”. In: *J. Chem. Phys.* 100 (1994), pp. 7535–7542.

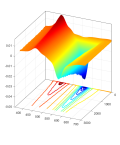

[17] A. A. Migdisov et al. “A spectroscopic study of uranyl speciation in chloride-bearing solutions at temperatures up to 250 °C”. In: *Geochim. Cosmochim. Acta* 222 (2018), pp. 130–145.

[18] L. Soderholm, S. Skanthakumar, and Richard E. Wilson. “Structural Correspondence between Uranyl Chloride Complexes in Solution and Their Stability Constants”. In: *J. Phys. Chem. A* 115 (2011), pp. 4959–4967.

[19] A. Abdel Razik, F. A. Ali, and F. Abu Attia. “Evaluation of the stability constants of uranyl association complexes with chloride, fluoride, bromide, and sulfate anions in solutions of constant ionic strength”. In: *Microchem. J.* 39.3 (1989), pp. 258–264.

[20] Björn Drobot et al. “Speciation Studies of Metals in Trace Concentrations: The Mononuclear Uranyl(VI) Hydroxo Complexes.” eng. In: *Anal. Chem.* 88 (2016), pp. 3548–3555.

[21] C. Hennig et al. “Comparative EXAFS investigation of uranium(VI) and -(IV) aquo chloro complexes in solution using a newly developed spectroelectrochemical cell”. In: *Inorg. Chem.* 44.19 (2005), pp. 6655–6661.

[22] Thanh Nghi Nguyen et al. “Multi-scale modelling of uranyl chloride solutions”. In: *J. Chem. Phys.* 142.2 (2015).

[23] Toni Haubitz et al. “Ultrafast Transient Absorption Spectroscopy of UO22+ and [UO2Cl]+”. In: *J. Phys. Chem. A* (2018).

[24] Minas D. Marcantonatos. “Mechanism of Interactions between Aquo-metallic Complexes and the Photoexcited Aquo-uranyl(VI) Ion”. In: *J. Chem. Soc. Faraday Trans. 1* 75 (1978), pp. 2252–2272.

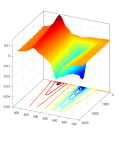

[25] A. Ekstrom. “Kinetics and Mechanism of the Disproportionation of Uranium(V)”. In: *Inorg. Chem.* 13.9 (1974), pp. 2237–2241.

[26] M. Demnitz et al. “Temperature-dependent luminescence spectroscopic investigations of uranyl(vi) complexation with the halides F-and Cl-”. In: *Dalt. Trans.* 49.21 (2020), pp. 7109–7122.

[27] G. C. Hug. “Optical Spectra of Nonmetallic Transient Species in Aqueous Solutions”. In: *Natl. Stand. Ref. Data Ser. NSRDS-NBS69* (1981).

[28] A. Osman and G. Geipel. *Luminescence properties of uranyl ions in chloride media in frozen samples*. Tech. rep. 2012, p. 60.

[29] Hans-Joachim Werner, Hubert Staerk, and Albert Weller. “Solvent, isotope, and magnetic field effects in the geminate recombination of radical ion pairs”. In: *J. Chem. Phys.* 68.5 (1978), pp. 2419–2426.

[30] Christoph Hennig et al. “Species Distribution and Coordination of Uranyl Chloro Complexes in Acetonitrile”. In: *Inorg. Chem.* 47.8 (2008), pp. 2987–2993.

[31] Kelly Servaes et al. “Structure of [UO2Cl4]2- in Acetonitrile”. In: *Inorg. Chem.* 44.22 (2005), pp. 7705–7707.

[32] Michael Bühl et al. “Water versus Acetonitrile Coordination to Uranyl. Density Functional Study of Cooperative Polarization Effects in Solution”. In: *Inorg. Chem.* 50.1 (2011), pp. 299–308.

[33] C Gaillard et al. “Uranyl Coordination in Ionic Liquids: The Competition between Ionic Liquid Anions, Uranyl Counterions, and Cl- Anions Investigated by Extended X-ray Absorption Fine Structure and UV−Visible Spectroscopies and Molecular Dynamics Simulations”. In: *Inorg. Chem.* 46.12 (2007), pp. 4815–4826.

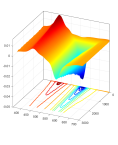

[34] Ian R Gould and Samir Farid. “Dynamics of Bimolecular Photoinduced Electron-Transfer Reactions”. In: *Acc. Chem. Res.* 29.11 (1996), pp. 522–528.

[35] David R. Lide. *CRC Handbook of Chemistry and Physics*. 84th. Boca Raton, FL: CRC Press, 2004, pp. 153–155.

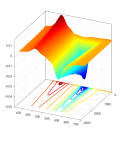

The first principle is that you must not fool yourself – and you are the easiest person to fool.

Richard Feynman

4

Discussion

For a complete photophysical characterization of atoms or molecules, it is necessary to know the energies of their excited states, the temporal development of those states, and to understand the chemical interactions between these states and other present compounds. For a basic understanding of these properties, classical techniques such as linear absorption and laser luminescence spectroscopy are an excellent choice to start with for a simple ground and excited state characterization. However, to fully understand the involved excited state processes, a more sophisticated and more

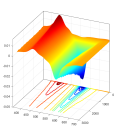

detailed method is necessary. That is where transient absorption spectroscopy comes into play, an extremely powerful and information-rich technique developed to investigate reaction mechanisms and excited state processes. The excellent combination of extremely high time resolution in the femto- and picosecond range, high energy pulses, high information density, and low measurement time of only a few minutes makes it the go-to solution for investigating any organic and inorganic chromophores. Synergizing absorption, emission, and vibrational spectroscopic methods, a full photophysical picture of any optically active substance can be obtained. This combination of techniques becomes even more powerful when combined with automated data evaluation techniques, such as PARAFAC, and with theoretical chemistry calculations, such as TD-DFT. By this combination, the large amount of data generated can be handled, and can be interpreted extensively from a quantum mechanical perspective.

For a photophysical investigation, samples measured by TAS can be differentiated into inorganic and organic chromophores. While the organic chromophores are usually dominated by molecular orbital transitions in large organic ring systems, inorganic molecules are usually dominated by atomic transitions or charge transfer processes between a metal and its ligands.

As the detection limit of chromophores in transient absorption spectroscopy is dominated by their extinction coefficient in the ground and excited states, then molecules with extinction coefficients in the range of several thousand L mol^{-1} cm^{-1} are needed to detect substances in the mM or μM concentration range. That is why organic dyes are often easier to investigate than inorganic molecules and ions, because by having stronger absorption in the ground state, more molecules can be excited, thus giving a higher concentration of molecules in the excited state. Furthermore, the excited states of organic compounds often exhibit also a higher extinction coefficient, inducing a higher signal-to-noise ratio. However, the biggest drawback for organic dyes in high-intensity laser applications is photodegradation, whereby UV excitation and a high photon flux the dyes are getting destroyed, either by oxidation through dissolved oxygen, by reactions with the solvent, or inter- and intramolecular chemical reactions. Within minutes, these dyes can be completely destroyed. The degradation kinetics might influence the TAS measurement, as TAS is not actually measuring on femtosecond timescales

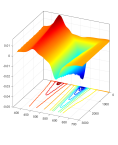

but uses sequential spectrum collection that needs minutes to conclude. Thus, the ultrafast kinetics might be convolved with the macroscopic degradation kinetics in the data. One way to compensate this, is by using a random instead of a sequential scanning mode, where the delay positions are not measured consecutively but randomly. However, this leads to two major problems: 1) The spectra are much noisier, as each delay position contains data of early and late degradation stages, and 2) the measurement takes much longer, as the delay stage is constantly driving back and forth between the delay positions, which takes more time and thus further worsens the problem. A more elegant solution developed in this thesis is to shorten the integration time for each spectrum so that each full scan takes up a much shorter time (much lower than the effects of degradation take place) while collecting more scans. Then, instead of averaging all spectra (which would be a valid approach, as degradation effects are minimized in all spectra), the whole set of scans is used in a PARAFAC deconvolution as a tensor, to deconvolve the different species spectra and ultrafast time profiles, alongside the global degradation kinetics over several minutes. By this approach it was possible not only to measure photoliable dyes without a sample regenerative flow cell, but also to shorten the measurement time and increase the information density by the additional degradation dimension. Furthermore, by the installation of two reference channels, one for the probe- and one for the pump-beam, the sensitivity and signal-to-noise ratio of the system could be increased by a factor of five. This made it possible to reduce the pump-beam intensity, i.e., photon flux, and thus further slow down the photodegradation process, without sacrificing spectra quality.

Using this approach, it is possible to better investigate fluorescent dyes, such as DBD dyes, S^4-DBD dyes, and pyridinylanthracenes, as smaller amounts of dye are necessary for each TAS measurement despite photodegradation. As their photophysical properties, especially in the presence of quenching, cannot always be identified by linear absorption and steady-state or time-resolved emission techniques, such TAS measurements are an absolute necessity for further molecule design improvements to increase absorption and luminescence efficiency. The luminescent properties of these dyes highly depend on the solvent, protonation stage, and substitution pattern. Using only the standard linear

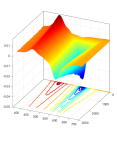

absorption and emission techniques, it can be complicated to understand the effects of those parameters, as no larger mechanistic understanding of excited state behavior can be deduced. With TAS however, several common effects, such as solvent relaxation and multipole changes, triplet formation, specific solvent interactions, and more, could be investigated in this thesis. Only when considering and understanding those microscopic and close-range effects on the chromophores, the macroscopic and ensemble effects (such as quenching, Stokes shifts, hypsochromic and bathochromic shifts of bands, etc.) can be understood, explained, and predicted. The dynamics and origin of these effects are most often only visible on the picosecond scale of TAS, as they involve molecular motion on the nanometer scale and are not accessible by many spectroscopic methods. For example, all the three investigated dye types exhibit a form of solvent relaxation that induces redshifts in emission bands and molecular geometry optimizations, whose time profiles could only be investigated in TAS. Furthermore, only with TAS, it is possible to separate the total stokes shift into the spectral shift induced by the initial geometry change from the spectral shift induced by solvent relaxation. From this separation, it is possible to calculate precise multipole moment changes of the molecules upon excitation.

Another important factor that can be easily detected by TAS measurements is the formation and observation of triplet states. When a triplet is formed, this is easily identifiable in the TA spectra as a new absorption of an emerging species, which coincides with the depopulation of, usually, the S_1 state. This formation can be used to calculate the quantum yields of triplet formations and other non-radiative deactivation rates. As these triplet states have good extinction coefficients for their triplet-triplet absorption, they have similar limits of detection as the absorptions of the singlet states (*vide supra*). This is a significant advantage compared to emission-based methods where these triplet states are usually difficult to detect, as organic molecules in triplet states usually have too many competing and faster vibrational deactivation pathways to emit any photons at room temperature or in the presence of dissolved oxygen. For TAS, these downsides of vastly reduced photon emission are not relevant, and triplets can be detected independent of those measuring conditions. This detection makes it easy to identify ISC as a reason for low luminescence quantum yields in organic dyes and opens up

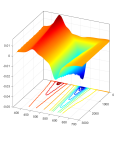

the possibility of counteracting those losses through synthetic approaches. For the three investigated organic dyes, this easy detection of triplet states by TAS induced further insides into their photophysical properties, which were previously unknown from luminescence spectroscopy. This was especially important for the S^4-DBD dyes, as their triplet formation yield is so high that a completely new application field as a triplet sensitizer or singlet oxygen generator might open up.

Synergizing TAS and PARAFAC deconvolution and consecutive modeling of the resulting kinetics via least-square fitting, were crucial in analyzing the samples. Only by these numeric techniques, it was possible to thoroughly explore the vast amount of generated data efficiently and extensively. We believe that the developed application of PARAFAC on TAS data is unprecedented, as usually not as sophisticated approaches for data deconvolution, such as SVD and PCA, are utilized in literature for TAS data evaluation. Furthermore, code modifications of PARAFAC, self-written data modeling algorithms with ODE solvers, and self-written temporal baseline algorithms increased the accuracy of the results and accelerated the data evaluation process immensely. Adding to the investigation of ultrafast kinetics, we can, with a detailed and thorough kinetic model, use TAS to determine complex stability constants from the fitted rate constants. This makes it possible to obtain thermodynamic data from ultrafast processes for both the ground and excited states.

As these complex stability constants are especially important in metal-ligand complexes, the utilization of TAS for uranyl(VI) complex investigation was obvious and promising. While many uranyl(VI) complexes are luminescent and can be investigated using luminescence spectroscopy in trace amounts, there are many important ligand systems in which uranyl(VI) luminescence is quenched and cannot be investigated by this method. As TAS is actively probing the sample, it does not rely on the sample being fluorescent, hence, it is not "blind" for non-luminescent or quenched samples. It opens up a whole new field for spectroscopic investigations of those samples, instead of relying only on linear absorption and vibrational spectroscopic methods. As none of the two methods are time-resolved or investigate the excited states, it is harder to differentiate complex species if they are spectrally similar, while in TAS, this is less of a concern, as two species usually have distinctive kinetic properties that can

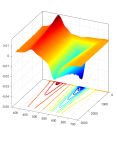

be extracted from the temporal data dimension. Furthermore, certain uranyl(VI)-related species, luminescent or not, are only visible as transient species that are not persistent in the sample. These short-lived photoproducts, like halogenide diradicals $X_2^{\cdot -}$, have their own kinetics and reactions with other excited state complexes of uranyl(VI) that cannot be detected by steady state methods like UV/Vis or IR-/Raman spectroscopy or even time-resolved luminescence spectroscopy. The discovery and analysis of these transient species in TAS induced important insights into the luminescence quenching and reaction mechanisms, which not many spectroscopic techniques can investigate.

One other major advantage of TAS is the identification of excited electronic and vibronic states. Determining whether a state is a singlet or a triplet state can be done based on the time evolution or on spectral properties like transition probabilities (decay rate constants or extinction coefficients). Additionally, different states of the same multiplicity can be differentiated in TAS, like for the uranyl(VI) ion, where it was difficult to experimentally prove if the $^3\Delta$ or $^3\Phi$ state was the energetically lowest state that generates luminescence. This determination is achieved by combining TAS with quantum mechanical approaches like TD-DFT to calculate and interpret excitation spectra and predict changes in the charge distribution based on electron orbital transitions, alongside geometry changes like bond elongation and molecule planarization. Using quantum mechanical approaches, the energies of non-emitting triplet states can be estimated, as these states are often not accessible by linear absorption and emission techniques due to their low extinction coefficients and luminescence quantum yields. For small organic molecules, like organic dyes, these quantum mechanical calculations are nowadays easy and fast to execute, making them a standard chromophore investigation method to go along with TAS measurements. With this fundamental photophysical and quantum mechanical understanding, TAS measurements of chromophores can be fully understood, and they can also be used to compare the theoretical predictions of the calculations with experimental results.

With all the data gathered from linear absorption, luminescence, and TAS measurements, which are analyzed by PARAFAC deconvolution and kinetic modeling, and which are supported by quantum mechanical calculations, it is possible to generate a detailed Jabłoński diagram of a photophysical

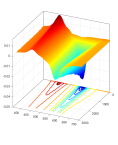

system. These diagrams contain all the experimentally observed and identified photophysical processes, such as electronic transitions and photoreactions. Without TAS, these diagrams are usually very sparse, as they only show the lowest excited states of molecules from luminescence spectroscopy, alongside the energetic positions of higher excited states from linear absorption spectroscopy. Furthermore, they often do not show any time constants connecting those excited states and are often lack information about triplet energies and processes, without displaying any ultrafast processes, such as solvent relaxation. This sparsity problem is even larger when no emission is observed from the chromophore, as even less information can be gained from classical optical spectroscopic methods — linear absorption and luminescence spectroscopy. With TAS, it is possible to generate detailed diagrams that are invaluable for any work related to those chromophores and are the fundamental photophysical basis for any optical spectroscopic application or analysis of those molecules. This makes TAS itself a fundamental tool in any chromophore analysis, which cannot be left out when characterizing and quantifying photophysical properties for applications in microscopy or environmental analysis.

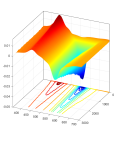

5

Summary & Outlook

Transient absorption spectroscopy is an invaluable technique when investigating the spectroscopic and photophysical properties of organic and inorganic chromophores. The extremely high time resolution in the femto- and picosecond ranges makes it possible to investigate inter- and intramolecular electronic and vibrational processes, which is mostly unparalleled in spectroscopy. Although the sensitivity is limited, the spectral and temporal information density is enormous, as any state or photoproduct with sufficient absorption can be detected and considered in a mechanistic model or descrip-

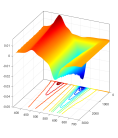

tion of a sample. Compared to luminescence spectroscopy, the application of this method extends to non-luminescent samples due to the active probing mechanism of the spectrometer. This further extends to highly quenched chromophores and strong triplet-forming molecules.

In this work, transient absorption spectroscopy was used as an investigation technique for the analysis of three organic dye types (DBDs, S^4-DBDs, and pyridylanthracenes) and the inorganic optically active molecule uranyl(VI). For all the investigated samples the excited states and their excited state reactions were analyzed and quantified. For the organic dyes,strong changes in multipole moments and the resulting solvent relaxation were observed. However, while the solvent relaxation was strong for the DBD dyes due to their high quadrupole moment change, the geometry change was the stronger effect for the large Stokes shifts of these dyes. Furthermore, for the DBD dyes and the anthracene derivates it was found that the formation of a triplet state was the major competitive mechanism to the luminescence and thus lowered the dyes' luminescence quantum yields. Also, the S^4-DBD dyes' triplet formation was even stronger than for the O^4-DBD dyes, while for the anthracene derivates, the increase in other non-radiative processes was the cause for the drop in the luminescence quantum yield of the protonated forms. It was further found that the strong Stokes shift, one of the biggest strengths of DBD dyes, is also the source of the reduced luminescence quantum yields in more polar solvents. As the solvent relaxation is strongest in these solvents, the smaller energy gap leads to more non-radiative deactivation according to the energy gap law. These additional pathways necessitated to shorter luminescence lifetimes and lower luminescence quantum yields. With the here identified causes of the low luminescence quantum yields of these organic dyes, it is now possible to reduce these luminescence quantum yield losses via synthesis approaches or to even increase the triplet formation rate to repurpose some of these dyes into triplet sensitizers.

For the non-complexed uranyl(VI) on the other hand, it was possible to identify two transient species by TAS. It was previously shown that using the quantum mechanical calculations from the literature, it was possible to assign those states to the energetically lowest excited states $^3\Delta$ and $^3\Phi$, where the $^3\Delta$ state is the energetically lowest of the two and thus the source of the uranyl(VI) lumi-

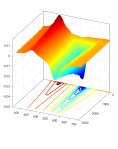

nescence in water under acidic conditions. However, the here shown and more impressive result is that uranyl(VI) could be measured in solutions with high concentrations of chloride and bromide ions at room temperature. Under these conditions, luminescence spectroscopy is simply "blind", as the luminescence of uranyl(VI) is strongly quenched by those ions, and no emission can be detected. So far, the quenching mechanism of uranyl(VI) by halides has not been fully understood, but it could be conclusively shown here which mechanistic steps induced the decrease in uranyl(VI) luminescence. It was found that the actual cause was an excited state redox reaction between the excited uranyl(VI) and the halide ions. Surprisingly, excited uranyl(VI) is an extraordinary strong oxidizer that is capable to even oxidize halide ions to form dihalide radical ions $X_2^{\cdot -}$. These radicals could be identified in TAS as a new transient species at the blue end of the spectrum and occur only in halide-rich samples. Hence, we can conclude that, while the formation of the 1:1-uranyl(VI)-halide complex $[UO_2X]^+$ is the source of the static quenching component in luminescence spectroscopy, the consecutive collision with a second halide ion is the source of the dynamic quenching component. This dynamic mechanism forms the 1:2-uranyl(VI)-halide complex $[UO_2X_2]^0$, which then undergoes a fast redox reaction and separation into "free" radical ions. It could be shown that this mechanism holds for chloride and bromide ions over a large concentration range. This mechanism further explains the luminescence of these complexes under cryogenic conditions, where the diffusion-based processes of halide collision and radical separation are suppressed, and the luminescence is the remaining deactivation pathway. Further investigation in the non-aqueous solvents ACN and acetone showed that the separation process is also suppressed in low dielectric media, which also induces luminescence. Adding to the quenching mechanism, ground and excited state complex stability constants could be determined for each chloride and bromide complex, resulting in a complete photophysical picture of uranyl(VI) interaction with halides. Based on these results, it is now understood why luminescence is quenched for these highly relevant uranyl(VI) sample matrices of long-term repository and environmental research. This lays the foundation for improving spectroscopic investigations in this topic, such as conducting luminescence measurements only under cryogenic conditions to suppress quenching and measuring

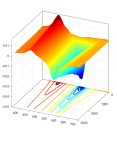

only frozen ground state instead of excited state equilibrium constants.

In this work, TAS was successfully shown to be an extremely valuable addition to any spectroscopic and photophysical investigation of chromophores due to its high time resolution, applicability to non-luminescent systems, and high information density. It is an essential method for reaction and luminescence quenching mechanism investigation, excited state dynamics and kinetics evaluation, and the determination of complexes and complex stability constants.

Future aspects of TAS investigation can be the application to new inorganic systems, such as expanding research into the realm of uranium(IV), its complexes, and luminescence quenching mechanisms. Due to the, in the long run, reducing conditions in long-term nuclear repositories, this oxidation state will dominate. Thus, it is of vast environmental interest to understand the fundamental photophysical processes of this oxidation state for the application of luminescence spectroscopy in that research field. Furthermore, newly designed dyes based on the presented results require as well a photophysical characterization to determine their efficiencies and processes and to further improve their designs for future microscopy applications.

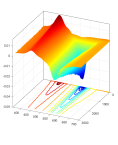

Bibliography

[1] Heinz Langhals. “Fluorescence and fluorescent dyes”. In: *Phys. Sci. Rev.* 5.8 (2020).

[2] Nigar Anzar et al. “Carbon nanotube - A review on Synthesis, Properties and plethora of applications in the field of biomedical science”. In: *Sensors Int.* 1 (2020), p. 100003.

[3] T. H. Maiman. “Stimulated Optical Radiation in Ruby”. In: *Nature* 187.4736 (1960), pp. 493–494.

[4] C. Moulin et al. “Determination of uranium in solution at the ng l-1 level by time-resolved laser-induced spectrofluorimetry: application to geological samples”. In: *Anal. Chim. Acta* 238 (1990), pp. 291–296.

[5] Ninad Mehendale and Srushti Neoge. “Review on Lidar Technology”. In: *SSRN Electron. J.* (2020).

[6] Russell S. Harmon, Richard E. Russo, and Richard R. Hark. “Applications of laser-induced breakdown spectroscopy for geochemical and environmental analysis: A comprehensive review”. In: *Spectrochim. Acta - Part B At. Spectrosc.* 87 (2013), pp. 11–26.

[7] Peter Moulton. “Spectroscopic and laser characteristics of Ti:Al2O3”. In: *J. Opt. Soc. Am. B* 3.1 (1986), pp. 125–133.

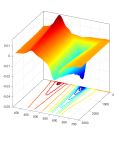

[8] R. W. Sabnis. *Handbook of Biological Dyes and Stains: Synthesisand Industrial Applications*. 2010.

[9] Hoa T. Hoang, Toni Haubitz, and Michael U. Kumke. "Photophysics of "Floppy" Dyads as Potential Biomembrane Probes". In: *J. Fluoresc.* 28.5 (2018), pp. 1225–1237.

[10] Hans Blom and Jerker Widengren. *Stimulated Emission Depletion Microscopy*. 2017.

[11] Robert Wawrzinek et al. "DBD dyes as fluorescence lifetime probes to study conformational changes in proteins". In: *Chem. - A Eur. J.* 19.51 (2013), pp. 17349–17357.

[12] Pablo Wessig, Leonard John, and Monique Mertens. "Extending the Class of [1,3]-Dioxolo[4.5- f]benzodioxole (DBD) Fluorescent Dyes". In: *European J. Org. Chem.* 2018.14 (2018), pp. 1674–1681.

[13] Pablo Wessig et al. "FRET Pairs with Fixed Relative Orientation of Chromophores". In: *European J. Org. Chem.* 2016.26 (2016), pp. 4476–4486.

[14] Robert Wawrzinek et al. "DBD dyes as fluorescent probes for sensing lipophilic environments". In: *Bioorganic Med. Chem. Lett.* 22.17 (2012), pp. 5367–5371.

[15] Pablo Wessig et al. "Fluorescent dyes with large Stokes shifts based on benzo[1,2-d:4,5-d']bis([1,3]dithiole) ("S4-DBD dyes")". In: *European J. Org. Chem.* (2020).

[16] Werner Fudickar and Torsten Linker. "Synthesis of Pyridylanthracenes and Their Reversible Reaction with Singlet Oxygen to Endoperoxides". In: *J. Org. Chem.* 82.17 (2017), pp. 9285–9262.

[17] Sam Keith Keith et al. "Toxicological Profile for Uranium". In: *Toxicol. Profiles* (2013), pp. 1–526.

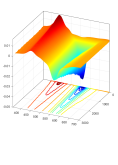

[18] Stephanie Handley-Sidhu et al. “A review of the environmental corrosion, fate and bioavailability of munitions grade depleted uranium”. In: *Sci. Total Environ.* 408.23 (2010), pp. 5690–5700.

[19] “WHO | Uranium in drinking-water”. In: *WHO* (2012).

[20] Euo Chang Jung et al. “Uranium determination in groundwater using laser spectroscopy”. In: *Rev. Anal. Chem.* 33.4 (2014), pp. 245–254.

[21] Björn Drobot et al. “Speciation Studies of Metals in Trace Concentrations: The Mononuclear Uranyl(VI) Hydroxo Complexes.” eng. In: *Anal. Chem.* 88 (2016), pp. 3548–3555.

[22] Hugh D. Burrows et al. “Quenching of the luminescent state of the uranyl ion (UO) by metal ions. Evidence for an electron transfer mechanism”. In: *J. Chem. Soc. Faraday Trans. 1 Phys. Chem. Condens. Phases* 72.0 (1976), pp. 163–171.

[23] C. Götz, G. Geipel, and G. Bernhard. “The influence of the temperature on the carbonate complexation of uranium(VI): A spectroscopic study”. In: *J. Radioanal. Nucl. Chem.* 287 (2011), pp. 961–969.

[24] Hugh D. Burrows. “Electron transfer from halide ions to uranyl(2+) excited-state ions in aqueous solution: formation and decay of dihalide radical anions”. In: *Inorg. Chem.* 29 (1990), pp. 1549–1554.

[25] Rudi Berera, Rienk van Grondelle, and John T M Kennis. “Ultrafast transient absorption spectroscopy: Principles and application to photosynthetic systems”. In: *Photosynth. Res.* 101.2-3 (2009), pp. 105–118.

[26] A. Einstein. “Über einen die Erzeugung und Verwandlung des Lichtes betreffenden heuristischen Gesichtspunkt”. In: *Ann. Phys.* 322.6 (1905), pp. 132–148.

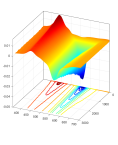

[27] M. Planck. “Ueber das Gesetz der Energieverteilung im Normalspectrum”. In: *Ann. Phys.* 309.3 (1901), pp. 553–563.

[28] J. J. Thomson. “XL. Cathode Rays”. In: *London, Edinburgh, Dublin Philos. Mag. J. Sci.* 44.269 (1897), pp. 293–316.

[29] E. Rutherford. “LXXIX. The scattering of α and β particles by matter and the structure of the atom”. In: *London, Edinburgh, Dublin Philos. Mag. J. Sci.* 21.125 (1911), pp. 669–688.

[30] M. Orchin et al. *Atomic Orbital Theory*. 2005.

[31] E. Schrödinger. “Quantisierung als Eigenwertproblem”. In: *Ann. Phys.* 384.4 (1926), pp. 361–376.

[32] Joseph R. Lakowicz. *Principles of fluorescence spectroscopy*. 3rd. New York: Springer, 2006, p. 954.

[33] H N Russell and F A Saunders. “New Regularities in the Spectra of the Alkaline Earths”. In: *Astrophys. J.* 61 (1925), p. 38.

[34] W. Heisenberg. “Mehrkörperproblem und Resonanz in der Quantenmechanik”. In: *Zeitschrift für Phys.* 38.6 (1926), pp. 411–426.

[35] J. Franck and E. G. Dymond. “Elementary processes of photochemical reactions”. In: *Trans. Faraday Soc.* 21 (1926), pp. 536–542.

[36] Edward Condon. “A Theory of Intensity Distribution in Band Systems”. In: *Phys. Rev.* 28.6 (1926), pp. 1182–1201.

[37] M. Born and R. Oppenheimer. “Zur Quantentheorie der Molekeln”. In: *Ann. Phys.* 389.20 (1927), pp. 457–484.

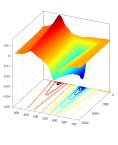

[38] J Orear et al. *Nuclear Physics: A Course Given by Enrico Fermi at the University of Chicago*. Midway reprints. University of Chicago Press, 1950.

[39] Robert Englman and Joshua Jortner. "The energy gap law for non-radiative decay in large molecules". In: *J. Lumin.* 1-2 (1970), pp. 134–142.

[40] Michael Kasha. "Characterization of Electronic Transitions in Complex Molecules". In: *Trans. Faraday Soc.* 9.c (1950), pp. 14–19.

[41] Albert Einstein. "Zur Quantentheorie der Strahlung". In: *Mittl. Phys. Gesell. Zurich* 18 (1916), pp. 47–62.

[42] E. Lippert. "Spektroskopische Bestimmung des Dipolmomentes aromatischer Verbindungen im ersten angeregten Singulettzustand". In: *Zeitschrift für Elektrochemie, Berichte der Bunsengesellschaft für Phys. Chemie* (1957).

[43] Noboru Mataga, Yozo Kaifu, and Masao Koizumi. "Solvent Effects upon Fluorescence Spectra and the Dipolemoments of Excited Molecules". In: *Bull. Chem. Soc. Jpn.* (1956).

[44] T. Förster. "Zwischenmolekulare Energiewanderung und Fluoreszenz". In: *Ann. Phys.* 437.1-2 (1948), pp. 55–75.

[45] D L Dexter. "A Theory of Sensitized Luminescence in Solids". In: *J. Chem. Phys.* 21.5 (1953), pp. 836–850.

[46] Rasmus Bro. "PARAFAC. Tutorial and applications". In: *Chemom. Intell. Lab. Syst.* 38 (1997), pp. 149–171.

[47] *MATLAB and Optimization Toolbox 2018b*. Natick, Massachusetts, 2019.

[48] Frank Neese. "Software update: the ORCA program system, version 4.0". In: *Wiley Interdiscip. Rev. Comput. Mol. Sci.* (2018).

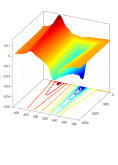

[49] Frank Neese. "The ORCA program system". In: *Wiley Interdiscip. Rev. Comput. Mol. Sci.* (2012).

[50] Abdulazeez T. Lawal. "Polycyclic aromatic hydrocarbons. A review". In: *Cogent Environ. Sci.* 3.1 (2017), p. 1339841.

[51] John B. Birks. *Photophysics of aromatic molecules*. London: Wiley-Interscience, 1970, p. 704.

[52] Victor Gray et al. "Photophysical characterization of the 9,10-disubstituted anthracene chromophore and its applications in triplet-triplet annihilation photon upconversion". In: *J. Mater. Chem. C* 3.42 (2015), pp. 11111–11121.

[53] F J Duarte and L W Hillman. *Dye laser principles*. English. 1st ed. United States: San Diego, CA (United States); Academic Press Inc., 1990.

[54] Toni Haubitz et al. "PH-Sensitive Fluorescence Switching of Pyridylanthracenes: The Effect of the Isomeric Pattern". In: *J. Phys. Chem. A* 124.52 (2020), pp. 11017–11024.

[55] Emel Onal et al. "Lifetime-Based Oxygen Sensing Properties of palladium(II) and platinum(II) meso-tetrakis(4-phenylethynyl)phenylporphyrin". In: *J. Fluoresc.* 27 (2017), pp. 861–868.

[56] N. Wiberg, A. F. Holleman, and E. Wiberg. *Holleman-Wiberg's Inorganic Chemistry*. De Gruyter, 2002, p. 1924.

[57] M. Alex Brown et al. "A novel method for molybdenum-99/technetium-99m recovery via anodic carbonate dissolution of irradiated low-enriched uranium metal foil". In: *Ind. Eng. Chem. Res.* 54.2 (2015), pp. 712–719.

[58] Yuheng Wang et al. "Mobile uranium(IV)-bearing colloids in a mining-impacted wetland." eng. In: *Nat. Commun.* 4 (2013), p. 2942.

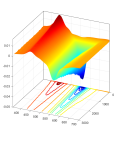

[59] John R. Bargar et al. “Biogenic uraninite nanoparticles and their importance for uranium remediation”. In: *Elements* 4.6 (2008), pp. 407–412.

[60] David Bodansky. *Nuclear energy: Principles, practices, and prospects: Second edition*. Springer New York, 2005, pp. 1–693.

[61] C. Hennig et al. “Comparative EXAFS investigation of uranium(VI) and -(IV) aquo chloro complexes in solution using a newly developed spectroelectrochemical cell”. In: *Inorg. Chem.* 44.19 (2005), pp. 6655–6661.

[62] Björn Drobot et al. “Combining luminescence spectroscopy, parallel factor analysis and quantum chemistry to reveal metal speciation – a case study of uranyl(VI) hydrolysis”. In: *Chem. Sci.* 6 (2015), pp. 964–972.

[63] A. A. Migdisov et al. “A spectroscopic study of uranyl speciation in chloride-bearing solutions at temperatures up to 250 °C”. In: *Geochim. Cosmochim. Acta* 222 (2018), pp. 130–145.

[64] Robert G. Denning. “Electronic structure and bonding in actinyl ions and their analogs”. In: *J. Phys. Chem. A* 111.20 (2007), pp. 4125–4143.

[65] Florent Real et al. “Theoretical investigation of the energies and geometries of photoexcited uranyl(VI) ion: a comparison between wave-function theory and density functional theory.” In: *J. Chem. Phys.* 127 (2007), p. 214302.

[66] Toni Haubitz et al. “Ultrafast Transient Absorption Spectroscopy of UO22+ and [UO2Cl]+”. In: *J. Phys. Chem. A* (2018).

[67] David Brewster. “XIII.—On the Decomposition and Dispersion of Light within Solid and Fluid Bodies”. In: *Trans. R. Soc. Edinburgh* 16.2 (1846), pp. 111–121.

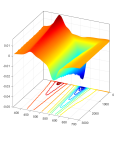

[68] Jerome Kretzschmar et al. “Network-like arrangement of mixed-valence uranium oxide nanoparticles after glutathione-induced reduction of uranium(vi)”. In: *Chem. Commun.* 54.63 (2018), pp. 8697–8700.

[69] L. Soderholm, S. Skanthakumar, and Richard E. Wilson. “Structural Correspondence between Uranyl Chloride Complexes in Solution and Their Stability Constants”. In: *J. Phys. Chem. A* 115 (2011), pp. 4959–4967.

[70] Susanne Lehmann et al. “Thermodynamic and structural aspects of the aqueous uranium(iv) system - hydrolysis vs. sulfate complexation”. In: *Dalton Trans.* 48.48 (2019), pp. 17898–17907.

[71] Akira Kirishima et al. “Luminescence properties of tetravalent uranium in aqueous solution”. In: *Radiochim. Acta* 92.9-11 (2004), pp. 705–710.

[72] A. Ekstrom. “Kinetics and Mechanism of the Disproportionation of Uranium(V)”. In: *Inorg. Chem.* 13.9 (1974), pp. 2237–2241.

[73] Toshinari Ogura et al. “Spectroelectrochemical identification of a pentavalent uranyl tetrachloro complex in room-temperature ionic liquid”. In: *Inorg. Chem.* 50.21 (2011), pp. 10525–10527.

[74] Koichiro Mizuoka et al. “Electronic spectra of pure uranyl(V) complexes: Characteristic absorption bands due to a UVO2+ core in visible and near-infrared regions”. In: *Inorg. Chem.* 44.18 (2005), pp. 6211–6218.

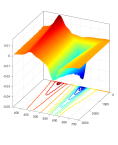

A

Supporting Informations

A.1 SI of Photophysics of Acyl- and Ester-DBD Dyes: Quadrupole Induced Solvent Relaxation Investigated by Transient Absorption Spectroscopy

A.1.1 Theoretical Calculations

Calculated geometries and bond distances from TD-DFT in M062X/def2-TZVP of the ground and excited state of the cis- and trans-conformer of the Acyl-DBD dye are given in Figure A.1.1. Their relative ground state energy difference was calculated to be 0.25 kcal mol^{-1}, which translates to 41%

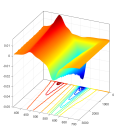

of the cis-conformer being present at room temperature. Upon excitation a significant bond length decrease of the carbonyl-carbon and aromatic-carbon bond has been observed, due to the increase in double bond character. The DBD core becomes elon-gated along the substituent axis and compressed along the dioxol-ring axis. The dipole moments of the trans- and cis-conformer were calculated to 0.00 and 3.11 D, respectively.

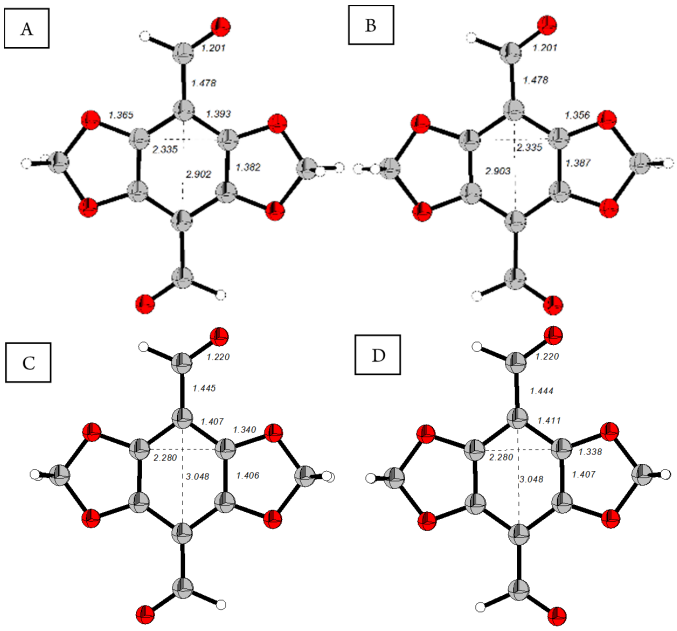

Figure A.1.1: Calculated Acyl-DBD geometries from TD-DFT calculations in M062X/def2-TZVP of the ground (top) and excited state (bottom) of the trans- (left) and cis-conformer (right).

A.1.2 Carboxylate-DBD Synthesis

a. General Information The ^{1}H NMR and ^{13}C NMR spectra were recorded at a Bruker Avance 300 (300 MHz, 75 MHz) in deuterated solvents as internal standard (^{1}H NMR: [D_6]DMSO = 2.50 ppm; 13C NMR: [D_6]DMSO = 39.5 ppm). Chemical shifts are given in ppm. The coupling constants are given in Hz for the following multiplicities: s = singlet, d = doublet, t = triplet, q = quartet and m = multiplet. High resolution mass spectroscopy (HRMS) was performed on a GC-MS Trace DSQ II mass spectrometer. The melting point was recorded on an Elektrothermal 9100 melting point appa-

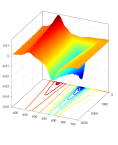

ratus and are uncorrected. Thin layer chromatography (TLC) was performed on TLC Silica gel 60 RP-18 F254 aluminium sheets from Merck.

b. Sample Preparation Benzo[1,2,4,5]bis([1,3]dioxole)-4,8-dicarboxylic acid

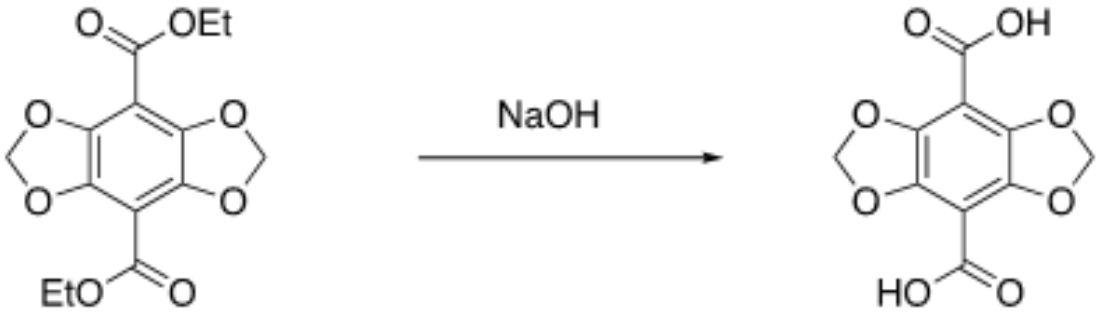

DBD-Diester (50 mg, 0.16 mmol, 1.0 eq.) was dissolved in a mixture of 4 mL acetonitrile and 4 mL water. After adding NaOH (250 mg, 6.45 mmol, 40 eq.) the solution was heated for 4 h at 60 °C. The mixture was extracted with DCM and acidified with 1M HCl to pH = 2. The precipitated red solid was filtered off, washed with MeOH, DCM and Et2O and dried in vacuum to obtain the carboxylate-DBD (34 mg, 0.13 mmol, 83%) as a red solid.

Tetrabutylammonium benzo[1,2,4,5]bis([1,3]dioxole)-4,8-dicarboxylate

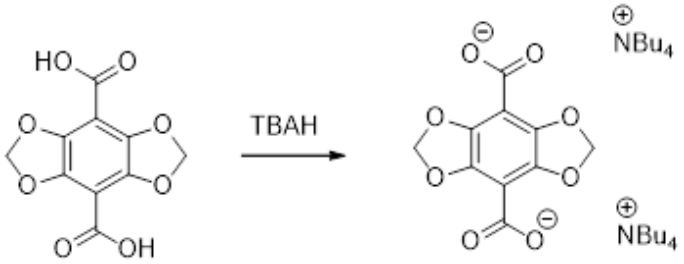

Carboxylate-DBD (10 mg, 0.04 mmol, 1.0 eq.) and tetrabutylammonium hydroxide (TBAH)-solution (0.1 M, 0.78 mL, 2.0 eq. 0.08 mmol) were dissolved in five drops of dry DMF and stirred for 1 h at room temperature. The solvent was removed in vacuo to obtain the product (29 mg, 0.04 mmol, quant.) as a slightly orange oil.

Compund Characterization

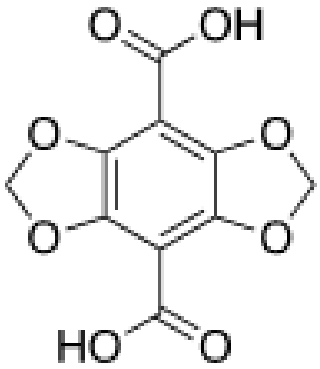

Rf = 0.50 (ACN:H2O 1:1); IR (ATR, cm^{-1}) 2810, 2671, 2540, 1682, 1441, 1262, 1185, 1063, 930; ^{1}H-NMR (DMSO-d_6, 300 MHz, ppm): δ = 6.08 (s, 4H, CH_2), 13.35 (2H, bs, COOH); ^{13}C-NMR (DMSO-d_6, 75 MHz, ppm): δ = 102.4 (CH_2), 103.3 ($C_{q/ar}$), 141.1 ($C_{q/ar}$), 162.4 ($C_{q/COOH}$); m.p.: > 230 °C; HRMS [EI]: m/z calc. for $C_{10}H_6O_8$: 254.0063, found: 254.0065.

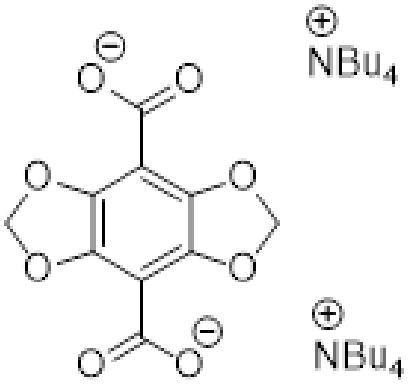

Rf = 0.10 (ACN:H2O 1:1); IR (ATR, cm^{-1}) 2921, 2890, 2520, 1590, 1403, 1234, 1157, 1020; ^{1}H-NMR (DMSO-d_6, 300 MHz, ppm): δ = 0.92 (t, J = 7.3 Hz, 24H, CH_3), 1.30 (q, J = 7.2 Hz, 16H,CH_2), 1.56 (q, J = 7.2 Hz, 16H,CH_2), 3.15 – 3.18 (m, 16H, CH_2), 5.66 (s, 4H, CH_2); ^{13}C-NMR (DMSO-d_6, 75 MHz, ppm): δ = 13.5 (CH_3), 19.2 (CH_2), 23.1 (CH_2), 57.5 (CH_2), 99.2 (CH_2), 111.2 ($C_{q/ar}$), 137.3 ($C_{q/ar}$), 163.5 ($C_{q/COO}$); HRMS [ESI]: m/z calc. for $C_{42}H_{76}N_2O_8$:759.5499 [M^+]; found: 759.5427.

d. NMR Spectra

Benzo[1,2,4,5]bis([1,3]dioxole)-4,8-dicarboxylic acid

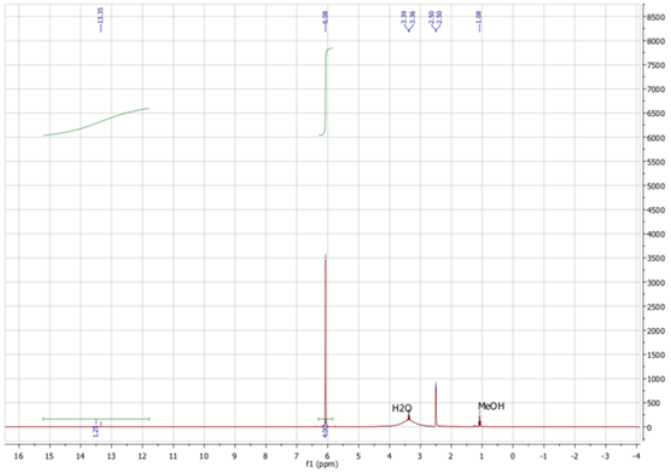
H2O
MeOH
f1 (ppm)

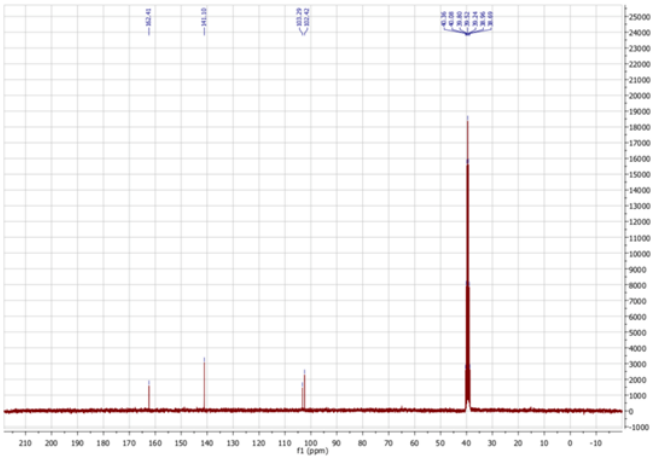
f1 (ppm)

Tetrabutylammonium benzo[1,2,4,5]bis([1,3]dioxole)-4,8-dicarboxylate

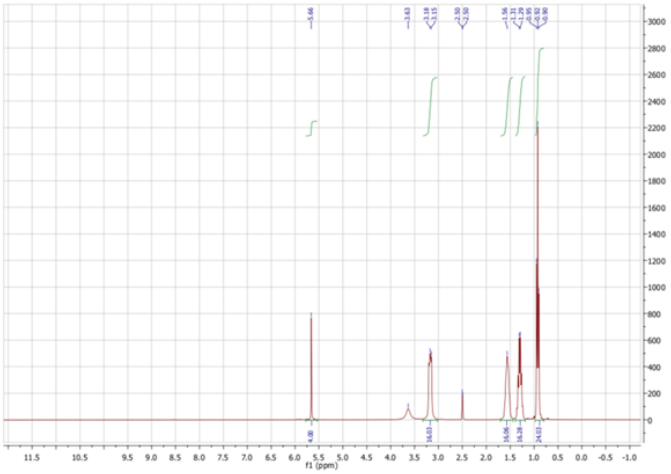

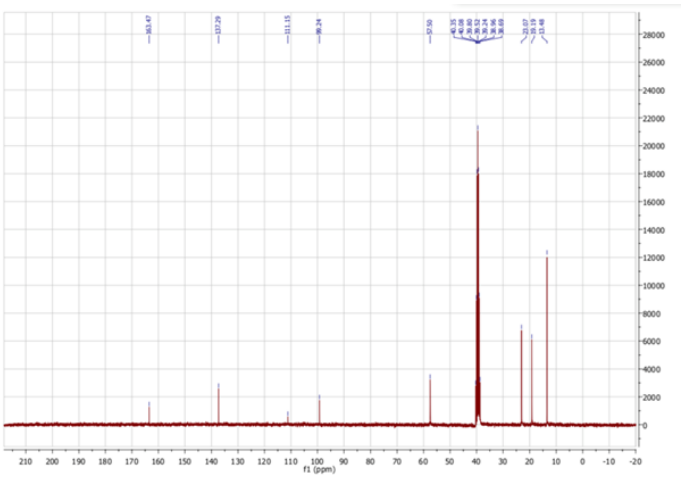

A.1.3 Viscosity dependence of the Ester-DBD dye

Viscosity dependence of the Ester-DBD dye is very similar to the Acyl-DBD dye and a linear relationship could be applied. No convergence of the quenched fluorescence lifetime and the extended solvent relaxation times is occurring at high glycerol concentrations, due to the generally longer fluorescence lifetime.

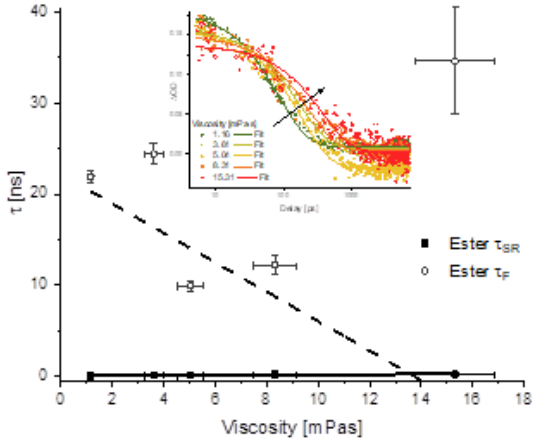

Figure A.1.2: Viscosity dependence of the solvent relaxation time τ_{SR} and fluorescence decay time τ_F of the Ester-DBD in Ethanol-Glycerol-mixtures. Inset: Monoexponential fit of data curves.

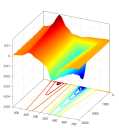

A.1.4 Nitrogen based Dye

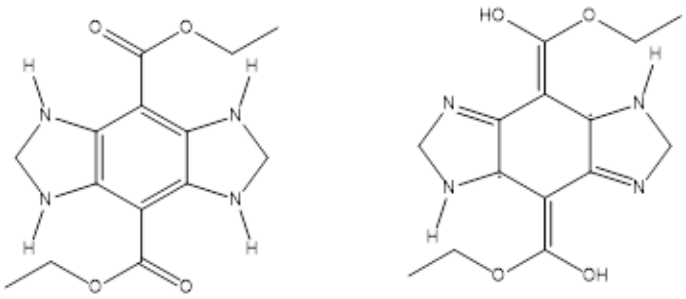

Figure A.1.3: Structure of proposed Nitrogen-DBDs. Left: Ground state electronic configuration. Right: Supposed principal electron configuration in the first excited state.

A.2 SI of Quenching Mechanism of Uranyl(VI) by Chloride and Bromide in Aqueous and Non-Aqueous Solution

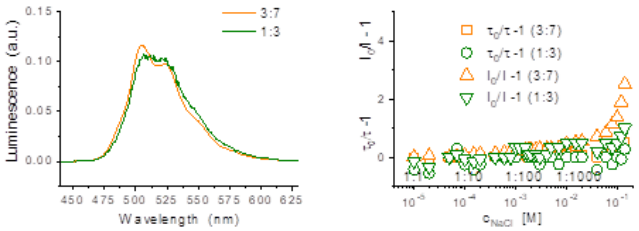

Figure A.2.1: Deconvoluted U(VI) luminescence spectra for 10^{-5} M U(VI) and 0.1 M $NaClO_4$ solution at pH 8.0 (left) and its Stern-Volmer plot with increasing NaCl concentration (right). 1:3 and 3:7 correspond to $UO_2(OH)^{3-}$ and $(UO_2)_3(OH)^{7-}$, respectively.

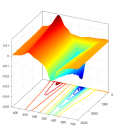

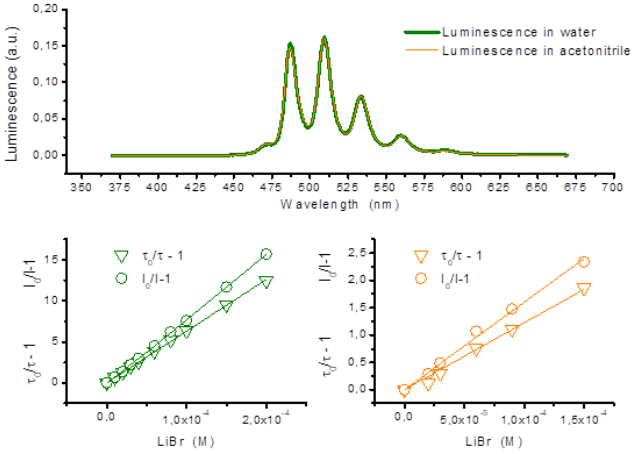

Figure A.2.2: Emission spectra of 10^{-4} M U(VI) with 10^{-2} $HClO_4$ in water (pH 2.0) and in acetonitrile (upper) and its Stern-Volmer plots (lower) with increasing bromide concentration ($0 \leq [LiBr] \leq 2.0 \cdot 10^{-4}$ M).

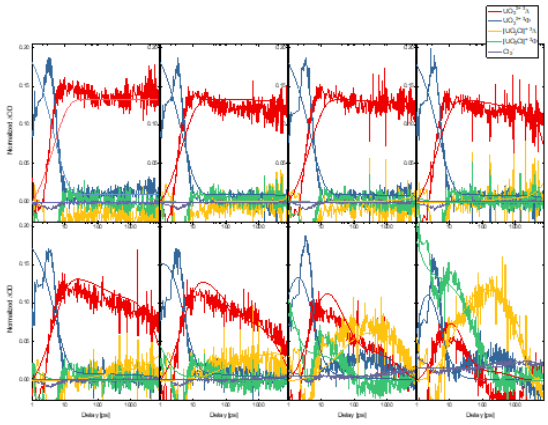

Figure A.2.3: PARAFAC deconvoluted time-traces of the found species in uranyl-chloride samples. Noisy lines represent data, smooth lines represent fit by the kinetic model. Chloride concentrations are logarithmically increasing from top left to bottom right in $10^{-0.5}$ M steps from 0 to 1 M concentration. I = 1 M, c_U = 0.01 M, pH = 0.

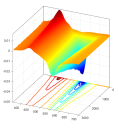

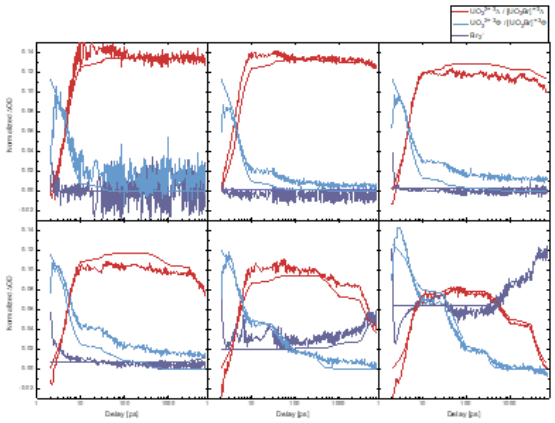

Figure A.2.4: PARAFAC deconvoluted time-traces of the found species in uranyl-bromide samples. Noisy lines represent data, smooth lines represent fit by the kinetic model. Bromide concentrations are logarithmically increasing from top left to bottom right in $10^{-0.5}$ M steps from 0 to 0.1 M concentration. I = 1 M, c_U = 0.01 M, pH = 0.

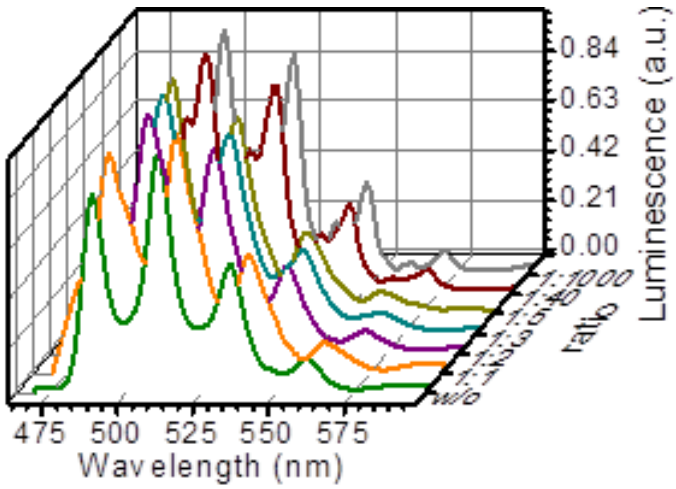

Figure A.2.5: Emission spectra of 10^{-4} M U(VI) in acetone with increasing chloride concentration (0 ≤ [LiCl] ≤ 0.1 M). Excitation wavelength is 340 nm.

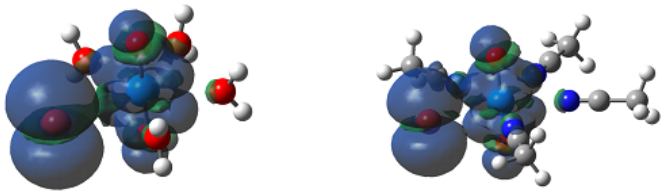

Figure A.2.6: The structures and spin density α – β of the lowest-lying triplet state (T_1) of $[UO_2Br(H_2O)_4]^+$ (left) and $[UO_2Br(CH_3CN)_4]^+$ (right). The isovalue of the surface is 0.0004 a.u..

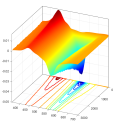

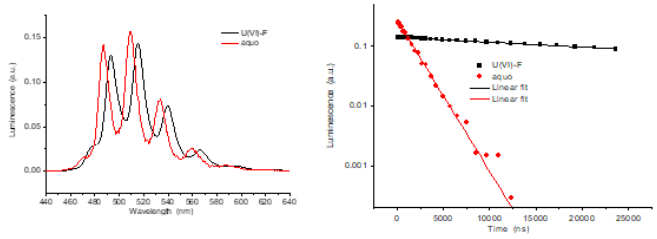

Figure A.2.7: Emission spectra (left) and luminescence decay over time (right) of 1.0×10^{-4} U(VI) and 1.0×10^{-4} NaF in water at pH 2.0 after PARAFAC deconvolution. The uranyl(VI)-fluoride complex represents 90 % of overall intensity.

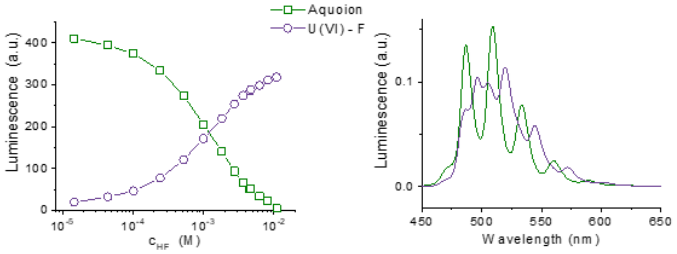

Figure A.2.8: Emission spectra (right) and luminescence intensity (left) of 1.0×10^{-4} U(VI) and 1.0×10^{-4} HF in ACN after PARAFAC deconvolution.

$$^{3}\Phi\ UO_2^{2+}: \frac{dy_1}{dt} = k_2 * y_2 + k_6 * y_3 - (k_1 + k_5 * y_9) * y_1 \tag{A.1}$$

$$^{3}\Delta\ UO_2^{2+}: \frac{dy_2}{dt} = k_1 * y_1 + k_4 * y_4 - (k_2 + k_3 * y_9) * y_2 \tag{A.2}$$

$$^{3}\Phi\ [UO_2X]^{+}: \frac{dy_3}{dt} = k_5 * y_9 * y_1 + k_8 * y_4 + k_{12} * y_5 - (k_6 + k_7 + k_{11} * y_9) * y_3 \tag{A.3}$$

$$^{3}\Delta\ [UO_2X]^{+}: \frac{dy_4}{dt} = k_3 * y_9 * y_2 + k_7 * y_3 + k_{10} * y_6 - (k_4 + k_8 + k_9 * y_9) * y_4 \tag{A.4}$$

$$^{3}\Phi\ [UO_2X_2]^{o}: \frac{dy_5}{dt} = k_{11} * y_9 * y_3 + k_{14} * y_6 - (k_{12} + k_{13}) * y_5 \tag{A.5}$$

$$^{3}\Delta\ [UO_2X_2]^{o}: \frac{dy_6}{dt} = k_9 * y_9 * y_4 + k_{13} * y_5 + k_{16} * y_7 - (k_{10} + k_{14} + k_{15}) * y_6 \tag{A.6}$$

$$[UO_2^{+} \cdots X_2^{-}]^{o}: \frac{dy_7}{dt} = k_{15} * y_6 - (k_{16} + k_{17}) * y_7 \tag{A.7}$$

$$X_2^{-}: \frac{dy_8}{dt} = k_{17} * y_7 * -k_{18} * y_8 \tag{A.8}$$

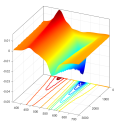

$$X^{-}: \frac{dy_9}{dt} = k_6 * y_3 + k_4 * y_4 + k_{12} * y_5 + k_{10} * y_6 - (k_5 * y_1 + k_3 * y_2 + k_9 * y_4 + k_{11} * y_3) * y_9 \quad \text{(A.9)}$$

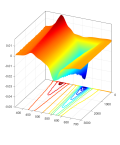

Table A.2.1: All fitted kinetic rates k. Ground state complex stability constants β from UV/Vis data. c_U = 0.01 M, c_{Cl} = 0 - 1 M, c_{Br} = 0 – 0.1 M, pH ≈ 0, I = 1 M

	Cl^-	Br^-	Unit
β_1	2.0	20	$[M^{-1}]$
k_1	210	400	$[ns^{-1}]$
k_2	11	< 0.01	$[ns^{-1}]$
k_3	45	60	$[ns^{-1}M^{-1}]$
k_4	6.0	< 0.01	$[ns^{-1}]$
k_5	< 0.01	< 0.01	$[ns^{-1}M^{-1}]$
k_6	870	< 0.01	$[ns^{-1}]$
k_7	1.0	12	$[ns^{-1}]$
k_8	0.03	< 0.01	$[ns^{-1}]$
k_9	12	22	$[ns^{-1}M^{-1}]$
k_{10}	< 0.01	410	$[ns^{-1}]$
k_{11}	680	60	$[ns^{-1}M^{-1}]$
k_{12}	< 0.01	0.012	$[ns^{-1}]$
k_{13}	14	410	$[ns^{-1}]$
k_{14}	< 0.01	< 0.01	$[ns^{-1}]$
k_{15}	110	580	$[ns^{-1}]$
k_{16}	15	5.4	$[ns^{-1}]$
k_{17}	2.2	2.9	$[ns^{-1}]$
k_{18}	0.07	0.08	$[ns^{-1}]$

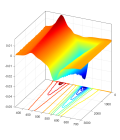

This thesis was typeset using LaTeX, originally developed by Leslie Lamport and based on Donald Knuth's TeX. The body text is set in 11 point Egenolff-Berner Garamond, a revival of Claude Garamont's humanist typeface. A template that can be used to format a PhD thesis with this look and feel has been released under the permissive MIT (XII) license, and can be found online at github.com/suchow/Dissertate or from its author, Jordan Suchow, at suchow@post.harvard.edu.